UNIVERSITÀ DEGLI STUDI DI PAVIA

Dipartimento di Scienze della Terra e dell'Ambiente

PhD Program in Earth and Environmental Sciences
Dottorato di Ricerca in Scienze della Terra e dell'Ambiente
XXXIII Series

Evolution of mantle melts intruding the lower continental crust: constraints from the Rocca d'Argimonia ultramafic sequence (Ivrea Mafic Complex, southern Alps)

PhD Thesis of
Marta Antonicelli

Tutor

Prof. Riccardo Tribuzio

Coordinator

Prof. Roberto Sacchi

Academic year 2019/2020

Acknowledgements

I would like to dedicate this thesis to my family and Ruben for their endless support all over my career.

I am very grateful to Prof. Riccardo Tribuzio (Università di Pavia) for his support and guidance over the three years of my doctorate, and to my colleagues from the Chinese Academy of Sciences of Beijing for their precious help with the analysis procedures. I would like to thank Antonio Langone (C.N.R., Unità di Pavia) for his support during U-Pb zircon analyses and sample preparation.

A sincere thanks also to my colleagues and friends Greta, Elisa, Roberta e Alberto for their help, support and relaxing Thursday dinners over these three years.

I also thank Maria Rosaria Renna and Silvano Sinigoi for their very precious revisions and constructive comments to my thesis.

Finally, I want to thank all scientist and people I met during my academic career and who allowed me to arrive at this point.

INDEX

Preface

The Ivrea-Verbano Zone from Italian Alps exposes a nearly complete, lower continental crustal section (e.g., Schmid et al., 2017). This section mostly consists of a ~8 km thick gabbroic-dioritic sequence of Lower Permian age (Ivrea Mafic Complex) that intruded a granulite to amphibolite facies basement (Kinzigite Formation) in conjunction with the post-collisional transtensional regime of the Variscan orogeny (e.g., Handy et al., 1999; Wilson et al., 2004). This gabbroic-dioritic complex is an excellent natural laboratory to assess the lower crust processes associated with the development of crustal-scale magmatic systems (e.g., Solano et al., 2014; Jackson et al., 2018).

Numerous ultramafic bodies of magmatic nature are associated with the Ivrea Mafic Complex (e.g., Voshage et al., 1990; Klötzli et al., 2014). Towards the top of the Ivrea Mafic Complex and within the Kinzigite Formation, discordant peridotite-pyroxenite bodies (up to 300 m wide), typically amphibole- and phlogopite-bearing, are exposed (Garuti et al., 2001). They are collectively known as Ultramafic Pipes and most likely formed by primitive alkaline magmas at 288-249 Ma (see also Locmelis et al., 2016; Fiorentini et al., 2018). Along the northern edge of the Mafic Complex, several sill-like peridotite-pyroxenite sequences (up to km-scale in length) crop out (Ferrario et al., 1983; Zaccarini et al., 2014). These peridotite-pyroxenite sequences, also collectively known as Monte Capio sill, are relatively rich in amphibole and phlogopite-free, and formed by H_2O-rich basaltic melts that intruded the lowermost continental crust of the Ivrea-Verbano Zone (Berno et al., 2020). The age of these peridotite-pyroxenite sequences is debated. Klötzli et al. (2014) proposed an age of 314 ± 5 Ma based on U-Pb analyses of zircons separated from an amphibole-garnet gabbro, which could be however genetically unrelated to the peridotite-pyroxenite sequence. Denyszyn et al. (2018) reported a U-Pb zircon age of ~200 Ma, which could also be referred to a zircon recrystallization event, as observed for zircons from other deep levels of the Ivrea-Verbano Zone (e.g., Langone et al., 2017). In its deepest levels, in addition, the Mafic Complex includes several peridotite-pyroxenite sequences considered of magmatic origin (e.g., Quick et al., 2003), whose petrological, geochemical and geochronological characteristics are poorly known.

The main purpose of my PhD is to provide new insights into the processes governing the evolution of primitive mantle magmas emplaced in the lower continental crust. I also wish to acquire new constraints on the compositions of mantle magma sources involved in the generation of the Ivrea Mafic Complex. Hence, I carried out a petrological, geochemical and geochronological investigation of the largest peridotite-pyroxenite sequence of magmatic nature exposed within the Mafic Complex, which is locally referred to as Rocca d'Argimonia (Bertolani and Loschi Ghittoni, 1979). This sequence is enclosed within gabbronorites, which are in turn embedded by the amphibole gabbros of

the lower sector of the Ivrea Mafic Complex (Quick et al., 2003), at a depth corresponding to ~0.8 GPa pressure conditions (Demarchi et al., 1998).

The first year of my PhD was mostly devoted to the petrographic and petrological characterization of the Rocca d'Argimonia peridotite/pyroxenite sequence. The second year of my PhD was mainly focused on the geochemical characterization of the sequence, through definition of trace element and isotopic Nd-Sr-Hf-O compositions of whole-rocks, clinopyroxenes and amphiboles. In particular, the isotopic analyses were carried out during a three-month visit at the Institute of Geology and Geophysics, Chinese Academy of Sciences (Beijing, China). During the third year of my PhD, I obtained new geochronological constraints on formation of the Rocca d'Argimonia sequence by U-Pb isotope zircon investigations. In the last year of my PhD, I also prepared two manuscripts, which represent the two main chapters of my PhD thesis.

The first main chapter of my PhD thesis was published on European Journal of Mineralogy (Antonicelli et al., 2020). This paper deals with the origin of the Rocca d'Argimonia peridotites mostly based on petrological data and on oxygen isotopic compositions of olivine (Antonicelli et al., 2020). The peridotites compositionally range from dunites to harzburgites and minor clinopyroxene-poor lherzolites. Despite the extensive subsolidus re-equilibration under granulite facies conditions, these rocks and the crosscutting gabbronorite dykes typically retain structures and microstructures of magmatic origin. In particular, the harzburgites and the lherzolites are characterized by the presence of poikilitic orthopyroxenes enclosing partially dissolved olivine and minor spinel. The gabbronorite dykes most likely formed by chemically evolved basalts, and show mm-scale thick, orthopyroxenite to websterite reaction zones along the contact with host peridotites. The development of these reaction zones is attributed to a melt-peridotite reaction comprising: (i) dissolution of a mm-scale thick peridotite layer, (ii) orthopyroxenite and websterite crystallization, and (iii) mixing of the melt residual after orthopyroxenite-websterite crystallization with unreacted migrating melt.

The compositional variations of the Rocca d'Argimonia peridotites cannot be related to a magmatic evolution process driven by closed system fractional crystallization. This notion is for instance shown by the $\delta^{18}O_{Ol}$ significantly increasing with decreasing olivine forsterite proportion and with increasing modal orthopyroxene. Most likely, the peridotites record a process of reactive melt flow through a melt-poor olivine-rich crystal mush or a pre-existing dunite of likely magmatic origin. We propose that the reactively migrating melts possessed a substantial crustal component, and that they could be compositionally similar to those forming the gabbronorite dykes. The process of contaminating melt flow is considered to be responsible for the olivine dissolution shown by the poikilitic orthopyroxenes in the harzburgites-lherzolites, and is inferred to have operated at least at

the scale of ~100 meters. The nature of the primitive melt forming the precursor olivine-rich matrix remains unknown.

The second main chapter of my PhD thesis consists of a manuscript entitled "Origin of the peridotite-pyroxenite sequence from Rocca d'Argimonia, Ivrea Mafic Complex (northern Italy)". I wish to submit this manuscript to a scientific journal with high impact factor, such as Journal of Petrology, Contributions to Mineralogy and Petrology, or Lithos. In this manuscript, I refined the petrogenetic scenario depicted in Antonicelli et al. (2020). An age of 286.0 ± 3.0 Ma is suggested for the formation of the Rocca d'Argimonia sequence, based on U-Pb zircon investigations of gabbronorites enclosing the peridotite-pyroxenite sequence. This age is consistent with a two-point Lu-Hf isochron of 285 ± 22 Ma, obtained from clinopyroxene and amphibole separated from a dunite. The Rocca d'Argimonia sequence therefore most likely developed in conjunction with the main phase of Mafic Complex formation, which occurred at 283.5 ± 2.3 Ma, as recently documented by U-Pb zircon investigations by isotope dilution TIMS (Karakas et al., 2019).

Mostly based on Nd-Sr-Hf isotopic compositions of peridotites, pyroxenites, gabbronorite dykes and enclosing gabbronorites, the following sequence of events is formulated for the formation of the Rocca d'Argimonia peridotite-pyroxenite sequence:

1. intrusion of chemically primitive mantle-derived magmas into the lower continental crust;
2. formation of a melt-poor olivine-rich crystal mush by slow cooling, presumably associated with minor assimilation of crustal material;
3. building of the peridotite-pyroxenite sequence in response to reactive migration of crustally contaminated melts. The latter could be compositionally similar to those forming the gabbronorite dykes or be derived from the enclosing gabbronorites.

Similar reactive melt flow relationships, with an early olivine-rich crystal mush percolated by chemically evolved basic melts, were suggested for other peridotite-pyroxenite sequences associated with the Mafic Complex of the Ivrea Verbano Zone, namely the so-called Ultramafic Pipes (Locmelis et al., 2016) and the Monte Capio-Alpe Cevia sequence (Berno et al., 2020). The mineral reaction products in those cases differ in the relatively high proportion of amphibole and, locally, in the presence of phlogopite, most likely in response to involvement of primitive mantle melts with different compositions. Reactive melt flow through an olivine-dominated matrix in the lower crust, associated with crustal contamination, may therefore represent a common process of large-scale magmatic systems growing in extensional (or transtensional) continental settings.

Chapter I: Origin of Rocca d'Argimonia peridotites

Contaminating melt flow in magmatic peridotites from the lower continental crust (Rocca d'Argimonia sequence, Ivrea-Verbano Zone)

Marta Antonicelli, Riccardo Tribuzio, Tong Liu and Fu-Yuan Wu

European Journal of Mineralogy, 32, 587–612

The supplementary material related to this article is available online at:
https://doi.org/10.5194/ejm-32-587-2020-supplement

Abstract

The lower continental crust section of the Ivrea–Verbano Zone (Italian Alps) was intruded by a ~8 km thick gabbroic–dioritic body (Ivrea Mafic Complex) in the Upper Carboniferous–Lower Permian, in conjunction with the post-collisional transtensional regime related to the Variscan orogeny. In the deepest levels of the Ivrea Mafic Complex, several peridotite–pyroxenite sequences considered of magmatic origin are exposed. We present here a petrological–geochemical investigation of the peridotites from the largest magmatic ultramafic sequence of the Ivrea Mafic Complex, locally called Rocca d'Argimonia. In spite of the widespread subsolidus re-equilibration under granulite facies conditions, most likely reflecting a slow cooling evolution in the lower continental crust, the Rocca d'Argimonia peridotites (dunites to harzburgites and minor clinopyroxene-poor lherzolites) typically retain structures and microstructures of magmatic origin. In particular, the harzburgites and the lherzolites typically show poikilitic orthopyroxenes enclosing partially dissolved olivine and minor spinel. Olivine has forsterite proportion diminishing from the dunites to the harzburgites and the lherzolites (90 mol% to 85 mol%) and negatively correlating with $\delta^{18}O$ (+5.8 ‰ to +6.6 ‰). Gabbronorite dykes locally crosscut the peridotites and show millimetre-scale thick, orthopyroxenite to websterite reaction zones along the contact with host rocks. We propose that the Rocca d'Argimonia peridotites record a process of reactive melt flow through a melt-poor olivine-rich crystal mush or a pre-existing dunite. This process was most likely responsible for the olivine dissolution shown by the poikilitic orthopyroxenes in the harzburgites–lherzolites. We infer that the reactively migrating melts possessed a substantial crustal component and operated at least at the scale of ~100 m.

1 Introduction

The processes driving the chemical differentiation of primitive magmas emplaced in the deep sectors of the continental crust are largely unknown. Several recent studies have proposed that the melt evolution in large magma reservoirs predominantly occurs by reactive flow in melt-poor crystal mushes (e.g. Lissenberg and MacLeod, 2016; Jackson et al., 2018). In the lower continental crust, in particular, the intrusion of primitive mantle magmas is expected to generate a region of crystal mush, in which the melt phase may also originate, to a minor extent, from partial melting of the crust (see also Solano et al., 2012). Within mushy magma chambers, buoyant melts are inferred to percolate upwards along crystal boundaries, transporting chemical components and modifyingthe structure and the chemistry of pre-existing crystals. Other studies conversely support the idea that magma evolution in large magmatic systems is controlled by fractional crystallization in long-lived, liquid-dominated magma chambers (e.g. Kruger and Latypov, 2020). The Ivrea Mafic Complex of the Ivrea–Verbano Zone (Italian Alps) is an excellent natural laboratory to assess the lower crust processes associated with the development of crustalscale magmatic systems (Quick et al., 1992; Sinigoi et al., 2011, 2016; Solano et al., 2014; Jackson et al., 2018). The Ivrea Mafic Complex consists of a ~8 km thick gabbroic–dioritic intrusion, developed in conjunction with the postcollisional transtensional regime of the Variscan orogeny (e.g. Handy et al., 1999; Wilson et al., 2004). In its deepest levels, the Ivrea Mafic Complex includes several peridotite–pyroxenite sequences considered of magmatic origin (e.g. Quick et al., 2003), whose petrological characteristics are poorly known. The present study wishes to provide new insights into the processes governing the evolution of primitive mantle magmas emplaced in the lower continental crust. For this purpose, we carried out a petrological–geochemical investigation of the peridotites from the largest magmatic ultramafic sequence exposed within the Ivrea Mafic Complex, which is locally referred to as Rocca d'Argimonia (Lensch, 1968; Bertolani and Loschi Ghittoni, 1979). This sequence comprises peridotites characterized by the widespread occurrence of poikilitic orthopyroxenes. Similar microstructures in other ultramafic magmatic sequences from the upper continental crust have been recently related to an open-system magmatic evolution driven by reactive melt flow (Barnes et al., 2016; Kaufmann et al., 2018) or by wall-rock crustal contamination (Mao et al., 2019). We also acquired relevant information about the Rocca d'Argimonia peridotite-forming processes by investigating orthopyroxene-rich reaction zones that developed along the contacts between the peridotites and crosscutting gabbronorite dykes. Based on petrographic observations and mineral - whole-rock major element chemistry, we propose that the development of orthopyroxene in the Rocca d'Argimonia peridotites was related to reactive melt flow through a melt-poor olivine rich crystal mush or a pre-existing dunite. Because the peridotite olivines

show significant variations in oxygen isotopic signature, we also infer that the reactively migrating melts possessed a substantial crustal component.

2 Geological framework

The Ivrea–Verbano Zone (Fig. 1) from the inner arc of western Italian Alps exposes a nearly complete section of the pre-Alpine, lower continental crust (e.g. Sinigoi et al., 2016; Pistone et al., 2017). To the west and northwest, the Ivrea–Verbano Zone is in tectonic contact with the Austroalpine domain, which typically exhibits widespread tectono-metamorphic transformations related to the Alpine orogenic evolution (e.g. Schmid, 2017), through the Insubric tectonic lineament. To the south and southeast, two tectonic lineaments, namely the Cossato–Mergozzo–Brissago and the Pogallo Lines, separate the Ivrea–Verbano Zone from the Serie dei Laghi, which represents the upper section of the pre-Alpine continental crust (e.g. Boriani and Giobbi, 2004).

The southwestern sector of the Ivrea–Verbano Zone (Fig. 1) consists of a ~8 km thick gabbroic–dioritic sequence (Ivrea Mafic Complex) intruding a granulite to amphibolite facies basement (e.g. Quick et al., 1992; Sinigoi et al., 2011), in conjunction with the post-collisional transtensional regime related to the Variscan orogeny (e.g. Handy et al., 1999; Wilson et al., 2004). The basement, locally known as Kinzigite Formation, is made up of metasediments (metapelites with subordinate metagreywackes and impure marbles), minor metabasites and, locally, mantle peridotite blocks (e.g. Quick et al., 1995; Redler et al., 2013). In the Val Strona di Omegna section, adjacent to the northern termination of the Ivrea Mafic Complex, the basement rocks show pressure and temperature conditions gradually diminishing from ~0.9 GPa and ~940°C near the Insubric Line to ~0.5 GPa and ~650°C near the Cossato–Mergozzo–Brissago line (see also Kunz and White, 2019). The onset of this metamorphic gradient and the main phase of Ivrea Mafic Complex formation were inferred to occur at 316 ± 3 Ma (Ewing et al., 2013) and 283.5 ± 2.3 Ma (Karakas et al., 2019).

The Ivrea Mafic Complex (Fig. 1) was subdivided into two stratigraphically overlying units (Quick et al., 2003). The Lower Ivrea Mafic Complex is mostly composed of amphibole gabbros that make up the southwestern sector of the intrusion. It includes the peridotite–pyroxenite sequence of Rocca d'Argimonia (Lensch, 1968; Bertolani and Loschi Ghittoni, 1979), which was considered of magmatic origin (see also Sinigoi et al., 1991). The Upper Ivrea Mafic Complex mainly consists of gabbronorites and, towards the roof, diorites. The lowest level of the Upper Ivrea Mafic Complex, also referred to as "paragneiss-bearing belt", comprises metasedimentary septa and peridotite–pyroxenite silllike bodies (Rivalenti et al., 1975; Voshage et al., 1990; Sinigoi et al., 1995, 1996). The metasedimentary septa are interpreted as remnants of the Kinzigite Formation that underwent substantial extraction of SiO_2-rich melts in response to the interaction with melts forming the Ivrea Mafic Complex. The paragneiss-bearing belt also encloses a huge mantle sequence defining a 4.5 km long and 0.8 km wide lens, which is known as Balmuccia peridotite massif (Quick et al., 1995). This mantle sequence is mostly made up of clinopyroxene poor lherzolites (e.g. Shervais and Mukasa,

1991) containing replacive dunite bodies (Mazzucchelli et al., 2009) and two major sets of pyroxenite veins dominated by either Cr-diopside or Al-augite (e.g. Voshage et al., 1988; Rivalenti et al., 1995; Mukasa and Shervais, 1999).

Towards the top of the Ivrea Mafic Complex and within the Kinzigite Formation, discordant peridotite–pyroxenite bodies (up to 300 m wide), typically amphibole- and phlogopite-bearing, are exposed (Garuti et al., 2001). They are collectively known as the ultramafic pipes and most likely formed by primitive alkaline magmas at 288–249 Ma (see also Locmelis et al., 2016; Fiorentini et al., 2018). Along the northern edge of the Ivrea Mafic Complex, near the Insubric Line, several sill-like peridotite–pyroxenite sequences (up to kilometre scale in length) crop out (Ferrario et al., 1983; Zaccarini et al., 2014). These peridotite–pyroxenite sequences, also collectively known as Monte Capio sill, are relatively rich in amphibole and phlogopite-free and formed by H_2O-rich basaltic melts that intruded the lowermost continental crust of the Ivrea–Verbano Zone (Berno et al., 2020). The age of these peridotite–pyroxenite sequences is debated. Klötzli et al. (2014) proposed an age of 314 ± 5 Ma based on U–Pb analyses of zircons separated from an amphibole–garnet gabbro, which could be however genetically unrelated to the peridotite–pyroxenite sequence. Denyszyn et al. (2018) reported a U–Pb zircon age of ~200 Ma, which could also be referred to as a zircon recrystallization event, as observed for zircons from other deep levels of the Ivrea–Verbano Zone (e.g. Vavra et al., 1999; Zanetti et al., 2016; Langone et al., 2017).

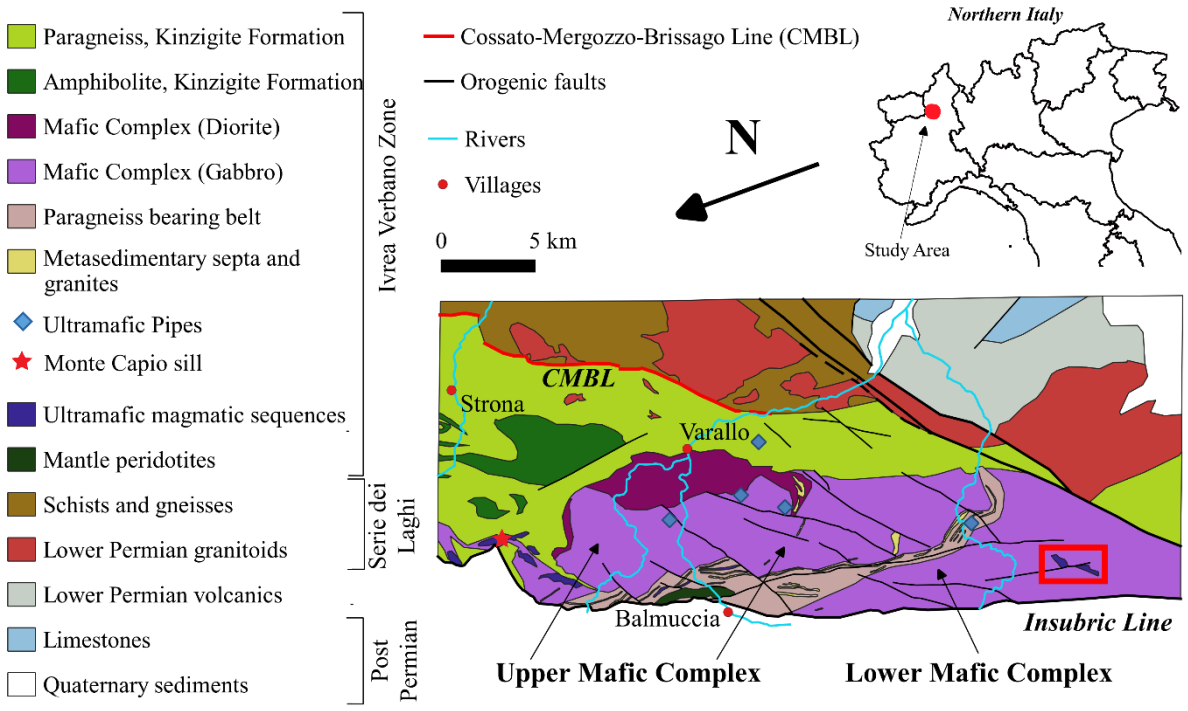

Figure 1. Geological map of the central Ivrea–Verbano Zone and Serie dei Laghi, simplified after Sinigoi et al. (2016). Location of the ultramafic pipes after Guergouz et al. (2018). The north orientation aims at elucidating the inferred Permian stratigraphy. The red frame refers to the location of the Rocca d'Argimonia sequence (see Fig. 2).

3 The Rocca d'Argimonia sequence: field relationships

The Rocca d'Argimonia ultramafic rocks are enclosed within gabbronorites, which are in turn embedded in the amphibole gabbros of the Lower Ivrea Mafic Complex (Quick et al., 2003). In particular, two major ultramafic rock bodies, characterized by up to 100 m thick peridotite–pyroxenite alternations, are exposed near Bielmonte village (Fig. 2). The peridotites are locally characterized by the widespread occurrence of poikilitic orthopyroxenes, typically 0.5–2.0 cm in size (Fig. 3a). The poikilitic orthopyroxenes are in places aligned to define a foliation that is subparallel to the inferred orientation of the peridotite–pyroxenite surface contacts (Fig. 2). Olivine-depleted bands, characteristically a few tens of centimetres thick, are locally associated with the peridotites rich in poikilitic orthopyroxene. The pyroxenites are plagioclase-bearing, medium-grained rocks that are modally dominated by orthopyroxene (see also Bertolani and Loschi Ghittoni, 1979).

The peridotites are crosscut by up to 0.3 m thick gabbronorite dykes with sharp planar boundaries (Fig. 3b). The dykes are oriented at a high angle with respect to the orthopyroxene foliation of host peridotites. The gabbronorite–peridotite contact is characterized by a 3–5 mm thick pyroxene-rich zone. Sinuous gabbronorite dykelets (≤2 cm thick) also occur in places, in both the peridotites and adjacent pyroxenites. Subparallel to the contact surface with host peridotites, the gabbronorite dykes exhibit a layering defined by grain size and/or plagioclase/pyroxene modal variations and, locally, a foliation defined by weak alignment of plagioclase and pyroxene. Some of the dykes show pyroxenes elongated nearly perpendicularly to the wall peridotite surface.

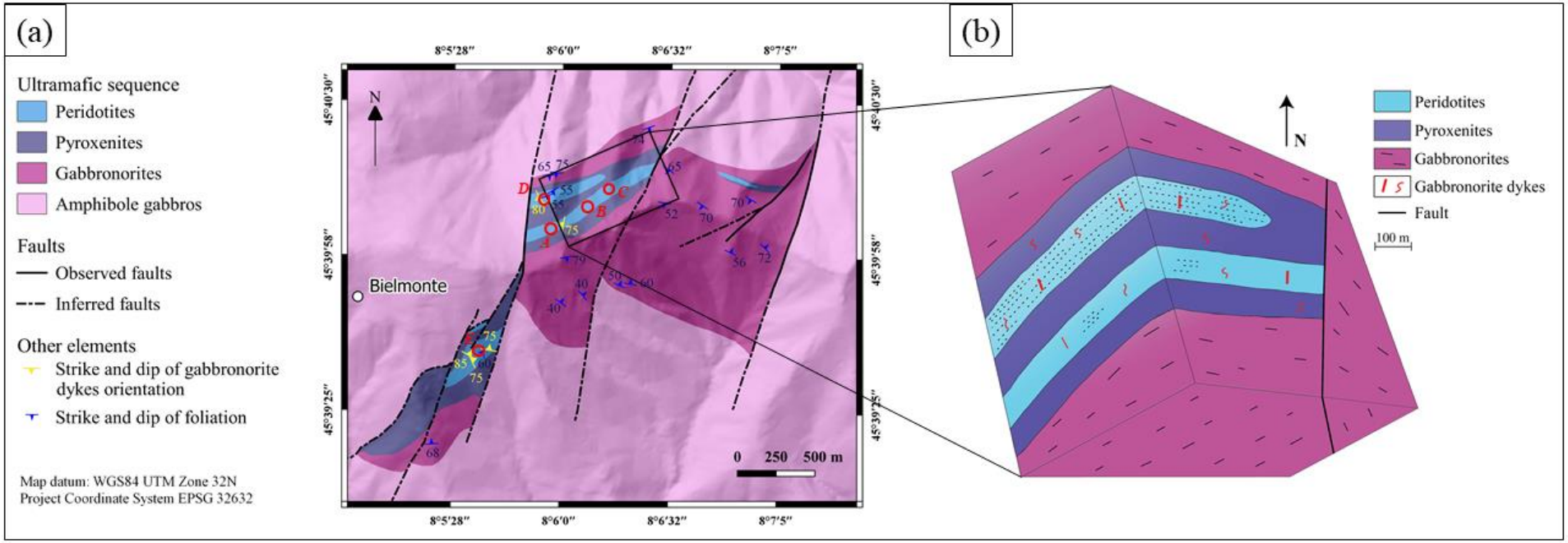

Figure 2. (a) Geological map of the Rocca d'Argimonia area, compiled after Lensch (1968) and Quick et al. (2003), and new field investigations. The empty dots represent the sampling sites. A: peridotites BI10/1 and BI10/3, and gabbronorite BI10/3; B: peridotites BI4/1 and BI4/3; C: peridotite BI5/1; D: peridotites BI2/1, BI2/5, BI2/7, BI6/2 and BI30/5, and gabbronorites BI2/5 and BI8/1; E: gabbronorite BI50/3. Location of Bielmonte village is also reported. (b) Synthetic block diagram illustrating the relationships between the different rock types of the Rocca d'Argimonia sequence; the dotted lines within the peridotites represent domains rich in poikilitic orthopyroxene.

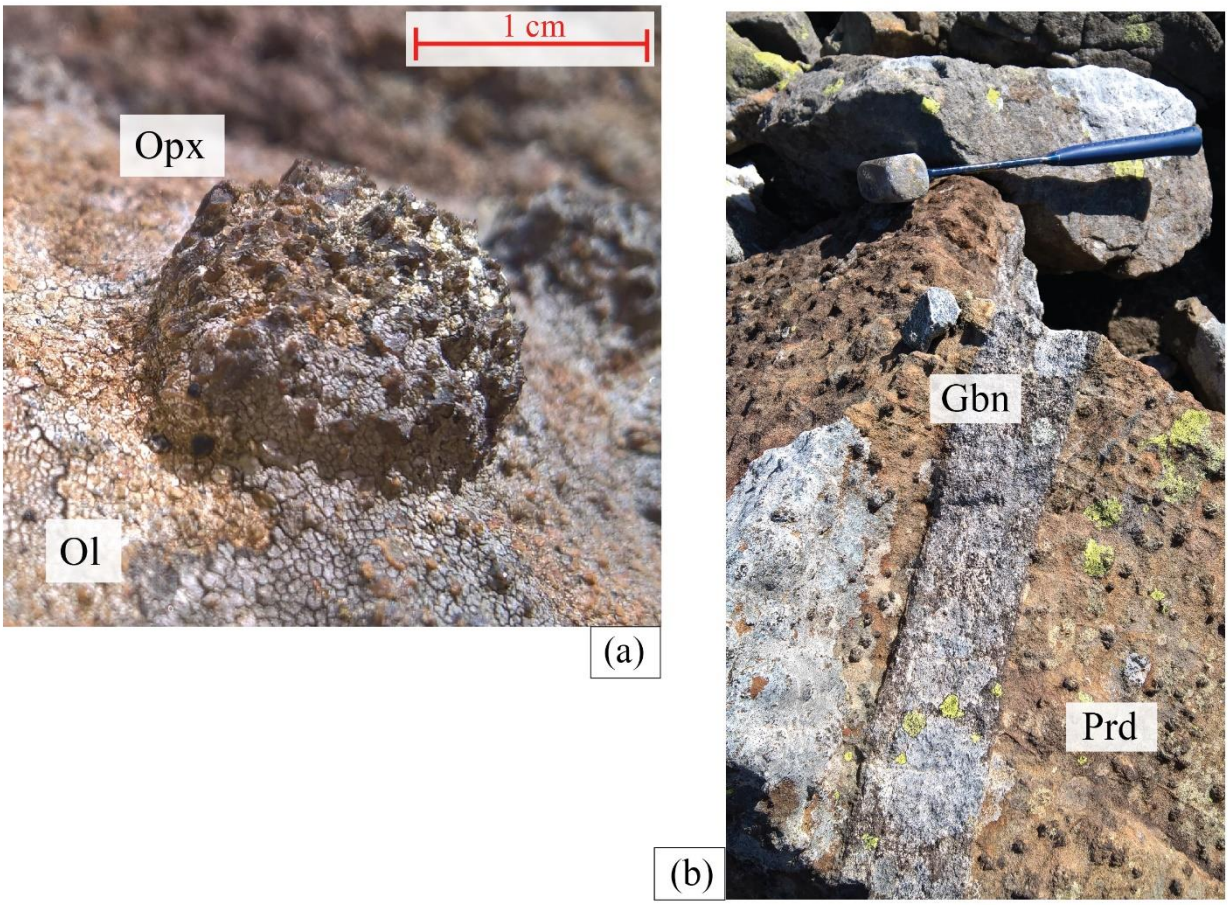

Figure 3. (a) Poikilitic orthopyroxene (1 cm in diameter) in a peridotite, evidenced by the preferential erosion of host olivine-rich matrix. (b) Gabbronorite dyke (Gbn) displaying sharp planar contacts against host peridotite (Prd), in turn displaying poikilitic orthopyroxenes.

4 Analytical methods

Whole-rock major element analyses of selected peridotites and gabbronorite dykes (Table 1) were carried out at Activation Laboratories (Ancaster, Ontario), following commercial package 4Lithores. Sample preparation implies a lithium metaborate–tetraborate fusion and digestion in 5 % nitric acid. Analyses of SiO_2, Al_2O_3, Fe_2O_3, MnO, MgO, CaO, Na_2O, K_2O, TiO_2 and P_2O_5 were performed by inductively coupled plasma optical emission spectroscopy. Cr_2O_3 and NiO contents were measured by inductively coupled plasma mass spectroscopy. Detection limits are 0.01 wt% for SiO_2, Al_2O_3, Fe_2O_3, MgO, CaO, Na_2O, K_2O and P_2O_5, 0.001 wt% for MnO and TiO_2, and 0.003 wt% for Cr_2O_3 and NiO.

The main mineral phases (olivine, orthopyroxene, clinopyroxene, amphibole spinel and plagioclase) of the selected rock samples were analysed for Si, Ti, Al, Cr, Fe, Mn, Ni, Mg, Ca, Na and K with an electron microprobe (JEOL 8200 Super Probe) at Dipartimento di Scienze della Terra, Università degli Studi di Milano, in wavelength-dispersive spectrometry mode. Electron microprobe operating conditions were 15 kV accelerating voltage and 5 nA beam current, with counting times of 30 s on the peaks and 10 s on the backgrounds. We used a ~1 μm focused beam and natural minerals as standards, namely grossular for Si, Ca and Al; fayalite for Fe; forsterite-rich olivine for Mg; rhodonite for Mn; ilmenite for Ti; omphacite for Na; K-feldspar for K; niccolite for Ni; and pure chromium metal for Cr.

Oxygen isotopic compositions of olivine from selected peridotites (Table 8) were analysed in situ using CAMECA IMS-1280 ion microprobe at the Institute of Geology and Geophysics – Chinese Academy of Sciences, Beijing. Olivine grains were separated and embedded in epoxy, adjacent to grains of a San Carlos olivine standard. The Cs+ primary beam was accelerated at 10 kV with an intensity of ~1.5 nA. The spot size was 10–15 μm in diameter. An electron gun was used to compensate for sample charging during analysis. Secondary ions were extracted with a ~10 kV potential. Oxygen isotopes were measured in multi-collector mode with two off-axis Faraday cups with each analysis consisting of 16 cycles × 4 s counting time. The instrumental mass fractionation factor is corrected using San Carlos olivine standard with $\delta^{18}O_{VSMOW} = 5.25 \pm 0.05$ ‰ (Eiler et al., 1995). Point-to-point uncertainty for $\delta^{18}O$ was typically <0.4 ‰ (2 SE). For each peridotite, oxygen isotopic analyses were conducted at the core of 18–20 olivine grains. The measured $\delta^{18}O_{VSMOW}$ of the San Carlos olivine standard during this study is 5.27 ± 0.12 ‰ (95 % confidence level, n = 20).

5 Results

The main petrographic characteristics and GPS coordinates of rock samples selected for the present study are reported in Table 9. Location of samples is also shown in Fig. 2a. Mineral proportions were evaluated based on mass balance calculations, combining whole-rock and mineral chemical compositions. In particular, we used a least squares mixing programme to reproduce the whole-rock chemistry based on compositions of the minerals constituting the rock (see Table 9 caption for details about calculations). Computed whole-rock compositions based on observed mineral compositions and estimated mineral proportions are listed in Table A1.

5.1 Peridotites

5.1.1 Petrographic characteristics

The peridotites free of poikilitic orthopyroxene are dunites (Fig. 4a). They mostly consist of olivine polygonal grains (average size 2–3 mm) defining a nearly granoblastic structure and include accessory clinopyroxene, spinel, amphibole and orthopyroxene. Clinopyroxene, spinel and amphibole grains are smaller than olivine grains (Table 9) and typically display nearly equant morphology. Spinel also occurs within olivine, with subhedral to euhedral morphology. Orthopyroxene (1 vol%–5 vol%) has variable grain size and, characteristically, anhedral morphology. It may form small grains interstitial among olivines to large grains with anhedral morphology (up to 7 mm in thin section).

The peridotites rich in poikilitic orthopyroxenes (7 vol%–15 vol%) are harzburgites (Fig. 4a). The poikilitic orthopyroxenes enclose a substantial amount of olivine and minor spinel (Fig. 5a). In particular, modal point counting applied to poikilitic orthopyroxenes showed that olivine and spinel correspond to 35 vol%–40 vol% and 6 vol%–9 vol%, respectively, of the orthopyroxene volume. Olivine within poikilitic orthopyroxene shows variable grain size, rounded to elliptical shape, and frequent embayed boundaries. Conversely, olivine external to poikilitic orthopyroxenes is nearly equigranular and with polygonal morphology. Within a single poikilitic orthopyroxene, the elliptical olivine inclusions are locally subparallel. A single orthopyroxene may also host olivine clusters showing the same optical orientation, thereby indicating that they were part of a pre-existing larger olivine grain. Spinel within and external to poikilitic orthopyroxenes typically has similar grain size and nearly equant morphology. Spinel occurring along the contact between olivine and enclosing orthopyroxene is distinct in the elongated shape. Similar to the dunites, the harzburgites contain accessory amounts of clinopyroxene and amphibole with nearly equant morphology.

Samples collected as olivine-depleted bands during field investigations have 37 vol%–54 vol% olivine, 28 vol%–51 vol% orthopyroxene and 5 vol%–14 vol% clinopyroxene. They are therefore classified as lherzolites and olivine websterites (Fig. 4a). For the sake of simplicity, they are hereafter

referred to as lherzolites. Orthopyroxene and clinopyroxene mostly occur as nearly equant to subprismatic grains associated with polygonal olivine, thereby defining a nearly granoblastic structure with an average grain size of 1–2 mm. Orthopyroxene also occurs as rare poikilitic grains (up 8 mm) enclosing olivine and minor spinel, similar to the harzburgites. The lherzolite showing the highest clinopyroxene amounts locally comprises poikilitic clinopyroxene grains (5–7 mm) including sub-prismatic to rounded olivine, nearly equant minor spinel and, sporadically, subprismatic orthopyroxene (Fig. 5b). The lherzolites also contain accessory amounts of spinel and amphibole, which display nearly equant morphology.

In all peridotite samples, pyroxenes are exsolved (Fig. 5b). In particular, clinopyroxene exhibits a few micrometres thick exsolution lamellae of orthopyroxene and spinel. The outer regions of the clinopyroxene grains also locally include domains free of exsolution lamellae that contain minor amounts of globular amphibole (tens to hundreds of micrometres in size) and vermicular spinel (typically a few micrometres in thickness). Orthopyroxene has a few micrometres thick lamellae of clinopyroxene and spinel. All selected samples include accessory amounts of Fe–Ni–Cu sulfides (pyrrhotite, pentlandite and minor chalcopyrite), which mostly occur along mineral grain boundaries, frequently in association with spinel. According to Bertolani and Loschi Ghittoni (1979), these sulfides are in places accompanied by cubanite and sphalerite.

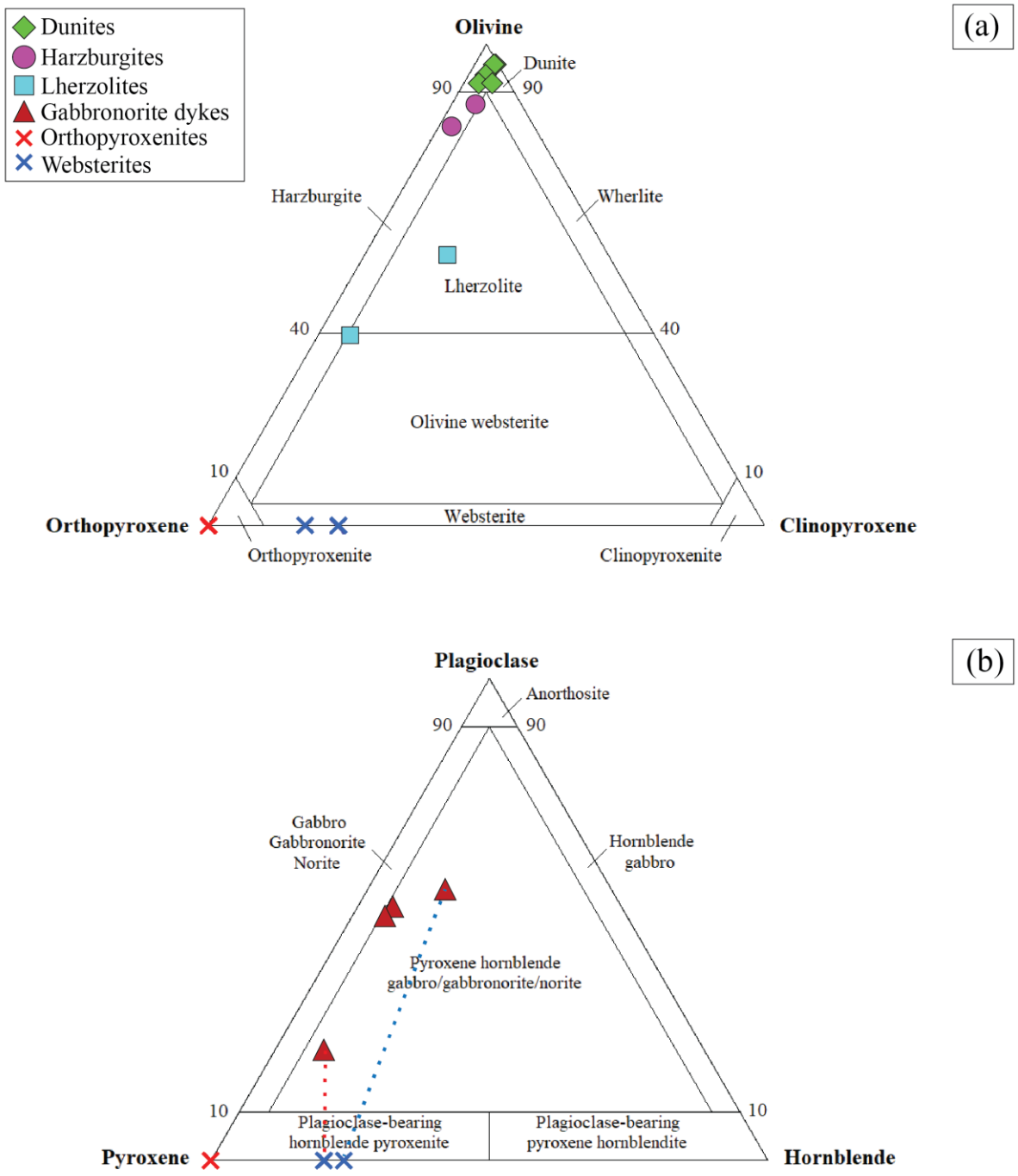

Figure 4. (a) Peridotite modal compositions (vol%) reported in the olivine–orthopyroxene–clinopyroxene classification diagram of ultramafic rocks. The compositions of orthopyroxenite and websterite micro-layers formed along the contacts between the peridotites and crosscutting gabbronorite dykes are also reported. (b) Modal compositions of hornblende gabbronorite dykes (vol%) reported in the plagioclase-total pyroxene–amphibole classification diagram of gabbroic rocks. The compositions of orthopyroxenite and websterite micro-layers formed along the contacts between gabbronorite dykes and peridotites are also reported. The dotted tie lines refer to the gabbronites and physically adjacent websterite micro-layers (blue: sample BI2/5; red: sample BI10/3).

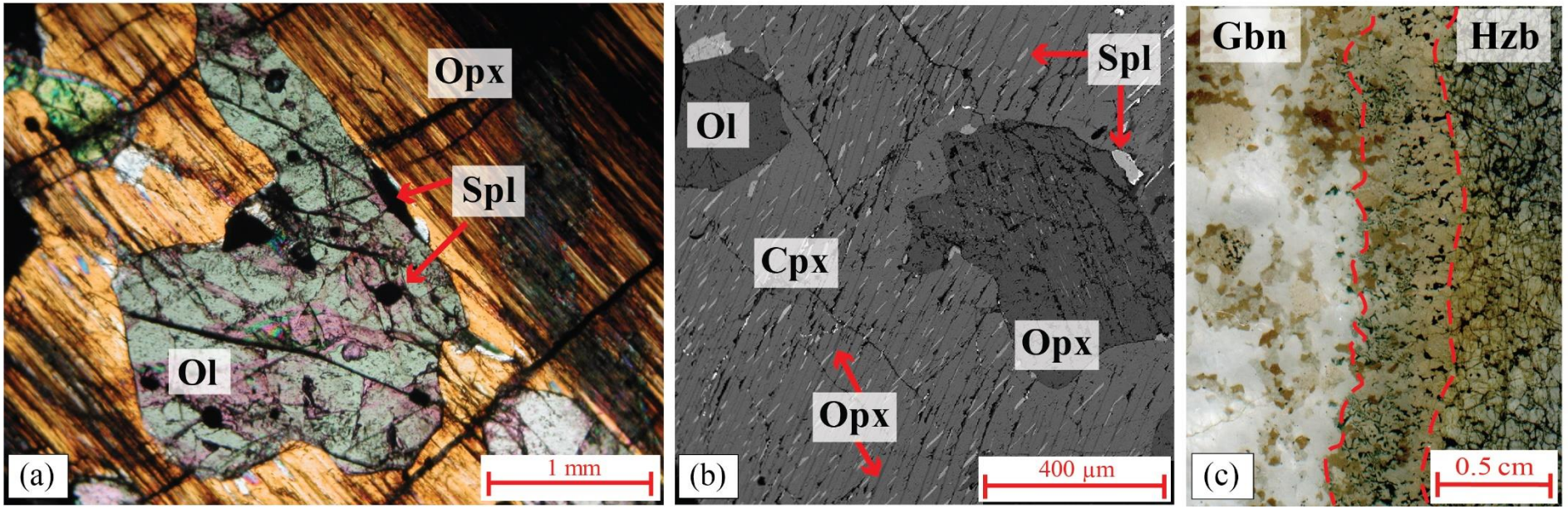

Figure 5. (a) Micro-photo showing a poikilitic orthopyroxene from harzburgite BI2/7 (crossed nicols). Olivine inclusions show embayed boundaries or rounded to elliptical shape. The largest olivine inclusion encloses several spinel grains with euhedral–subhedral morphology. Spinel with anhedral elongated morphology is present along the contact between olivine and enclosing orthopyroxene. Mineral abbreviations after Whitney and Evans (2010). (b) Back-scattered electron image showing a poikilitic clinopyroxene from lherzolite BI6/2. The clinopyroxene encloses olivine and orthopyroxene. In addition, spinel with elongated to nearly equant morphology is present along the contact between olivine–orthopyroxene and host clinopyroxene. The poikilitic clinopyroxene exhibits a few micrometres thick exsolution lamellae of orthopyroxene and spinel. The enclosed orthopyroxene is also exsolved, with a few micrometres thick lamellae of clinopyroxene and spinel. Mineral abbreviations after Whitney and Evans (2010). (c) Scanned thin section image showing the contact zone between harzburgite BI2/5 (Hzb) and crosscutting gabbronorite dyke (Gbn). The contact zone is bounded by red dashed lines and consists of spinel-bearing orthopyroxenite towards the harzburgite and of spinel-bearing hornblende websterite towards the gabbronorite. The gabbronorite dyke shows granoblastic structure.

5.1.2 Whole-rock chemical compositions

The peridotites show low loss on ignition values (≤1.1 wt%), in agreement with the negligible low temperature alteration of selected samples. The Mg# [molarMg=(Mg+Fe^{2+}_{tot}) × 100] decreases from the dunites (87–90) to the harzburgites (86–87) and the lherzolites (84–85). Al_2O_3 shows a rough negative correlation with Mg# (Fig. 6). CaO is 0.6 wt%–1.2 wt% in the dunites and the harzburgites and 1.7 wt%–3.4 wt% in the lherzolites. Dunite BI5/1 exhibits lower SiO_2 and higher Cr_2O_3 (Table 1) than the other peridotites, in agreement with the relatively high spinel proportion observed for this sample (cf. Table 9).

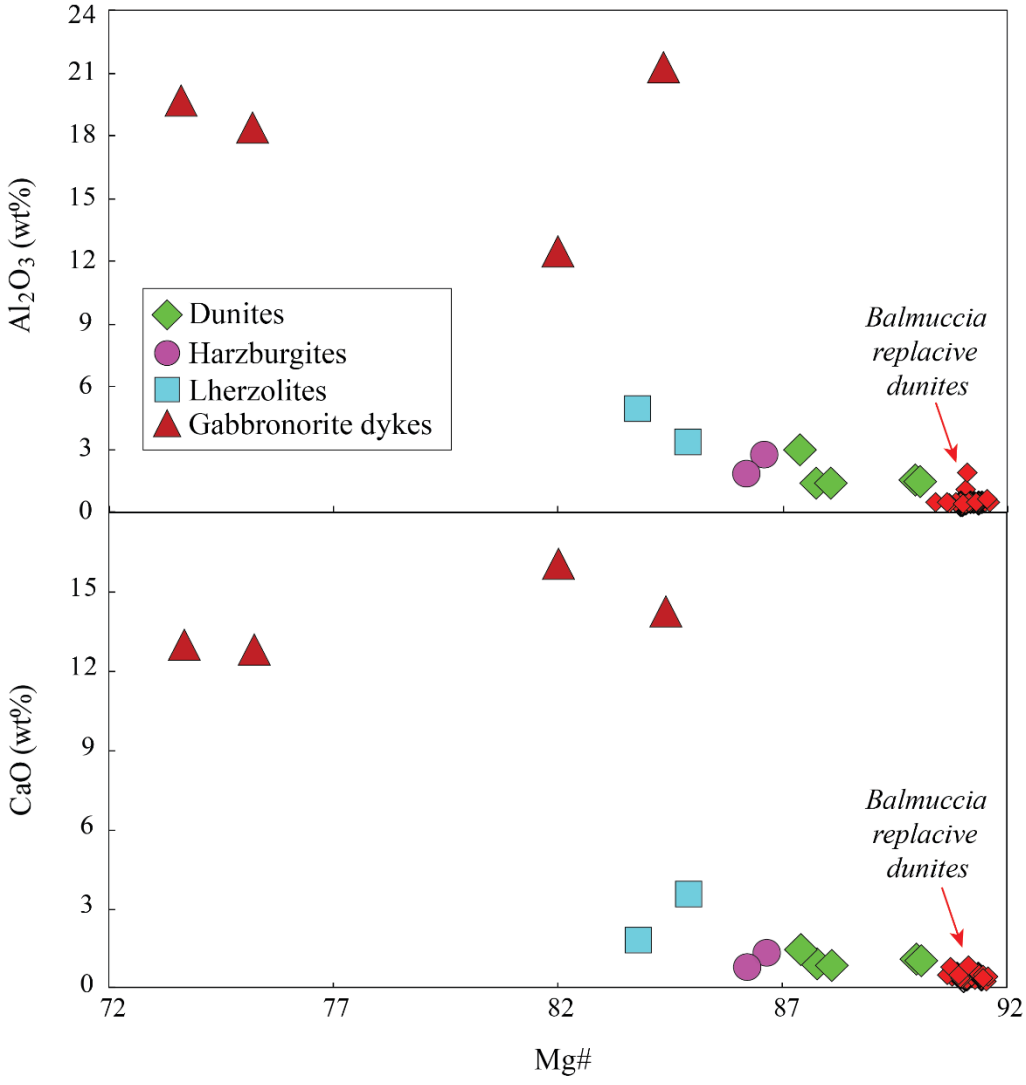

Figure 6. Diagrams showing the whole-rock chemical compositions of the selected samples from the Rocca d'Argimonia sequence. Al_2O_3 and CaO, calculated on anhydrous basis, versus Mg# [molarMg=(Mg+Fe^{2+}_{tot}) × 100]. The compositions of mantle replacive dunites of the Balmuccia peridotite massif (Mazzucchelli et al., 2009) are reported for comparative purposes.

Sample	BI4/3	BI4/1	BI10/3	BI10/1	BI5/1	BI2/1	BI2/7	BI6/2	BI30/5	BI2/5	BI10/3	BI8/1	BI50/3
Rock type	**Dunites**					**Harzburgites**		**Lherzolites**		**Gabbronorite dykes**			
SiO_2	38.2	38.4	39.3	39.2	37.1	39.5	40.1	43.5	44.7	45.9	47.8	49.1	47.0
Al_2O_3	1.48	1.51	1.39	1.40	3.00	2.66	1.75	3.30	4.86	21.3	12.5	18.4	19.3
Fe_2O_3 (tot)	10.4	10.5	12.1	12.7	12.4	13.0	13.3	12.5	13.0	4.04	6.69	6.50	7.27
MnO	0.14	0.14	0.16	0.16	0.15	0.17	0.17	0.17	0.18	0.07	0.13	0.12	0.13
MgO	47.5	47.5	45.3	45.8	43.2	42.6	42.2	35.6	34.0	11.0	15.4	10.0	10.3
CaO	0.92	0.96	0.75	0.82	1.38	1.17	0.63	3.42	1.67	14.1	16.0	12.7	12.6
Na_2O	0.05	0.05	0.04	0.04	0.06	0.06	0.04	0.13	0.10	1.27	0.68	1.57	1.61
K_2O	<0.01	<0.01	<0.01	<0.01	<0.01	<0.01	<0.01	<0.01	<0.01	0.06	0.05	0.13	0.12
TiO_2	0.05	0.05	0.04	0.05	0.09	0.10	0.05	0.17	0.19	0.33	0.43	0.40	0.39
Cr_2O_3	0.64	0.65	0.59	0.52	1.27	0.88	0.92	0.41	0.70	0.02	0.10	0.02	0.01
NiO	0.31	0.31	0.27	0.28	0.34	0.24	0.23	0.16	0.18	0.08	0.08	0.03	0.02
P_2O_5	0.01	<0.01	<0.01	<0.01	<0.01	0.01	0.01	<0.01	0.02	<0.01	<0.01	<0.01	<0.01
LOI	<0.01	0.20	0.11	<0.01	1.12	0.05	0.46	0.83	0.52	1.80	0.92	0.95	2.03
Total	99.7	100.2	100.0	100.9	100.0	100.4	99.8	100.1	100.1	100.0	100.7	99.8	100.8
Mg#	90.1	90.0	88.1	87.8	87.4	86.7	86.3	84.9	83.8	84.4	82.0	75.2	73.7

Table 1. Whole-rock chemical compositions of selected samples.

5.1.3 Mineral chemical compositions

The peridotite minerals typically show minor intra-grain and within-sample chemical variability. The forsterite proportion of olivine (Fig. 7) decreases from the dunites (90 mol%–88 mol%) to the harzburgites (87 mol%) and the lherzolites (85 mol%). In contrast, olivine NiO (0.24 wt%–0.36 wt%) shows no systematic variations among the different peridotite types. In the harzburgites and the lherzolites, olivines within and external to poikilitic pyroxenes have similar compositions (Table 2).

The poikilitic orthopyroxene in the harzburgites–lherzolites show no significant chemical zoning (Table 3). Both orthopyroxene and clinopyroxene have Mg# [100×molarMg=(Mg+Fe^{2+}_{tot})], mol%] decreasing from the dunites to the harzburgites and the lherzolites and linearly correlating (Fig. 8) with Cr# [100×Cr/(Cr+Al), mol%]. Within a single lherzolite sample, pyroxenes showing different microstructures are chemically nearly homogeneous (see also Table 4). Overall, orthopyroxene contains 0.3 wt%–0.4 wt% CaO, and clinopyroxene has 0.3 wt%–0.6 wt% Na_2O and 0.5 wt%–0.7 wt% TiO_2.

According to the amphibole nomenclature of Leake et al. (1997), amphibole is pargasite to titanian pargasite in dunites and titanian pargasite in harzburgites and lherzolites (Table 5). Amphibole Mg# and Cr# roughly decrease from the dunites to the harzburgites and the lherzolites.

Spinels from the harzburgites and the dunites show overlapping Cr# (16–31 and 20–28, respectively; Fig. 9). In the harzburgites, spinels within and external to poikilitic orthopyroxenes have similar compositions (Table 6). Spinel from the lherzolites is distinct in the low Cr# of ~11–13. In all the peridotites, TiO_2 in spinel is low (0.03 wt%–0.16 wt%). The spinel Cr# yields a rough linear correlation when plotted against the forsterite proportion of coexisting olivine.

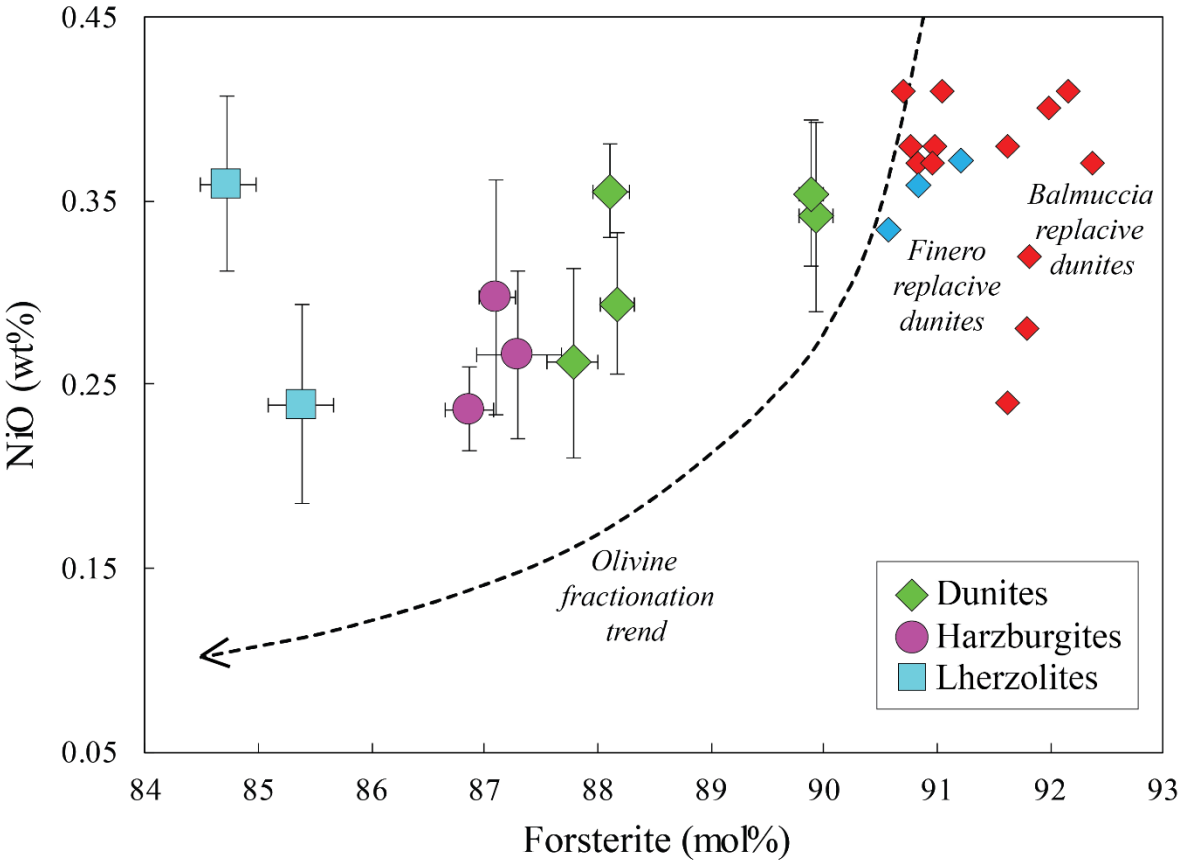

Figure 7. Plot of NiO (wt%) versus forsterite proportion (mol%) of olivine from the Rocca d'Argimonia peridotites. Data are averaged per sample; error bars represent the standard deviation of the mean value (2σ). The compositions of olivine from mantle replacive dunites of the Balmuccia and Finero mantle sequences (Mazzucchelli et al., 2009; Bussolesi et al., 2019; Corvò et al., 2020) are reported for comparative purposes. Olivine fractionation trend after Su et al. (2016).

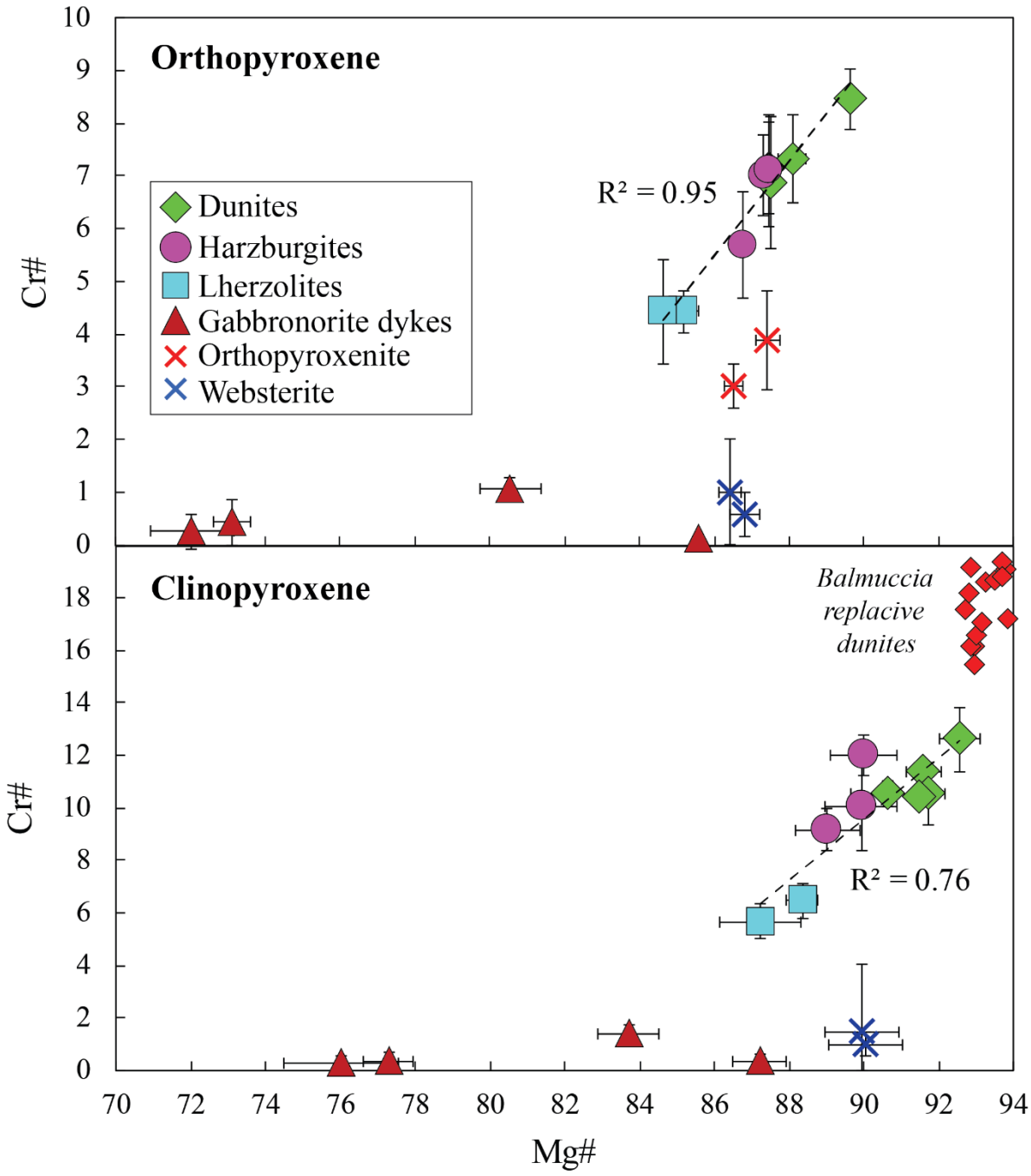

Figure 8. Plot of Cr# [100×Cr/(Cr+Al), mol%] versus Mg# [100×molarMg=(Mg+Fe^{2+}_{tot})] of orthopyroxene and clinopyroxene from the selected samples of the Rocca d'Argimonia sequence. Data are averaged per sample; error bars represent the standard deviation of the mean value (2σ). The compositions of clinopyroxene from mantle replacive dunites of the Balmuccia peridotite massif (Mazzucchelli et al., 2009) are reported for comparative purposes.

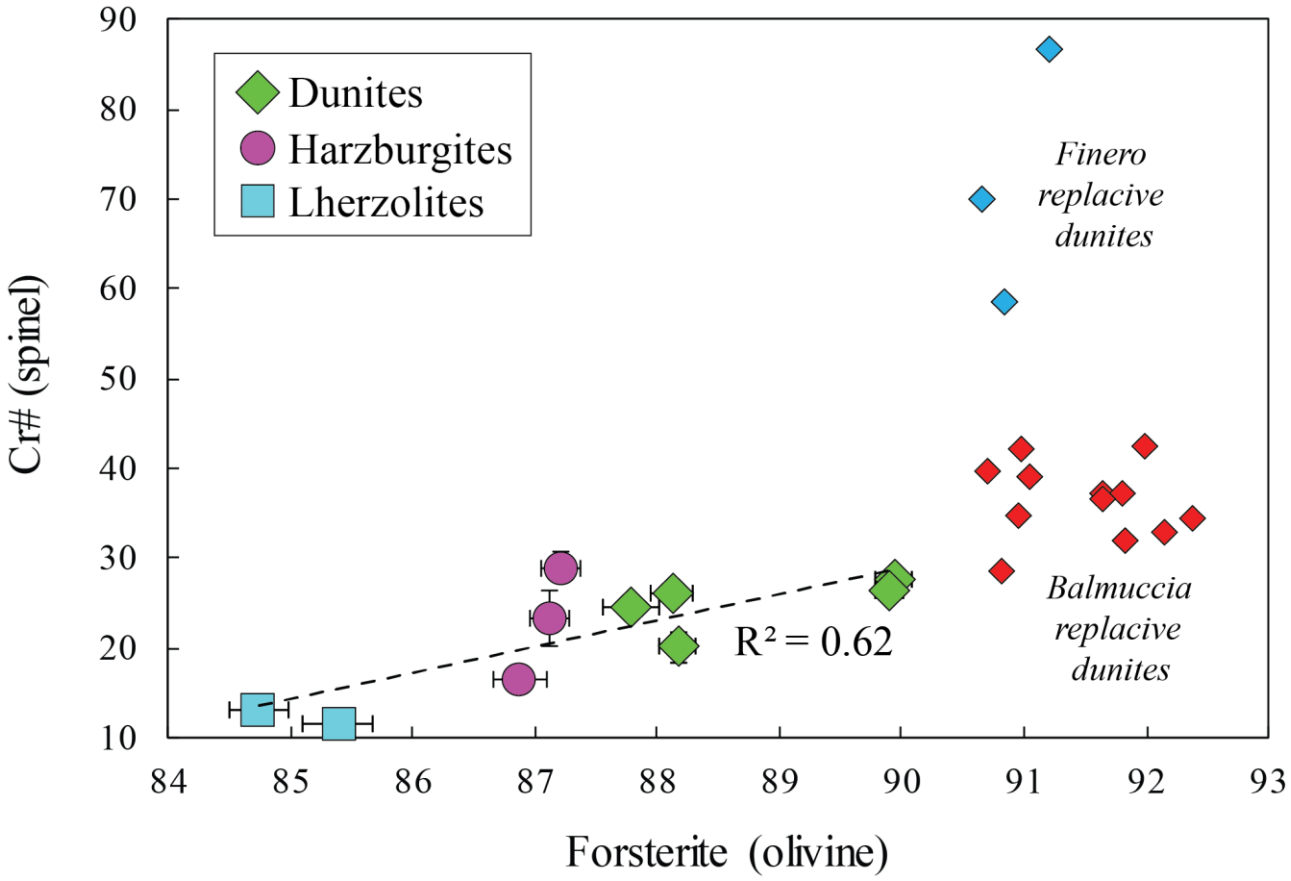

Figure 9. Plot of Cr# [100×Cr/(Cr+Al), mol%] of spinel versus forsterite proportion of coexisting olivine (mol%) for the Rocca d'Argimonia peridotites. Data are averaged per sample; error bars represent the standard deviation of the mean value (2σ). The compositions of spinel–olivine pairs from mantle replacive dunites of the Balmuccia and Finero mantle sequences (Mazzucchelli et al., 2009; Bussolesi et al., 2019; Corvò et al., 2020) are reported for comparative purposes.

Sample	BI4/3		BI4/1		BI10/3		BI10/1		BI5/1		BI2/5		BI2/5 (in poikilitic Opx)		BI2/1		BI2/1 (in poikilitic Opx)		BI2/7		BI2/7 (in poikilitic Opx)		BI6/2		BI6/2 (in poikilitic Cpx)		BI30/5		BI30/5 (in poikilitic Opx)	
Rock type	**Dunite**		**Dunite**		**Dunite**		**Dunite**		**Dunite**		**Harzburgite**		**Harzburgite**		**Harzburgite**		**Harzburgite**		**Harzburgite**		**Harzburgite**		**Lherzolite**		**Lherzolite**		**Lherzolite**		**Lherzolite**	
No.	8	SD	12	SD	9	SD	10	SD	11	SD	2	SD	6	SD	4	SD	5	SD	5	SD	9	SD	5	SD	1	SD	8	SD	8	SD
SiO_2	40.52	0.25	41.05	0.26	40.80	0.24	40.37	0.15	40.57	0.24	40.40	0.01	40.55	0.14	40.47	0.12	40.44	0.10	40.63	0.14	40.43	0.21	40.42	0.14	39.91	-	40.07	0.27	40.14	0.27
Al_2O_3	0.00	0.00	0.01	0.01	0.01	0.01	0.01	0.01	0.01	0.01	0.01	0.01	0.02	0.01	0.00	0.01	0.01	0.01	0.01	0.01	0.00	0.01	0.02	0.02	0.00	-	0.01	0.01	0.01	0.01
FeO (tot)	9.91	0.17	9.92	0.10	11.63	0.15	11.87	0.23	11.64	0.17	13.00	0.16	12.78	0.23	12.53	0.16	12.62	0.22	12.36	0.25	12.36	0.11	14.20	0.30	14.32	-	14.85	0.26	14.79	0.26
MnO	0.16	0.03	0.14	0.02	0.19	0.03	0.16	0.03	0.17	0.04	0.17	0.01	0.17	0.03	0.19	0.01	0.18	0.04	0.21	0.05	0.17	0.02	0.20	0.03	0.23	-	0.20	0.03	0.19	0.03
MgO	49.72	0.21	49.49	0.21	48.63	0.39	47.87	0.24	48.43	0.26	47.66	0.16	47.64	0.24	47.71	0.19	47.70	0.14	47.49	0.30	47.19	0.26	46.62	0.39	46.71	-	46.19	0.27	46.13	0.33
CaO	0.02	0.01	0.02	0.02	0.02	0.01	0.02	0.01	0.02	0.01	0.02	0.00	0.02	0.01	0.02	0.01	0.01	0.01	0.01	0.01	0.01	0.01	0.01	0.01	0.01	-	0.02	0.01	0.01	0.01
Na_2O	0.01	0.01	0.01	0.01	0.01	0.01	0.00	0.01	0.01	0.01	0.01	0.01	0.01	0.01	0.01	0.01	0.00	0.01	0.01	0.02	0.01	0.01	0.00	0.00	0.02	-	0.01	0.01	0.01	0.01
K_2O	0.00	0.01	0.00	0.01	0.00	0.01	0.01	0.01	0.00	0.01	0.00	0.00	0.00	0.00	0.00	0.01	0.00	0.00	0.00	0.00	0.00	0.01	0.01	0.01	0.00	-	0.00	0.00	0.00	0.01
TiO_2	0.01	0.01	0.01	0.01	0.01	0.01	0.01	0.01	0.00	0.01	0.00	0.00	0.01	0.01	0.02	0.03	0.02	0.01	0.01	0.01	0.00	0.00	0.01	0.01	0.00	-	0.01	0.02	0.01	0.02
Cr_2O_3	0.01	0.01	0.01	0.01	0.01	0.01	0.00	0.01	0.01	0.01	0.00	0.00	0.00	0.01	0.00	0.00	0.02	0.02	0.02	0.02	0.02	0.02	0.02	0.02	0.09	-	0.01	0.02	0.01	0.01
NiO	0.34	0.05	0.35	0.04	0.29	0.04	0.26	0.05	0.36	0.03	0.24	0.01	0.23	0.03	0.30	0.10	0.30	0.03	0.26	0.05	0.28	0.04	0.22	0.04	0.32	-	0.36	0.05	0.37	0.04
Total	100.7		101.0		101.6		100.6		101.2		101.5		101.4		101.3		101.3		101.0		100.5		101.8		101.6		101.7		101.7	
Fo (mol%)	89.9	0.15	89.9	0.11	88.2	0.15	87.8	0.23	88.1	0.16	86.8	0.19	86.9	0.22	87.2	0.12	87.0	0.25	87.3	0.24	87.2	0.11	85.4	0.32	85.3	-	84.7	0.23	84.7	0.25

Table 2. Chemical compositions of olivine from selected samples. Fo = molar proportion of forsterite component [100 × $Mg/(Mg+Fe^{2+}_{tot})$, in atoms per formula unit].

Sample	BI4/1		BI10/3		BI10		BI5/1		BI2/5 (poikilitic inner zone)		BI2/5 (poikilitic rim)		BI2/1 (poikilitic inner zone)		BI2/1 (poikilitic rim)		BI2/7		BI6/2		BI30/5 (poikilitic)		BI30/5		BI2/5		BI10/3		BI2/5		BI10/3		BI2/5		BI10/3		BI8/1		BI50/3 (sub-prismatic)		BI50/3 (granoblastic)	
Rock type	Dunite		Dunite		Dunite		Dunite		Harzburgite		Harzburgite		Harzburgite		Harzburgite		Harzburgite		Lherzolite		Lherzolite		Lherzolite		Orthopyroxenite		Orthopyroxenite		Websterite		Websterite		Gabbronorite dyke		Gabbronorite dyke		Gabbronorite dyke		Gabbronorite dyke		Gabbronorite dyke	
No.	6	SD	3	SD	11	SD	11	SD	5	SD	4	SD	8	SD	6	SD	8	SD	14	SD	15	SD	14	SD	6	SD	4	SD	4	SD	3	SD	1	SD	5	SD	8	SD	4	SD	3	SD
SiO_2	56.62	0.34	55.83	0.25	55.54	0.27	55.49	0.26	55.32	0.30	55.22	0.21	55.37	0.26	55.45	0.41	55.90	0.22	55.31	0.25	54.68	0.31	54.84	0.61	54.67	0.23	55.42	0.23	54.39	0.32	54.84	0.21	54.62		53.48	0.46	52.58	0.40	52.18	0.25	52.59	0.37
Al_2O_3	2.64	0.18	2.78	0.17	2.62	0.17	2.75	0.18	2.84	0.12	2.92	0.26	2.83	0.16	2.80	0.30	2.47	0.18	3.46	0.16	3.29	0.23	3.28	0.28	3.81	0.44	3.77	0.43	4.38	0.50	4.49	0.46	4.87		5.07	0.22	4.17	0.45	5.00	0.41	4.35	0.41
FeO (tot)	6.97	0.12	8.36	0.05	8.37	0.22	7.96	0.29	8.84	0.15	8.83	0.09	8.51	0.17	8.49	0.08	8.33	0.10	9.77	0.23	10.18	0.17	10.25	0.18	8.91	0.10	8.32	0.18	9.01	0.16	8.72	0.27	9.36		12.46	0.50	17.00	0.31	17.75	0.99	17.85	0.31
MnO	0.16	0.03	0.22	0.02	0.19	0.03	0.21	0.04	0.20	0.03	0.21	0.03	0.19	0.03	0.18	0.04	0.18	0.04	0.20	0.03	0.20	0.03	0.21	0.03	0.21	0.02	0.18	0.04	0.18	0.04	0.16	0.03	0.24		0.26	0.05	0.39	0.03	0.36	0.05	0.38	0.04
MgO	33.74	0.18	32.82	0.20	32.71	0.22	33.02	0.36	32.48	0.16	32.65	0.20	32.66	0.25	32.61	0.29	32.60	0.38	31.57	0.37	31.61	0.29	31.50	0.39	32.06	0.38	32.46	0.30	32.15	0.38	32.19	0.18	31.13		28.93	0.52	25.89	0.26	25.55	0.52	25.91	0.21
CaO	0.25	0.03	0.38	0.04	0.30	0.10	0.30	0.10	0.25	0.05	0.26	0.08	0.27	0.04	0.37	0.17	0.29	0.06	0.33	0.07	0.31	0.18	0.34	0.29	0.47	0.03	0.47	0.11	0.30	0.10	0.32	0.02	0.44		0.49	0.25	0.42	0.11	0.31	0.05	0.31	0.01
Na_2O	0.02	0.02	0.00	0.00	0.01	0.01	0.01	0.01	0.01	0.01	0.01	0.01	0.01	0.01	0.01	0.01	0.00	0.00	0.01	0.01	0.01	0.01	0.02	0.01	0.01	0.01	0.02	0.01	0.01	0.01	0.01	0.01	0.02		0.01	0.01	0.02	0.02	0.01	0.01	0.03	0.02
K_2O	0.01	0.01	0.02	0.02	0.00	0.01	0.01	0.01	0.01	0.01	0.01	0.01	0.00	0.00	0.00	0.01	0.00	0.00	0.00	0.01	0.01	0.01	0.01	0.01	0.01	0.01	0.01	0.01	0.00	0.00	0.00	0.00	0.01		0.01	0.01	0.00	0.00	0.00	0.01	0.01	0.01
TiO_2	0.12	0.02	0.13	0.01	0.13	0.03	0.13	0.03	0.08	0.02	0.12	0.02	0.15	0.04	0.14	0.02	0.11	0.04	0.13	0.03	0.13	0.03	0.13	0.03	0.10	0.04	0.14	0.06	0.06	0.04	0.07	0.05	0.12		0.09	0.02	0.12	0.03	0.08	0.01	0.10	0.01
Cr_2O_3	0.36	0.03	0.30	0.05	0.30	0.05	0.33	0.05	0.26	0.04	0.26	0.07	0.33	0.04	0.31	0.06	0.28	0.05	0.24	0.03	0.24	0.06	0.22	0.05	0.17	0.02	0.22	0.04	0.06	0.07	0.04	0.03	0.01		0.08	0.02	0.03	0.03	0.02	0.03	0.01	0.02
NiO	0.05	0.04	0.05	0.02	0.07	0.03	0.06	0.04	0.05	0.04	0.04	0.05	0.08	0.03	0.06	0.05	0.05	0.04	0.04	0.03	0.06	0.04	0.06	0.03	0.06	0.04	0.05	0.03	0.02	0.03	0.06	0.00	0.00		0.03	0.03	0.02	0.02	0.05	0.06	0.01	0.02
Total	100.9		100.9		100.3		100.3		100.3		100.5		100.4		100.4		100.2		101.1		100.7		100.9		100.5		101.0		100.5		100.9		100.8		100.9		100.6		101.3		101.5	
Mg#	89.6	0.14	87.5	0.10	87.4	0.26	88.1	0.37	86.8	0.21	86.8	0.16	87.2	0.28	87.3	0.17	87.5	0.13	85.20	0.37	84.70	0.22	84.57	0.25	86.5	0.24	87.4	0.31	86.4	0.31	86.8	0.41	85.6		80.5	0.82	73.1	0.50	72.0	1.52	72.1	0.50
Cr#	8.5	0.57	6.9	1.25	7.1	0.88	7.3	0.84	5.9	0.90	5.5	1.23	7.2	0.78	6.9	0.82	7.1	1.07	4.43	0.40	4.61	1.05	4.28	0.93	3.0	0.42	3.9	0.94	1.0	1.11	0.6	0.43	0.1		1.1	0.22	0.4	0.43	0.3	0.37	0.2	0.34

Table 3. Chemical compositions of orthopyroxene from selected samples. Mg# is [100 × Mg/(Mg+Fe^{2+}_{tot}), in atoms per formula unit], and Cr# is [100 × Cr/(Cr+Al), in atoms per formula unit].

Sample	BI4/3		BI4/1		BI10/3		BI10/1		BI5/1		BI2/5		BI2/1		BI2/7		BI6/2 (poikilitic)		BI6/2		BI30/5		BI2/5		BI10/3		BI2/5		BI10/3 (sub-prismatic)		BI10/3 (granoblastic)		BI8/1		BI50/3 (sub-prismatic)		BI50/3 (granoblastic)	
Rock type	Dunite		Dunite		Dunite		Dunite		Dunite		Harzburgite		Harzburgite		Harzburgite		Lherzolite		Lherzolite		Lherzolite		Websterite		Websterite		Gabbronorite dyke		Gabbronorite dyke		Gabbronorite dyke		Gabbronorite dyke		Gabbronorite dyke		Gabbronorite dyke	
No.	7	SD	7	SD	4	SD	5	SD	17	SD	4	SD	12	SD	7	SD	5	SD	9	SD	10	SD	4	SD	4	SD	3	SD	4	SD	3	SD	8	SD	7	SD	3	SD
SiO_2	51.99	0.70	52.79	0.38	52.35	0.23	51.51	0.27	52.17	0.44	51.89	0.49	51.94	0.46	52.49	0.32	52.28	0.51	52.07	0.46	51.49	0.57	51.70	0.67	50.95	0.42	50.86	0.48	50.11	0.31	49.98	0.38	49.89	0.31	49.91	0.32	49.54	0.25
Al_2O_3	3.60	0.43	3.79	0.24	3.60	0.16	3.84	0.11	3.83	0.20	4.16	0.23	4.02	0.35	3.52	0.28	4.24	0.23	4.55	0.28	4.57	0.56	4.14	0.54	5.59	0.65	6.63	0.33	6.76	0.35	6.97	0.53	6.21	0.28	6.73	0.23	6.96	0.17
FeO (tot)	2.33	0.15	2.62	0.16	2.61	0.16	2.92	0.35	2.67	0.22	3.46	0.30	3.12	0.31	3.10	0.28	3.52	0.09	3.64	0.17	3.92	0.28	3.15	0.14	3.01	0.49	3.78	0.12	4.94	0.25	4.71	0.20	6.82	0.22	7.13	0.21	8.02	2.11
MnO	0.08	0.04	0.09	0.04	0.08	0.03	0.08	0.03	0.08	0.02	0.10	0.02	0.10	0.02	0.08	0.02	0.12	0.03	0.11	0.02	0.11	0.03	0.09	0.04	0.11	0.06	0.14	0.01	0.12	0.03	0.13	0.02	0.18	0.03	0.16	0.01	0.19	0.07
MgO	16.27	0.29	16.00	0.17	16.21	0.28	15.84	0.22	16.05	0.37	15.71	0.06	15.62	0.25	15.62	0.23	15.39	0.21	15.23	0.18	15.06	0.51	15.77	0.50	15.27	0.34	14.46	0.47	14.03	0.05	13.82	0.59	13.02	0.28	12.68	0.22	13.54	1.40
CaO	23.71	0.32	23.26	0.44	23.79	0.63	23.72	0.31	23.40	0.50	23.23	0.56	23.34	0.49	23.50	0.44	23.40	0.05	23.31	0.24	23.43	0.57	23.91	0.41	23.92	0.45	23.23	0.15	22.72	0.35	23.06	0.08	22.36	0.32	22.89	0.17	20.64	3.13
Na_2O	0.45	0.12	0.50	0.04	0.37	0.07	0.33	0.07	0.51	0.08	0.53	0.10	0.61	0.09	0.58	0.08	0.68	0.04	0.62	0.05	0.55	0.14	0.43	0.05	0.38	0.11	0.70	0.04	0.60	0.06	0.56	0.05	0.80	0.05	0.74	0.06	0.90	0.07
K_2O	0.01	0.01	0.01	0.01	0.01	0.01	0.00	0.00	0.01	0.01	0.01	0.01	0.01	0.01	0.00	0.01	0.00	0.00	0.01	0.01	0.00	0.01	0.00	0.00	0.01	0.01	0.00	0.00	0.01	0.01	0.01	0.00	0.00	0.00	0.00	0.01	0.01	0.01
TiO_2	0.50	0.04	0.54	0.05	0.59	0.05	0.60	0.05	0.58	0.06	0.51	0.04	0.72	0.11	0.58	0.06	0.67	0.07	0.64	0.05	0.79	0.12	0.42	0.03	0.62	0.05	0.56	0.09	0.63	0.04	0.63	0.08	0.76	0.06	0.81	0.03	0.81	0.09
Cr_2O_3	0.77	0.12	0.72	0.05	0.63	0.09	0.68	0.05	0.66	0.06	0.63	0.05	0.67	0.13	0.72	0.07	0.45	0.05	0.46	0.05	0.41	0.09	0.08	0.13	0.08	0.04	0.04	0.03	0.15	0.04	0.13	0.02	0.03	0.03	0.01	0.03	0.02	0.03
NiO	0.04	0.05	0.04	0.04	0.01	0.01	0.04	0.04	0.03	0.04	0.05	0.03	0.03	0.03	0.04	0.04	0.06	0.02	0.03	0.02	0.03	0.02	0.02	0.02	0.04	0.03	0.01	0.02	0.04	0.05	0.03	0.03	0.02	0.02	0.01	0.02	0.01	0.02
Total	99.8		100.4		100.2		99.6		100.0		100.3		100.2		100.2		100.8		100.7		100.4		99.7		100.0		100.4		100. 1		100.0		100.1		101.1		100.6	
Mg#	92.6	0.54	91.6	0.48	91.7	0.43	90.6	0.98	91.5	0.69	89.0	0.87	89.9	0.95	90.0	0.89	88.6	0.29	88.2	0.42	87.2	1.08	89.9	0.46	90.0	1.64	87.2	0.70	83.5	0.64	83.9	1.13	77.3	0.68	76.0	0.77	75.3	2.80
Cr#	12.6	1.22	11.3	0.43	10.6	1.18	10.6	0.48	10.4	0.70	9.2	0.81	10.1	1.70	12.0	0.76	6.7	0.86	6.3	0.55	5.7	0.64	1.5	2.54	1.0	0.44	0.4	0.27	1.5	0.43	1.3	0.14	0.4	0.31	0.1	0.31	0.2	0.30

Table 4. Chemical compositions of clinopyroxene from selected samples. The analyses refer to inner regions of grains. Mg# is [100 × Mg/(Mg+Fe^{2+}_{tot}), in atoms per formula unit], and Cr# is [100 × Cr/(Cr+Al), in atoms per formula unit].

Sample	BI4/3		BI4/1		BI10/1		BI5/1		BI2/1		BI2/7		BI6/2		BI30/5		BI2/5		BI10/3		BI2/5		BI10/3		BI8/1		BI50/3	
Rock type	**Dunite**		**Dunite**		**Dunite**		**Dunite**		**Harzburgite**		**Harzburgite**		**Lherzolite**		**Lherzolite**		**Websterite**		**Websterite**		**Gabbronorite dyke**		**Gabbronorite dyke**		**Gabbronorite dyke**		**Gabbronorite dyke**	
Amphibole classification	Prg		Ti-Prg		Prg		Prg		Ti-Prg		Ti-Prg		Ti-Prg		Ti-Prg		Prg		Prg		Prg		Prg		Ti-Prg		Ti-Prg	
No.	5	SD	7	SD	10	SD	19	SD	13	SD	5	SD	13	SD	14	SD	4	SD	2	SD	4	SD	8	SD	7	SD	6	SD
SiO_2	42.62	0.22	43.51	0.24	43.12	0.14	43.41	0.53	42.64	0.47	42.75	0.23	43.00	0.53	42.59	0.62	42.75	0.25	42.81	0.49	42.79	0.39	42.30	0.30	41.41	0.30	41.38	0.39
Al_2O_3	13.37	0.16	13.58	0.06	13.26	0.12	13.43	0.37	13.73	0.46	13.00	0.25	14.29	0.18	14.09	0.39	15.96	0.19	15.60	0.12	15.51	0.36	15.72	0.26	14.65	0.17	15.02	0.29
FeO (tot)	4.20	0.12	4.26	0.08	5.11	0.10	4.77	0.14	5.19	0.18	5.16	0.19	5.92	0.25	6.36	0.31	5.13	0.13	5.23	0.00	5.60	0.26	7.71	0.56	10.08	0.42	10.91	0.36
MnO	0.05	0.02	0.05	0.03	0.06	0.03	0.07	0.03	0.05	0.03	0.04	0.03	0.07	0.02	0.07	0.03	0.07	0.04	0.04	0.03	0.06	0.04	0.08	0.04	0.10	0.03	0.10	0.03
MgO	17.59	0.19	17.12	0.09	17.08	0.14	17.20	0.29	16.56	0.51	16.64	0.16	16.19	0.19	16.17	0.33	16.72	0.11	16.43	0.02	16.51	0.18	15.12	0.36	13.36	0.17	13.10	0.31
CaO	12.24	0.06	12.19	0.13	12.31	0.08	12.33	0.12	12.12	0.18	12.30	0.04	12.16	0.13	12.08	0.34	12.16	0.10	12.22	0.02	12.17	0.06	11.99	0.11	11.91	0.07	11.76	0.09
Na_2O	3.07	0.12	2.88	0.03	2.80	0.08	2.99	0.11	3.24	0.19	3.20	0.11	3.04	0.19	3.19	0.11	3.16	0.05	2.78	0.06	3.09	0.11	2.91	0.05	2.92	0.09	3.08	0.18
K_2O	0.22	0.03	0.28	0.02	0.17	0.02	0.23	0.04	0.26	0.21	0.31	0.08	0.12	0.04	0.10	0.05	0.25	0.01	0.16	0.03	0.26	0.01	0.15	0.02	0.56	0.07	0.46	0.03
TiO_2	2.12	0.19	2.52	0.12	1.83	0.10	2.08	0.20	2.94	0.11	2.65	0.08	2.76	0.21	2.66	0.28	1.52	0.10	1.77	0.07	1.70	0.11	1.69	0.12	2.87	0.12	2.72	0.15
Cr_2O_3	1.28	0.04	1.30	0.06	1.02	0.05	1.23	0.14	1.20	0.14	1.24	0.15	0.68	0.08	0.69	0.08	0.03	0.02	0.16	0.01	0.03	0.04	0.14	0.05	0.07	0.04	0.05	0.06
NiO	0.12	0.02	0.10	0.03	0.07	0.05	0.10	0.04	0.07	0.05	0.07	0.03	0.04	0.04	0.11	0.04	0.07	0.02	0.07	0.01	0.06	0.02	0.06	0.02	0.04	0.02	0.03	0.02
Total	96.9		97.8		96.8		97.8		98.0		97.4		98.3		98.1		97.8		97.2		97.8		97.9		98.0		98.6	
Mg#	88.2	0.33	87.8	0.18	85.6	0.28	86.5	0.32	85.0	0.64	85.2	0.35	83.0	0.62	81.9	0.57	85.3	0.39	85.3	0.56	84.0	0.76	77.7	1.65	70.2	1.08	68.1	1.15
Cr#	6.1	0.22	6.1	0.28	4.9	0.20	5.8	0.61	5.5	0.55	6.0	0.64	3.1	0.36	3.2	0.32	0.1	0.10	0.7	0.05	0.1	0.19	0.6	0.23	0.3	0.16	0.2	0.28

Table 5. Chemical compositions of amphibole from selected samples. Amphibole nomenclature is after Leake et al. (1997), and abbreviations are after Whitney and Evans (2010). Mg# is [100 × Mg/(Mg+Fe^{2+}_{tot}), in atoms per formula unit], and Cr# is [100 × Cr/(Cr+Al), in atoms per formula unit].

Sample	BI4/3		BI4/1		BI10/3		BI10/1		BI5/1		BI2/5 (in poikilitic Opx)		BI2/1		BI2/1 (in poikilitic Opx)		BI2/7		BI2/7 (in poikilitic Opx)		BI6/2		BI30/5		BI2/5		BI10/3		BI2/5		BI10/3		BI50/3	
Rock type	Dunite		Dunite		Dunite		Dunite		Dunite		Harzburgite		Harzburgite		Harzburgite		Harzburgite		Harzburgite		Lherzolite		Lherzolite		Orthopyroxenite		Orthopyroxenite		Websterite		Websterite		Gabbronorite dyke	
No.	6	SD	7	SD	3	SD	7	SD	7	SD	6	SD	10	SD	6	SD	3	SD	12	SD	4	SD	7	SD	4	SD	5	SD	6	SD	7	SD	3	SD
SiO_2	0.03	0.04	0.01	0.01	0.02	0.01	0.02	0.02	0.02	0.01	0.02	0.02	0.03	0.03	0.05	0.07	0.03	0.01	0.13	0.08	0.02	0.01	0.03	0.02	0.04	0.02	0.03	0.00	0.03	0.02	0.02	0.01	0.02	0.01
Al_2O_3	42.02	0.52	42.94	0.28	46.72	0.86	41.89	1.24	42.28	0.70	49.45	1.79	44.65	0.54	42.93	2.68	36.47	1.46	38.86	1.14	54.63	0.53	51.07	1.00	60.67	3.58	59.76	0.81	66.44	1.66	65.66	1.44	65.17	1.73
FeO (tot)	20.58	0.73	20.68	0.40	21.16	0.22	24.91	1.65	22.69	0.57	22.68	1.05	24.36	0.59	23.49	1.27	28.53	1.36	26.06	1.44	21.19	0.74	24.24	0.93	17.01	1.38	15.38	0.56	14.25	0.93	13.67	0.80	21.83	3.56
MnO	0.14	0.05	0.10	0.04	0.17	0.05	0.17	0.04	0.15	0.03	0.12	0.02	0.14	0.02	0.17	0.04	0.19	0.02	0.16	0.03	0.11	0.03	0.12	0.04	0.11	0.05	0.12	0.02	0.08	0.03	0.09	0.03	0.23	0.02
MgO	15.18	0.40	14.67	0.31	15.22	0.30	13.24	0.95	14.00	0.38	14.55	0.61	13.49	0.31	13.59	0.40	11.05	0.91	11.77	1.00	15.59	0.19	14.53	0.46	17.93	0.82	18.72	0.26	19.49	0.49	19.58	0.34	14.78	1.83
CaO	0.01	0.01	0.00	0.01	0.02	0.01	0.02	0.02	0.01	0.01	0.01	0.01	0.01	0.01	0.01	0.01	0.01	0.01	0.02	0.04	0.01	0.01	0.01	0.01	0.00	0.00	0.02	0.01	0.01	0.01	0.04	0.01	0.02	0.01
Na_2O	0.02	0.02	0.01	0.01	0.02	0.02	0.02	0.03	0.02	0.03	0.03	0.02	0.01	0.02	0.02	0.03	0.01	0.01	0.02	0.02	0.01	0.01	0.01	0.01	0.00	0.00	0.01	0.01	0.02	0.01	0.01	0.01	0.02	0.03
K_2O	0.00	0.00	0.01	0.01	0.00	0.00	0.00	0.01	0.00	0.00	0.00	0.00	0.00	0.01	0.01	0.01	0.00	0.00	0.00	0.00	0.00	0.00	0.00	0.01	0.00	0.00	0.00	0.00	0.00	0.00	0.00	0.01	0.00	0.00
TiO_2	0.13	0.03	0.15	0.04	0.05	0.02	0.17	0.02	0.16	0.03	0.08	0.04	0.11	0.05	0.16	0.05	0.06	0.03	0.18	0.06	0.04	0.03	0.03	0.02	0.03	0.02	0.07	0.09	0.01	0.01	0.04	0.01	0.03	0.01
Cr_2O_3	23.85	0.46	22.92	0.35	17.47	1.38	20.25	0.44	22.23	0.62	14.46	1.05	19.20	0.48	21.48	2.56	24.40	0.49	22.95	1.08	10.50	0.33	11.48	0.66	5.87	2.76	6.88	0.22	1.07	1.46	1.29	0.82	0.30	0.06
NiO	0.21	0.04	0.20	0.03	0.25	0.05	0.21	0.05	0.25	0.04	0.23	0.02	0.19	0.04	0.19	0.03	0.10	0.07	0.17	0.05	0.19	0.04	0.39	0.05	0.26	0.06	0.34	0.07	0.27	0.06	0.33	0.03	0.14	0.05
Total	102.2		101.7		101.1		100.9		101.8		101.6		102.2		102.1		100.8		100.3		102.3		101.9		101.9		101.3		101.7		100.8		102.5	
Mg#	56.8	1.43	55.8	0.91	56.2	0.67	48.6	3.43	52.4	1.28	53.3	2.19	49.7	1.12	50.8	1.97	40.8	3.09	44.6	3.44	56.7	1.16	51.7	1.63	65.3	2.85	68.4	1.09	70.9	1.82	71.8	1.51	54.7	7.03
Cr#	27.6	0.43	26.4	0.32	20.0	1.56	24.5	0.80	26.1	0.83	16.4	1.50	22.4	0.42	25.2	3.38	31.0	1.27	28.4	1.43	11.4	0.35	13.1	0.87	6.2	3.09	7.2	0.30	1.1	1.48	1.3	0.85	0.3	0.06

Table 6. Chemical compositions of spinel from selected samples. Mg# is [100 × Mg/(Mg+Fe^{2+}_{tot}), in atoms per formula unit], and Cr# is [100 × Cr/(Cr+Al), in atoms per formula unit].

5.1.4 Oxygen isotopic composition of olivine

The ion microprobe analyses of olivine revealed limited $\delta^{18}O$ variations within a single peridotite (Table 8). Olivine $\delta^{18}O$ gradually increases with decreasing forsterite proportion (Fig. 10). In particular, the most primitive dunite and the most evolved lherzolite show $\delta^{18}O_{Ol}$ of +5.77 ± 0.10 ‰ (weighted average ± 2σ, n = 18) and +6.57 ± 0.06 ‰ (weighted average ± 2σ, n = 20), respectively. Taken as a whole, the Rocca d'Argimonia olivines have slightly higher $\delta^{18}O$ than typical mantle olivines (5.2 ± 0.3 ‰, Mattey et al., 1994).

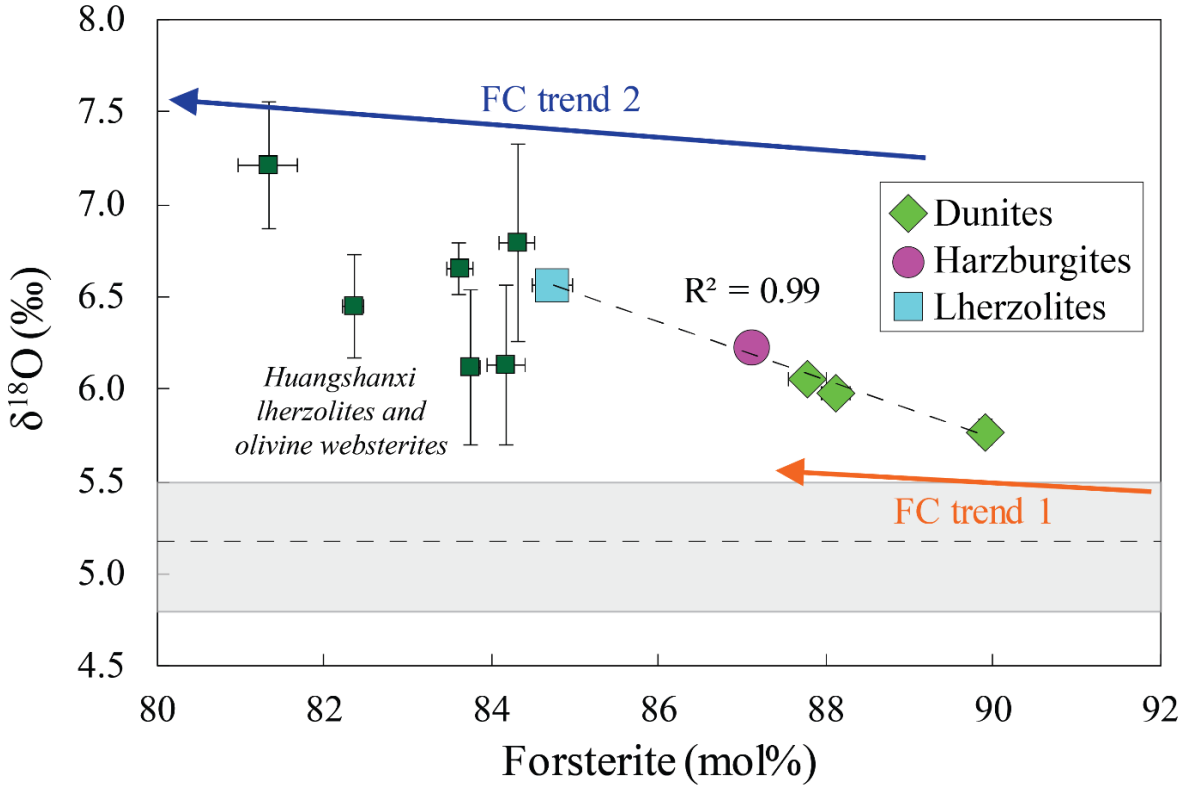

Figure 10. $\delta^{18}O$ (weighted average ± 2σ) versus forsterite proportion (mean ± 2σ) of olivine from the Rocca d'Argimonia peridotites; the error bars are in most cases within the symbol area. The compositions of olivine from lherzolites and olivine websterites of the Huangshanxi mafic-ultramafic intrusion in northwestern China (Mao et al., 2019) are reported for comparative purposes. The grey field represents the $\delta^{18}O$ of typical mantle olivines (Mattey et al., 1994). The diagram also reports the $\delta^{18}O$ variations modelled by Bucholz et al. (2017) in response to closed system fractional crystallization for (i) an anhydrous tholeiite crystallizing at 1.0 GPa (FC trend 1) and (ii) a high-K basalt with 2.5 H_2O crystallizing at ~0.4 GPa (FC trend 2). The anhydrous tholeiite model is based on the experimental results of Villiger et al. (2004); a typical mantle $\delta^{18}O$ value of +5.7 ‰ is assumed for the parental melt. Both models show that the $\delta^{18}O_{Ol}$ variations observed for the Rocca d'Argimonia peridotites are wider than those dictated by fractional crystallization alone.

5.2 Gabbronorite dykes and peridotite contact zones

5.2.1 Petrographic characteristics

The gabbronorites mostly consist of plagioclase, clinopyroxene and orthopyroxene (Table 9) and display mediumgrained, granoblastic to nearly granoblastic structure (Fig. 5c). These rocks locally also include sub-prismatic grains of orthopyroxene and clinopyroxene, which in places enclose euhedral to subhedral plagioclase grains. The gabbronorites also show 6 vol%–14 vol% amphibole with nearly equant morphology and are classified as hornblende gabbronorites (Fig. 4b). Al spinel (Table 6) and Fe–Cu sulfides (pyrrhotite and minor chalcopyrite) are common accessories.

The contact zone between gabbronorites and host peridotites was investigated for the thinnest selected dykes (samples BI2/5 and BI10/3, Table 10). In both cases, the contact zone consists of two different orthopyroxene-rich microlayers, each ~2 mm thick (Fig. 5c). Towards the peridotite side, there is a spinel-bearing orthopyroxenite with a nearly granoblastic structure defined by equant, polygonal morphology of orthopyroxene. This orthopyroxenite micro-layer includes 6 vol%–9 vol% spinel, which is typically anhedral and interstitial with respect to orthopyroxene. The microlayer adjacent to the gabbronorite is made up of orthopyroxene, amphibole, clinopyroxene and spinel, and it is therefore classified as hornblende websterite (Fig. 4). Pyroxenes and amphibole in the websterite micro-layer define a nearly granoblastic structure, whereas associated spinel has vermicular morphology. Accessory pyrrhotite occurs in both the orthopyroxenite and the hornblende websterite micro-layers.

5.2.2 Whole-rock chemical compositions

The thin dykes BI2/5 and BI10/3 have higher Mg# than the thick dykes BI8/1 and BI50/3 (82–84 and 74–75, respectively). Taken as a whole, the gabbronorites have high Al_2O_3 and CaO contents (Fig. 6), which are mostly controlled by the high modal proportions of plagioclase and clinopyroxene, respectively. In particular, the gabbronorite BI10/3 has the lowest Al_2O_3 and the highest CaO reflecting its low plagioclase/clinopyroxene modal ratio (cf. Tables 1 and 9).

5.2.3 Mineral chemical compositions

The minerals constituting the gabbronorite dykes are compositionally homogeneous within a single sample. Taken as a whole, however, clinopyroxene, orthopyroxene and amphibole (pargasite to titanian pargasite) from the gabbronorites show wide Mg# variations (Fig. 8, Tables 3, 4 and 5) paralleling the whole-rock variations. Cr_2O_3 in mafic silicates from the gabbronorites is invariably negligible (≤0.1 wt%). Orthopyroxene contains 0.3 wt%–0.5 wt% CaO, and clinopyroxene displays 0.6 wt%–0.8 wt% Na_2O and 0.6 wt%–0.8 wt% TiO_2. Plagioclase from the gabbronorites has anorthite proportion ranging from 88 mol% to 75 mol% (Table 7).

In the gabbronorite–peridotite contact zone, orthopyroxene has 87–86 Mg#, with no significant variability between the websterite and the orthopyroxenite micro-layer (Fig. 8). Conversely, orthopyroxene shows a Cr_2O_3 decrease and a concomitant Al_2O_3 increase (i.e. a Cr# decrease) from the orthopyroxenite to the websterite micro-layer, which is paralleled by associated spinel (Fig. 11). Clinopyroxene and amphibole (pargasite) present in the websterite micro-layer exhibit high Mg# of 90 and 85, respectively.

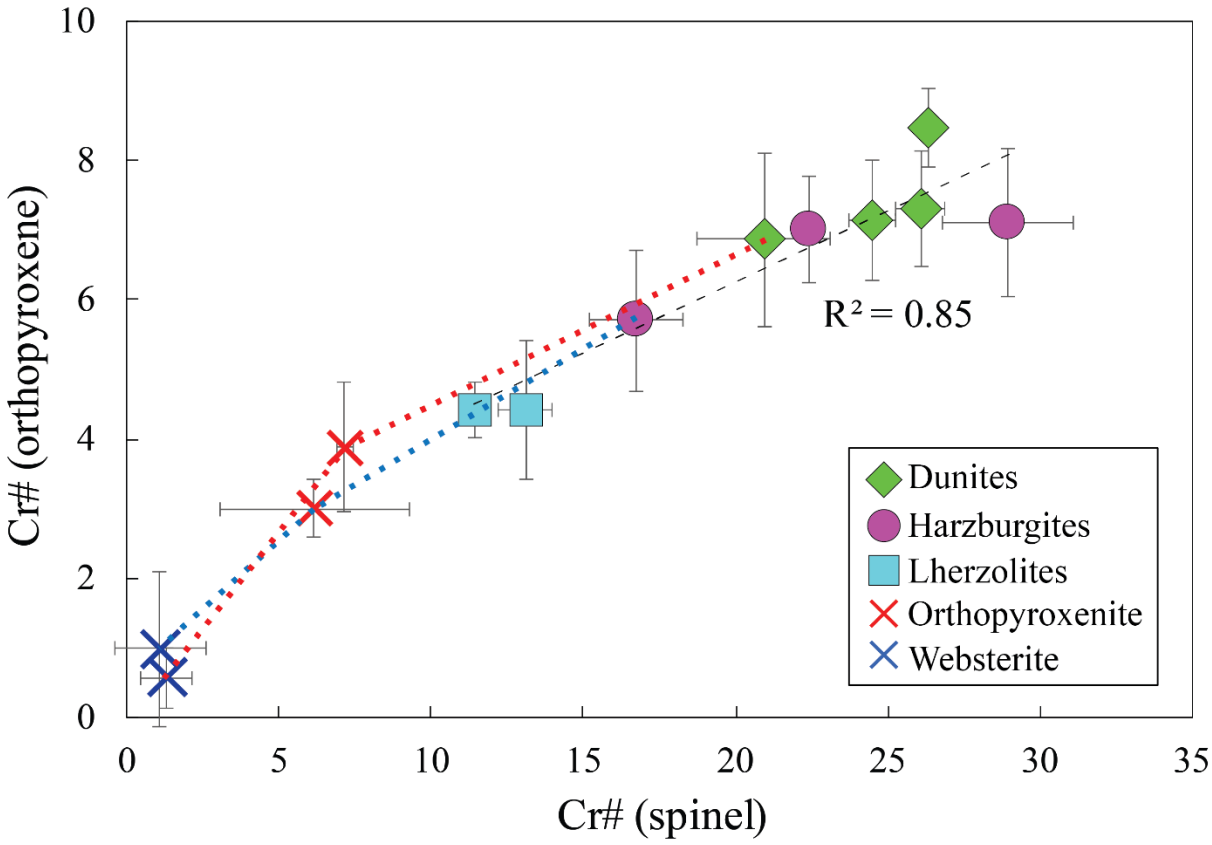

Figure 11. Plot of Cr# [100×Cr/(Cr+Al), mol%] of orthopyroxene versus Cr# of coexisting spinel (mol%) for the Rocca d'Argimonia peridotites. Data are averaged per sample; error bars represent the standard deviation of the mean value (2σ). The diagram also reports the compositions of orthopyroxene–spinel pairs from the contact zone at the boundaries between the thin gabbronorite BI2/5 and BI10/3 dykes and host peridotites. The dotted tie lines refer to these contact zones and physically adjacent peridotites (blue: sample BI2/5; red: sample BI10/3).

Sample	BI2/5		BI10/3		BI8/1		BI50/3 (included in Px)		BI50/3 (granoblastic)	
Rock type	**Gabbronorite dyke**		**Gabbronorite dyke**		**Gabbronorite dyke**		**Gabbronorite dyke**		**Gabbronorite dyke**	
No.	9	SD	6	SD	8	SD	5	SD	5	SD
SiO_2	47.47	0.31	46.00	0.31	49.36	0.27	48.85	0.60	49.52	0.12
Al_2O_3	33.55	0.48	34.46	0.11	32.32	0.27	33.62	0.30	33.04	0.31
FeO (tot)	0.04	0.03	0.09	0.03	0.07	0.06	0.24	0.08	0.11	0.02
MnO	0.01	0.01	0.01	0.02	0.01	0.02	0.00	0.00	0.01	0.02
MgO	0.01	0.01	0.00	0.01	0.00	0.01	0.00	0.01	0.01	0.00
CaO	16.58	0.33	17.82	0.28	15.52	0.14	16.17	0.53	15.54	0.12
Na_2O	2.08	0.20	1.35	0.13	2.90	0.13	2.59	0.30	2.88	0.13
K_2O	0.01	0.01	0.01	0.01	0.02	0.01	0.01	0.01	0.02	0.00
TiO_2	0.00	0.00	0.02	0.04	0.01	0.02	0.02	0.03	0.00	0.01
Cr_2O_3	0.02	0.02	0.02	0.03	0.01	0.01	0.03	0.03	0.03	0.03
NiO	0.01	0.02	0.00	0.00	0.02	0.02	0.02	0.03	0.03	0.05
Total	99.8		99.8		100.2		101.6		101.2	
An (mol%)	81.5	1.75	87.9	1.19	74.7	0.97	77.5	2.54	74.8	0.96

Table 7. Chemical compositions of plagioclase from selected samples. An = molar proportion of anorthite component [100 × Ca/(Ca+K+Na), in atoms per formula unit].

Sample	BI4/1																	
	BI4-1@1	BI4-1@2	BI4-1@3	BI4-1@4	BI4-1@5	BI4-1@6	BI4-1@7	BI4-1@8	BI4-1@9	BI4-1@10	BI4-1@11	BI4-1@12	BI4-1@13	BI4-1@14	BI4-1@15	BI4-1@16	BI4-1@17	BI4-1@18
IP(nA)	1.37	1.37	1.37	1.37	1.37	1.37	1.37	1.37	1.37	1.37	1.37	1.37	1.37	1.37	1.36	1.36	1.36	1.36
Intensity O^{16}	1.351E+9	1.357E+9	1.355E+9	1.355E+9	1.354E+9	1.350E+9	1.353E+9	1.359E+9	1.358E+9	1.362E+9	1.358E+9	1.358E+9	1.353E+9	1.349E+9	1.360E+9	1.358E+9	1.363E+9	1.367E+9
O^{16}/O^{18} Mean	2.040E-3	2.040E-3	2.040E-3	2.039E-3	2.040E-3	2.039E-3	2.039E-3	2.040E-3	2.040E-3	2.040E-3	2.040E-3	2.040E-3	2.039E-3	2.039E-3	2.040E-3	2.039E-3	2.039E-3	2.039E-3
delta O^{18}	5.86	5.82	5.77	5.60	6.06	5.60	5.71	5.82	6.05	6.07	6.02	5.96	5.71	5.50	5.79	5.65	5.28	5.65
2SE (error)	0.27	0.33	0.33	0.38	0.36	0.32	0.26	0.44	0.31	0.47	0.24	0.30	0.23	0.21	0.34	0.23	0.83	0.41
Weighted average (± 2σ) 5.771 ± 0.071																		

Sample	BI5/1																			
	BI5-1@1	BI5-1@2	BI5-1@3	BI5-1@4	BI5-1@5	BI5-1@6	BI5-1@7	BI5-1@8	BI5-1@9	BI5-1@10	BI5-1@11	BI5-1@12	BI5-1@13	BI5-1@14	BI5-1@15	BI5-1@16	BI5-1@17	BI5-1@18	BI5-1@19	BI5-1@20
IP(nA)	1.37	1.37	1.37	1.37	1.37	1.37	1.37	1.37	1.37	1.37	1.37	1.38	1.38	1.38	1.38	1.37	1.37	1.38	1.38	1.38
Intensity O^{16}	1.391E+9	1.404E+9	1.394E+9	1.388E+9	1.387E+9	1.390E+9	1.388E+9	1.390E+9	1.388E+9	1.385E+9	1.393E+9	1.391E+9	1.395E+9	1.380E+9	1.379E+9	1.385E+9	1.381E+9	1.377E+9	1.383E+9	1.376E+9
O^{16}/O^{18} Mean	2.041E-3	2.041E-3	2.041E-3	2.040E-3	2.041E-3	2.040E-3	2.041E-3	2.041E-3	2.041E-3	2.041E-3	2.041E-3	2.041E-3	2.040E-3	2.041E-3	2.041E-3	2.041E-3	2.041E-3	2.040E-3	2.040E-3	2.041E-3
delta O^{18}	6.10	6.33	6.05	5.73	5.87	5.82	5.90	5.89	5.95	6.09	6.16	6.34	5.81	6.07	6.01	6.02	6.08	5.77	5.83	6.23
2SE (error)	0.26	0.31	0.38	0.26	0.36	0.28	0.19	0.24	0.27	0.21	0.25	0.33	0.31	0.38	0.33	0.37	0.38	0.25	0.35	0.59
Weighted average (± 2σ)	5.98 ± 0.064																			

Sample	BI10/1																		
	BI10-1@1	BI10-1@2	BI10-1@3	BI10-1@4	BI10-1@5	BI10-1@6	BI10-1@7	BI10-1@8	BI10-1@9	BI10-1@10	BI10-1@11	BI10-1@12	BI10-1@13	BI10-1@14	BI10-1@15	BI10-1@16	BI10-1@17	BI10-1@18	BI10-1@19
IP(nA)	1.38	1.38	1.38	1.38	1.38	1.38	1.38	1.38	1.38	1.37	1.37	1.37	1.37	1.37	1.37	1.37	1.37	1.37	1.37
Intensity O^{16}	1.382E+9	1.384E+9	1.387E+9	1.386E+9	1.389E+9	1.390E+9	1.394E+9	1.398E+9	1.387E+9	1.397E+9	1.404E+9	1.408E+9	1.397E+9	1.397E+9	1.400E+9	1.399E+9	1.401E+9	1.404E+9	1.403E+9
O^{16}/O^{18} Mean	2.041E-3	2.041E-3	2.041E-3	2.041E-3	2.041E-3	2.041E-3	2.041E-3	2.041E-3	2.041E-3	2.040E-3	2.041E-3	2.040E-3	2.040E-3	2.040E-3	2.040E-3	2.041E-3	2.040E-3	2.041E-3	2.040E-3
delta O^{18}	5.91	6.17	6.30	6.19	6.13	6.23	6.19	6.05	6.15	5.87	6.02	5.83	5.87	5.83	5.82	6.15	5.77	6.18	5.83
2SE (error)	0.27	0.29	0.33	0.27	0.20	0.28	0.19	0.38	0.21	0.33	0.35	0.26	0.42	0.28	0.39	0.48	0.34	0.48	0.31
Weighted average (± 2σ)	6.051 ± 0.066																		

Sample	BI2/1																	
	BI2-1@1	BI2-1@2	BI2-1@3	BI2-1@4	BI2-1@5	BI2-1@6	BI2-1@7	BI2-1@8	BI2-1@9	BI2-1@10	BI2-1@11	BI2-1@12	BI2-1@13	BI2-1@14	BI2-1@15	BI2-1@16	BI2-1@17	BI2-1@18
IP(nA)	1.38	1.38	1.38	1.38	1.38	1.38	1.38	1.38	1.38	1.38	1.38	1.38	1.38	1.38	1.38	1.38	1.38	1.37
Intensity O^{16}	1.381E+9	1.378E+9	1.383E+9	1.396E+9	1.396E+9	1.391E+9	1.385E+9	1.394E+9	1.390E+9	1.399E+9	1.393E+9	1.389E+9	1.395E+9	1.393E+9	1.396E+9	1.403E+9	1.399E+9	1.394E+9
O^{16}/O^{18} Mean	2.041E-3	2.042E-3	2.041E-3	2.041E-3	2.041E-3	2.041E-3	2.041E-3	2.041E-3	2.041E-3	2.041E-3	2.041E-3	2.041E-3	2.042E-3	2.041E-3	2.042E-3	2.041E-3	2.041E-3	2.041E-3
delta O^{18}	6.21	6.66	6.19	6.35	6.19	6.29	6.16	6.01	6.22	6.20	6.40	6.29	6.44	6.31	6.57	6.18	6.04	5.96
2SE (error)	0.28	0.36	0.33	0.26	0.39	0.29	0.39	0.32	0.35	0.34	0.39	0.33	0.30	0.42	0.40	0.25	0.31	0.19
Weighted average (± 2σ)	6.222 ± 0.073																	

Sample	BI30/5																			
	BI30-5@1	BI30-5@2	BI30-5@3	BI30-5@4	BI30-5@5	BI30-5@6	BI30-5@7	BI30-5@8	BI30-5@9	BI30-5@10	BI30-5@11	BI30-5@12	BI30-5@13	BI30-5@14	BI30-5@15	BI30-5@16	BI30-5@17	BI30-5@18	BI30-5@19	BI30-5@20
IP(nA)	1.38	1.38	1.38	1.37	1.38	1.38	1.38	1.38	1.38	1.38	1.38	1.38	1.38	1.38	1.38	1.38	1.38	1.38	1.37	1.37
Intensity O^{16}	1.421E+9	1.427E+9	1.418E+9	1.425E+9	1.424E+9	1.411E+9	1.423E+9	1.425E+9	1.410E+9	1.414E+9	1.415E+9	1.417E+9	1.403E+9	1.410E+9	1.417E+9	1.419E+9	1.418E+9	1.411E+9	1.411E+9	1.418E+9
O^{16}/O^{18} Mean	2.042E-3	2.041E-3	2.041E-3	2.042E-3	2.042E-3	2.042E-3	2.042E-3	2.042E-3	2.042E-3	2.042E-3	2.042E-3	2.042E-3	2.042E-3	2.042E-3	2.042E-3	2.042E-3	2.042E-3	2.041E-3	2.042E-3	2.042E-3
delta O^{18}	6.85	6.28	6.35	6.76	6.57	6.51	6.59	6.53	6.77	6.51	6.67	6.53	6.45	6.54	6.67	6.81	6.43	6.27	6.58	6.69
2SE (error)	0.35	0.26	0.44	0.22	0.31	0.30	0.26	0.29	0.32	0.31	0.32	0.28	0.24	0.49	0.19	0.27	0.26	0.26	0.31	0.37
Weighted average (± 2σ)	6.568 ± 0.063																			

Sample	San Carlos Olivine																				
	Sancarlos1 @1	Sancarlos1 @2	Sancarlos1 @3	Sancarlos1 @4	Sancarlos1 @5	Sancarlos1 @6	Sancarlos1 @7	Sancarlos1 @8	Sancarlos1 @9	Sancarlos2 @1	Sancarlos2 @2	Sancarlos2 @3	Sancarlos2 @4	Sancarlos3 @1	Sancarlos3 @2	Sancarlos3 @3	Sancarlos3 @4	Sancarlos4 @1	Sancarlos4 @2	Sancarlos4 @3	Sancarlos4 @4
IP(nA)	1.37	1.38	1.38	1.38	1.37	1.37	1.37	1.37	1.37	1.37	1.37	1.38	1.38	1.38	1.38	1.38	1.37	1.37	1.37	1.37	1.36
Intensity O^{16}	1.376E+9	1.370E+9	1.372E+9	1.363E+9	1.372E+9	1.374E+9	1.369E+9	1.360E+9	1.375E+9	1.368E+9	1.357E+9	1.365E+9	1.367E+9	1.371E+9	1.362E+9	1.367E+9	1.361E+9	1.352E+9	1.347E+9	1.357E+9	1.350E+9
O^{16}/O^{18} Mean	2.039E-3	2.039E-3	2.040E-3	2.039E-3	2.039E-3	2.040E-3	2.039E-3	2.039E-3	2.039E-3	2.039E-3	2.040E-3	2.039E-3	2.039E-3	2.040E-3	2.039E-3	2.039E-3	2.040E-3	2.038E-3	2.039E-3	2.038E-3	2.038E-3
delta O^{18}	4.97	5.04	5.74	5.38	5.37	5.42	4.92	5.38	5.04	5.01	5.49	5.31	5.18	5.45	4.93	5.14	5.48	5.05	5.65	5.07	5.23
2SE (error)	0.33	0.18	0.33	0.39	0.32	0.39	0.51	0.30	0.35	0.37	0.29	0.46	0.34	0.28	0.24	0.32	0.33	0.33	0.18	0.35	0.28
Weighted average (± 95% conf.)	5.27 ± 0.12																				

Table 8. Oxygen isotope compositions of olivine from selected samples, and of San Carlos olivine standard.

Sample initials	Mineral modes (wt%)						Mineral modes (vol%)						Average grain size (mm)						Notes			Rock nomenclature	Coordinates	
	Ol	Opx	Cpx	Amp	Pl	Spl	Ol	Opx	Cpx	Amp	Pl	Spl	Ol	Opx	Cpx	Amp	Pl	Spl	Dyke width (cm)	Host rock	Other notes		x	y
Dunite BI4/3	92.1	0.6	3.3	1.2	-	2.8	92	1	3	1	-	2	3.0	0.3	0.7	0.5	-	0.6				Hornblende-bearing dunite	430064.0	5057698.8
DuniteBI4/1	92.1	0.6	3.4	1.1	-	2.8	92	1	4	1	-	2	2.5	1.0	1.0	0.6	-	0.7				Hornblende-bearing dunite	430059.0	5057692.9
Dunite BI10/3	88.5	5.3	2.5	1.2	-	2.5	89	5	3	1	-	2	3.0	1.0	1.0	up to 0.6	-	0.7				Hornblende-bearing dunite	429924.6	5057549.3
Dunite BI10/1	90.8	2.8	2.8	1.1	-	2.5	91	3	3	1	-	2	2.0	2.0	1.5	0.6	-	0.7				Hornblende-bearing dunite	429912.2	5057561.7
Dunite BI5/1	84.8	2.8	4.8	1.9	-	5.7	85	3	5	2	-	5	3.0	3.0	1.5	0.5	-	0.8			Large non-poikilitic Opx	Hornblende-bearing dunite	430205.7	5057811.1
Harzburgite BI2/1	83	7.2	4.2	1.5	-	4.1	83	7	4	2	-	3	1.5	9.0	1.0	0.6	-	0.6			Poikilitic Opx (up to 1 cm)	Hornblende-bearing harzburgite	429923.3	5057732.4
Harzburgite BI2/7	79.5	14.1	2.2	0.9	-	3.3	79	15	2	1	-	3	1.7	8.0	0.7	0.5	-	0.5			Poikilitic Opx (up to 1 cm)	Hornblende-bearing harzburgite	429861.8	5057726.5
Lherzolite BI6/2	54.3	27.2	13.8	1.7	-	3	54	28	14	2	-	3	1.0	1.5	2.0*	up to 0.6	-	0.6			Poikilitic Cpx (0.6 cm)	Hornblende-bearing lherzolite	429925.1	5057663.0
Lherzolite BI30/5	37.6	50.3	5.3	2.3	-	4.5	37	51	5	2	-	4	1.0	2.0*	1.5	0.6	-	0.7			Poikilitic Opx (up to 0.8 cm)	Hornblende-bearing olivine websterite	429768.9	5057796.4
Gabbronorite dyke BI2/5	-	17.8	14.8	15.1	51.3	1.0	-	16	13	14	56	1	-	1.0	1.0	1.0	2.0	0.3	2.5	Harzburgite		Hornblende gabbronorite	429902.3	5057750.2
Gabbronorite dyke BI10/3	-	22.8	47.8	9.3	19.3	0.8	-	22	46	9	22	1	-	5.0	5.0	1.0	2.0	0.5	3.0	Dunite		Hornblende gabbronorite	429924.6	5057549.3
Gabbronorite dyke BI8/1	-	23.9	21.6	7.0	47.5		-	21	20	7	53	-	-	1.0	1.0	1.0	1.5	-	10.0	Harzburgite	Sparse sub-prismatic Px, up to 3.5 mm long	Hornblende gabbronorite	429849.7	5057694.9
Gabbronorite dyke BI50/3	-	23.0	24.3	6.0	44.9	1.8	-	20	22	6	50	1	-	3.0	3.0	1.0	1.7	1.0	25.0	Harzburgite	Frequent sub-prismatic Px, up to 7 mm long	Hornblende gabbronorite	429431.9	5056741.6

* = poikilitic grains are not considered in the average grain size

Table 9. Location and main petrographic characteristics of selected samples. Mineral proportion calculations (wt%) were carried out on anhydrous basis, assuming all Fe as Fe^{2+}. We used a least squares mixing program to reproduce the observed whole-rock compositions (Table 1) based on mineral compositions (Tables 2 to 7). For the peridotites, the best fit between observed and calculated whole-rock compositions was obtained by refinements based on: (i) TiO_2, CaO and Na_2O for clinopyroxene and amphibole proportions, and (ii) SiO_2, Al_2O_3, NiO and Cr_2O_3 for olivine, orthopyroxene and spinel proportions. Obtained weight proportions were converted to volume proportions based on mineral densities (olivine = 3.3-3.4 g/cm^3, orthopyroxene = 3.3-3.4 g/cm^3, clinopyroxene = 3.2-3.3 g/cm^3, amphibole = 3.2 g/cm^3, spinel = 4.0-4.4 g/cm^3, plagioclase = 2.7 g/cm^3). Mineral abbreviations are after Whitney and Evans (2010), and rock nomenclature follows the classification of the International Union of Geological Sciences.

Sample initials	Average thickness (mm)	Mineral modes (vol%)				Average grain size (mm)				Rock nomenclature
		Opx	Cpx	Amp	Spl	Opx	Spl	Amp	Cpx	
BI2/5 towards peridotite	2.0	93.7	-	-	6.3	0.6	0.4	-	-	Orthopyroxenite
BI10/3 towards peridotite	1.9	91.4	-	-	8.6					Orthopyroxenite
BI2/5 towards gabbronorite	2.5	57.7	12.2	22	8.1	0.4	0.3	0.4	0.4	Hornblende websterite
BI10/3 towards gabbronorite	2.6	53.9	16.4	17.9	11.8					Hornblende websterite

Table 10. Main petrographic characteristics of micro-layers occurring along the contacts between gabbronorite dykes and host peridotites. Mineral proportions were evaluated by point counting. Mineral abbreviations are after Whitney and Evans (2010), and rock nomenclature follows the classification of the International Union of Geological Sciences.

6 Discussion

6.1 The Rocca d'Argimonia rock sequence: effects of subsolidus re-equilibration

The Rocca d'Argimonia ultramafic sequence shows alternating peridotite and pyroxenite layers that are tens of metres in thickness (Fig. 2; see also Lensch, 1968) and is locally crosscut by gabbronorite dykes. The Rocca d'Argimonia rocks, including the gabbronorite dykes, typically display both nearly granoblastic structure documenting re-equilibration by solid-state diffusion and/or recrystallization and relics of microstructures that may be reconciled with magmatic processes. The latter include the poikilitic morphology of orthopyroxene (Figs. 3a and 5a) in the harzburgites and the lherzolites and of clinopyroxene in the lherzolites (Fig. 5b). Evidence for a magmatic growth in the dunites is furnished by the orthopyroxene typically exhibiting anhedral habit, locally interstitial with respect to olivine, and by the euhedral to subhedral morphology of spinel grains enclosed by olivine. The gabbronorites retain magmatic structures at the macroscopic scale, as shown by the modal–grain size layering and the pyroxenes oriented orthogonally with respect to dyke walls, and at microscopic scale, with the local occurrence of sub-prismatic pyroxene grains hosting euhedral to subhedral plagioclase.

Application of the Ca-in-orthopyroxene and the orthopyroxene–clinopyroxene geothermometers of Brey and Kohler (1990) to the peridotites gave subsolidus estimates of 708–810°C (Table 11). We also employed the two-pyroxene geothermometer of Wells (1977), which does not require the presence of olivine and spinel in the confining mineral assemblage, obtaining 804–858°C for the peridotites and 810–838°C for the gabbronorites. The Wells' (1977) method yielded similar temperature values of 778–793°C for the websterite micro-layer occurring along the gabbronorite–peridotite contact. Overall, these temperature evaluations correspond to granulite facies metamorphic conditions and most likely reflect slow cooling of the Rocca d'Argimonia sequence in the lower continental crust. On the other hand, application of the amphibole–plagioclase geothermometer of Holland and Blundy (1994) to the gabbronorite dykes gave relatively high temperature values of 971–1035°C. For the gabbronorites, we obtained similar estimates of 999–1030°C based on the single amphibole geothermometer of Putirka (2016). Most likely, the amphibole-based geothermometers have a higher closure temperature than the pyroxene-based methods. The amphibole-based temperature evaluations could refer to late magmatic conditions, in agreement with the temperature range observed in fractional crystallization experiments from hydrous melts carried out at 0.7–0.9 GPa (e.g. Nekvasil et al., 2004).

The re-equilibration shown by the two-pyroxene geothermometry may have affected the original oxygen isotope mineral distribution through diffusive exchange (Giletti, 1986; Eiler et al., 1992, 1993; Valley, 2001). In particular, the slow cooling potentially produces a slight $\delta^{18}O$ olivine decrease

and a concomitant $\delta^{18}O$ increase of coexisting pyroxene (Chiba et al., 1989; Rosenbaum et al., 1994). If an olivine crystallized from a melt at 1300°C and subsequently completely re-equilibrated with pyroxene at 700°C, the $\delta^{18}O_{Ol}$ is expected to lower by 0.4 ‰. The primary $\delta^{18}O_{Ol}$ of the Rocca d'Argimonia peridotites could therefore be slightly higher than the observed value. It should be noted, however, that olivine is characterized by a low oxygen self-diffusivity (Dohmen et al., 2002). Actually, in mafic–ultramafic intrusions from middle and upper crustal levels, olivine is typically considered to retain the magmatic oxygen isotopic signature (e.g. Bucholz et al., 2017; Günther et al., 2018; Mao et al., 2019). Preservation of magmatic $\delta^{18}O_{Ol}$ in the Rocca d'Argimonia peridotites could be favoured by the relatively large crystal size of olivine (1–3 mm in diameter, Table 9).

In the following discussion sections, we will combine the information inferred from microstructures with mineral/whole-rock major element chemistry and O isotopic signature of olivine. Although the Rocca d'Argimonia sequence experienced extensive subsolidus re-equilibration, we will show that our methodological approach successfully brings information about the magmatic processes that gave rise to these deep-seated peridotites.

Sample	BI4/3	BI4/1	BI10/3	BI10/1	BI5/1	BI2/5	BI2/1	BI2/7	BI6/2	BI30/5	BI2/5	BI10/3	BI2/5	BI10/3	BI8/1	BI50/3
Rock type	**Dunites**					**Harzburgites**			**Lherzolites**		**Websterites**		**Gabbronorite dykes**			
Brey & Kohler (1990) Ca-in-Opx	/	751	811	751	743	749	758	752	753	753	/	/	/	/	/	/
Brey & Kohler (1990) Cpx-Opx	/	810	736	719	788	780	771	708	765	747	/	/	/	/	/	/
Wells (1977) Cpx-Opx	/	858	833	816	838	847	817	804	818	804	778	793	810	838	810	830
Holland & Blundy (1994) Amp-Pl	/	/	/	/	/	/	/	/	/	/	/	/	971	1035	979	996
Putirka (2016) Amp	/	/	/	/	/	/	/	/	/	/	/	/	1030	1008	1008	999

Table 11. Temperature estimates (°C) obtained for the selected rocks of the Rocca d'Argimonia sequence. A confining pressure of 0.8 GPa was assumed in the calculations, in agreement with pressure estimates reported by Demarchi et al. (1998) for the base of the Ivrea Mafic Complex. The method of Putirka (2016) was applied using equation 6.

6.2 Evidence for melt–peridotite reaction: the orthopyroxenite–websterite contact zone

The Rocca d'Argimonia peridotites are locally crosscut by hornblende gabbronorite dykes typically showing a thickness variable from few centimetres to few tens of centimetres (Fig. 3b). These dykes display a millimetre-scale thick orthopyroxene-rich zone (54 vol%–94 vol%, Table 10) along the contact with host peridotites, which consists of orthopyroxenite towards the peridotite and hornblende websterite towards the gabbronorite (Fig. 5c). In this section, we relate the development of this orthopyroxenite–websterite contact zone to a reaction driven by the chemical contrast between migrating melts and host peridotites.

The whole-rock chemical compositions of the gabbronorite dykes do not represent melt compositions. In particular, the thin dykes BI2/5 and BI10/3 have anomalously high Mg# of 82–84 (Fig. 6), which most likely reflects a role of host dunites–harzburgites, in response to local dissolution and assimilation of peridotite material by the migrating melt and/or diffusive Fe–Mg exchange between peridotite minerals and melt. The thick dykes BI8/1 and BI50/3 have 74–75 Mg# and relatively low SiO_2/Al_2O_3 values of 2.4–2.7, which indicate a role of plagioclase accumulation (Kempton and Harmon, 1992). However, information about chemical compositions of the melts feeding the gabbronorite dykes may be acquired by mineral chemistry, based on experimentally determined mineral–melt coefficients. This approach assumes that original mineral compositions were not modified in response to the high temperature subsolidus reequilibration in the lower continental crust. Two-pyroxene geothermometry documented granulite facies metamorphic conditions, whereas the amphibole based methods yielded values of ~1000°C (Table 11) that may be related to late magmatic conditions (cf. Nekvasil et al., 2004; Nandedkar et al., 2014). Hence, we used the chemical compositions of amphibole from thick gabbronorite dykes BI8/1 and BI50/3, for which the peridotite contribution was most likely negligible, to compute some compositional characteristics of the feeding melts.

The compilation of magmatic amphibole compositions by Putirka (2016) enables calculating the SiO_2 content of the amphibole equilibrium melts, which corresponds to 50 wt%–51 wt% for the BI8/1 and BI50/3 amphiboles. In addition, Mg# and TiO_2 of amphibole equilibrium melts may be computed assuming amphibole/basalt Fe–Mg and Ti partition coefficients of 0.37 and 2.47, respectively, as resulting from experiments carried out at 1010°C and 0.7 GPa by Nandedkar et al. (2014, 2016). Calculations show that BI8/1 and BI50/3 amphiboles were in equilibrium with melts having 44–47 Mg# and 1.1 wt%–1.2 wt% TiO_2. Amphibole compositions therefore document that the thick gabbronorite dykes crystallized from chemically evolved basaltic melts showing a marked chemical contrast with respect to host peridotites. For instance, the dunites and the harzburgites show 38 wt%–40 wt% SiO_2, 86–90 Mg# and 0.05 wt%–0.10 wt% TiO_2.

We computed the bulk chemical compositions of the microlayers developing at the gabbronorite–peridotite contact (Table A2), based on their mineral and modal compositions. The mean calculated compositions of the two microlayers are compared with the mean compositions of host dunites–harzburgites in Fig. 14. The diagram shows that MgO and FeO_{tot} steadily decrease from the peridotite across the contact zone. Contrary to MgO and FeO_{tot}, Al_2O_3 decreases from the websterite to the orthopyroxenite micro-layer and the peridotite. Cr_2O_3 concentrations are similar in the peridotite and the adjacent orthopyroxenite micro-layer and markedly decrease in the websterite micro-layer. The inferred Al_2O_3 and Cr_2O_3 variations from the peridotite across the contact zone are consistent with the Cr# of orthopyroxene and spinel decreasing from the peridotite to the orthopyroxenite and the websterite micro-layers (Fig. 11). Mass balance calculations also show that the whole contact zone exhibits higher SiO_2 than the dunites–harzburgites. In particular, because of the 18 vol%–22 vol% amphibole amount, the websterite micro-layer has slightly lower calculated SiO_2 (44 wt%–46 wt%) than the orthopyroxenite micro-layer (49 wt%–50 wt%). Finally, CaO, Na_2O and TiO_2 are low in the peridotite and the adjacent orthopyroxenite micro-layer, and they increase in the websterite microlayer, in response to the relatively high proportions of amphibole and clinopyroxene. For instance, calculated TiO_2 is 0.1 wt% and 0.4 wt% for the orthopyroxenite and the websterite micro-layer, respectively.

We propose that the double-layered contact zone formed in response to a two-step reaction progress. The melt–peridotite reaction initiated with the development of the orthopyroxenite micro-layer (step 1). Most likely, the migrating melt had relatively high contents of SiO_2 and Al_2O_3, which triggered the crystallization of orthopyroxene and minor spinel (~7 vol%). The similar Cr_2O_3 contents of the orthopyroxenite micro-layer and dunites–harzburgites (Fig. 14) suggest formation of the orthopyroxenite micro-layer by peridotite replacement, in response to peridotite dissolution by the migrating melt. Following the orthopyroxenite formation, excess CaO, Na_2O and TiO_2 from the reacting melt could promote crystallization of amphibole and clinopyroxene, in association with orthopyroxene and spinel, thereby giving rise to the websterite micro-layer (step 2). Presumably, the relatively low Cr_2O_3 content of the websterite micro-layer (estimated as ~0.2 wt%) reflects the minor Cr_2O_3 content of the migrating melt with respect to host peridotite, the limited Cr diffusion from the peridotite to the melt and the earlier crystallization of spinel in the orthopyroxenite micro-layer. The original melt–peridotite boundary could therefore be the present contact between the orthopyroxenite and the websterite micro-layer. The melt–peridotite reaction also implies that the chemical elements that are incompatible with respect to the websterite mineral assemblage were concentrated in a residual melt, which could ultimately mix with the migrating melt that was not in physical contact

with host peridotite. In particular, a significant proportion of original melt TiO_2 was probably focused into the unreacted migrating melt.

To conclude, upward melt migration into the consolidated peridotites of the Rocca d'Argimonia sequence triggered a reaction that most likely involved dissolution of a millimetre-scale thick peridotite layer, followed by orthopyroxenite and websterite crystallization and mixing of the residual melt with unreacted migrating melt. Such a dissolution–crystallization process is similar to the series of reactions inferred for formation of Cabo Ortegal (Spain) mantle pyroxenites at the metre scale, by reaction between a boninite-type melt and a dunite (Tilhac et al., 2016). We propose that the melts interacting with the Rocca d'Argimonia peridotites were chemically evolved basalts, based on chemical compositions of amphibole from the thick gabbronorite dykes.

6.3 Origin of the harzburgites and the lherzolites by reactive melt migration

Whole-rock and mineral chemistry of the Rocca d'Argimonia peridotites show Mg# decreasing from the dunites to the harzburgites and the lherzolites (Figs. 6, 7 and 8). Hence, the peridotite sequence could hypothetically be related to a fractional crystallization process involving early separation of olivine and accessory spinel, thereby giving rise to the dunites, followed by a stage forming the harzburgites and the lherzolites, ruled by segregation of olivine and accessory spinel together with orthopyroxene and minor clinopyroxene. This process could explain not only the olivine forsterite variations, but also the Mg#–Cr# correlation observed for orthopyroxene and clinopyroxene (Fig. 8), which may be reconciled with a plagioclase-free fractional crystallization process involving accessory spinel segregation. The rough positive correlation provided by the olivine–spinel pairs, with the forsterite proportion and the spinel Cr# decreasing from 90 mol% to 85 mol% and from 29 mol% to 11 mol%, respectively (Fig. 9), could also be consistent with a magmatic evolution controlled by fractionation of olivine and accessory spinel.

Fractional crystallization experiments from anhydrous and hydrous tholeiitic basalts at 0.7 GPa (Villiger et al., 2007; Nandedkar et al., 2014) show that the early olivine-only fractionation stage, forming dunites, is followed by a phase in which olivine crystallizes together with clinopyroxene to give rise to wehrlites. These experimental results therefore argue against formation of the Rocca d'Argimonia peridotites through closed system fractional crystallization, because the chemically evolved Rocca d'Argimonia peridotites (i.e. the harzburgites and the lherzolites) exhibit minor clinopyroxene and a wide range of olivine/orthopyroxene modal ratio (Fig. 4a, Table 9). A process of closed system fractional crystallization controlled by olivine separation is also inconsistent with the forsterite–NiO variations of the Rocca d'Argimonia olivines (Fig. 7), which do not follow the expected olivine fractionation trend (e.g. Su et al., 2016). For instance, olivine from lherzolite BI30/5

displays the lowest forsterite proportion (85 mol%), suggesting formation from a relatively evolved melt, but is characterized by the highest NiO content (0.36 wt%).

In the Rocca d'Argimonia harzburgites, orthopyroxene occurs as poikilitic grains enclosing olivine and spinel (Figs. 3a and 5a). Poikilitic orthopyroxene grains are locally also present in associated lherzolites. Olivine within orthopyroxene typically displays anhedral morphology with lobate boundaries, thereby indicating that olivine was partly dissolved by an orthopyroxene-saturated melt. The poikilitic orthopyroxene therefore might grow from a melt relatively rich in SiO_2 that reacted with olivine and partially digested it. Similar olivine/orthopyroxene replacement relationships were described for other ultramafic magmatic sequences intruding the upper continental crust (Barnes et al., 2016; Kaufmann et al., 2018; Mao et al., 2019). These studies agreed that poikilitic orthopyroxene did not form by closed-system peritectic reaction between olivine and residual melt. Barnes et al. (2016) and Kaufmann et al. (2018) argued for a reaction between olivine and an upward-migrating orthopyroxene saturated melt, which formed by olivine fractionation in the crystal mush below. Mao et al. (2019) proposed that orthopyroxene saturation in the melt was due to SiO_2 addition by wall-rock contamination, mainly based on oxygen isotopic compositions of olivine ($\delta^{18}O$ = 6.1 ‰–7.2 ‰; see also Fig. 10).

The $\delta^{18}O$ variability of the Rocca d'Argimonia olivines also argues for formation of the Rocca d'Argimonia peridotites by an open-system magmatic process. The $\delta^{18}O_{Ol}$ gradually increases from +5.8 ‰ to +6.6 ‰ with lowering forsterite proportion from 90 mol% to 85 mol% (Fig. 10). Fractional crystallization is expected to produce a negligible or minor $\delta^{18}O_{Ol}$ increase (<0.2 ‰) for the limited forsterite range of the Rocca d'Argimonia olivines (e.g. Eiler, 2001; Bindeman et al., 2004; Bucholz et al., 2017; Yao et al., 2019). Hence, the negative $\delta^{18}O$–forsterite correlation of the Rocca d'Argimonia olivines requires an external contaminating source with high $\delta^{18}O$. We will discuss about the nature of this external source in the next discussion section.

The development of an orthopyroxene-dominated reaction zone between the gabbronorite dykes and host peridotites (Fig. 5c) is consistent with the idea (Barnes et al., 2016; Kaufmann et al., 2018; Mao et al., 2019) that poikilitic orthopyroxene in the harzburgites and the lherzolites formed by an open-system reactive melt flux. In the Rocca d'Argimonia peridotites, the occurrence of gabbronorite dykelets showing sinuous boundaries and of gabbronorite dykes with sharp planar boundaries suggests repeated melt injections during peridotite cooling. Hence, buoyant melts could also have pervasively migrated through a high-temperature olivine-rich matrix, thereby causing partial replacement of olivine by orthopyroxene.

Origin of the Rocca d'Argimonia harzburgites–lherzolites by reactive melt migration may explain the lack of correlation between forsterite and NiO contents of olivine (Fig. 7). The lower oceanic

crustal rocks frequently show forsterite–NiO olivine variations deviating from expected olivine fractional crystallization trends, and these divergences are typically interpreted to reflect post-cumulus magmatic reactions (Yang et al., 2019 and references therein). In particular, olivine with higher NiO at a given forsterite content than predicted by olivine fractionation models may be produced by the following (i) decreasing olivine mass, in response to melt-driven partial dissolution, and (ii) a reacting melt having relatively low Mg#, which is associated with a high olivine–melt partition coefficient for Ni (Hart and Davis, 1978).

We envision the following reaction (mineral abbreviations after Whitney and Evans, 2010) for the partial replacement of olivine by poikilitic orthopyroxene in the Rocca d'Argimonia harzburgites–lherzolites:

(R1) Ol + SiO_2-rich melt 1 = Opx + melt 2,

where melt 1 is the buoyantly rising evolved melt, and melt 2 is the fraction of the melt residual after the reaction with olivine. Because olivine is obviously preserved and spinel is also present within the olivine–orthopyroxene association, the reaction envisaged should be properly expressed as

(R2) Ol 1 + Spl 1 + SiO_2-rich melt 1 = Opx + Ol 2 + Spl 2 + melt 2.

This formulation implies that olivine was originally associated with accessory spinel, and that both phases were not completely dissolved in response to the reaction with the infiltrating melt. The occurrence of olivine and spinel among reaction products denotes a conceivable compositional change of these phases ruled by the interaction with the melt. Notably, the relatively high proportion of spinel (6 vol%–9 vol%) hosted by the poikilitic orthopyroxene suggests that spinel might also have precipitated in conjunction with the olivine–melt reaction.

Crystallization of new spinel by melt–peridotite reaction is shown by the orthopyroxenite–websterite reaction zone along the contact between peridotites and crosscutting gabbronorite dykes. Remarkably, the orthopyroxene–spinel pairs from the orthopyroxenite micro-layer, adjacent to the peridotite in the reaction contact zone (Fig. 5c), follow the Cr# spinel–orthopyroxene covariation depicted by the harzburgites–lherzolites (Fig. 11). Assuming that the original spinel (Spl 1 in Reaction R2) was chemically homogeneous, the spinel–orthopyroxene Cr# variations observed for the harzburgites–lherzolites may be mostly related to different melt/crystal matrix ratios, with Cr# diminishing with increasing melt proportion. The low Cr# of orthopyroxene and spinel from the orthopyroxenite micro-layer was presumably due to a relatively high melt/peridotite ratio, which led to total consumption of olivine.

The gabbronorite–peridotite contact zone also includes a significant proportion of clinopyroxene and amphibole, in the websterite micro-layer adjacent to the gabbronorite. The crystallization of

clinopyroxene (2 wt%–14 wt%) and amphibole (1 wt%–2 wt%) in the harzburgites and the lherzolites could therefore be promoted by the process of reactive melt migration. Evidence for late clinopyroxene crystallization is shown by lherzolite BI6/2, in which poikilitic clinopyroxene enclosing olivine and minor spinel occurs (Fig. 5b). The complete reaction for the melt flow process leading to formation of the Rocca d'Argimonia harzburgites–lherzolites may therefore be schematized as follows:

(R3) Ol 1 + Spl 1 + SiO_2-rich melt 1 = Opx + Ol 2 + Spl 2 + Cpx + Amp + melt 2.

In summary, we attribute the development of poikilitic orthopyroxene in the Rocca d'Argimonia harzburgites–lherzolites to diffuse, reactive migration of melts relatively rich in SiO_2 into a crystal matrix consisting of olivine and accessory spinel. Because one of the Rocca d'Argimonia peridotite layers (Fig. 2) entirely consists of harzburgites and minor lherzolites, the process of reactive melt flow must have operated at least at the scale of ~100 m. The peridotites subsequently underwent a similar melt–peridotite reaction, ruled by injection of chemically evolved basalts into solidified peridotites, which produced a millimetrescale orthopyroxenite–websterite layer along the contact with crosscutting gabbronorite dykes (see previous section).

6.4 Origin of the dunites and the process of contaminating melt flow

The Ivrea–Verbano Zone comprises several mantle sequences, mostly at its stratigraphic base (e.g. Balmuccia and Finero massifs), which include dunite bodies formed by focused reactive flow of olivine-saturated melts into lherzolites (Mazzucchelli et al., 2009) or harzburgites (Bussolesi et al., 2019; Corvò et al., 2020). These mantle replacive dunites are compositionally distinct with respect to the most primitive dunites of the Rocca d'Argimonia sequence (Figs. 6–9). For instance, the Balmuccia and the Finero replacive dunites have forsterite-richer olivine and Cr-richer spinel than the Rocca d'Argimonia dunites. A hypothetical mantle origin for the Rocca d'Argimonia dunites is also difficult to reconcile with the peridotite–pyroxenite alternations (Fig. 2) recalling a large-scale magmatic layering.

The microstructural characteristics and the compositional variations observed for the Rocca d'Argimonia dunites indicate that these rocks underwent reactive melt flow, according to Reaction (R3), as envisaged for associated harzburgites–lherzolites. Orthopyroxene from the dunites (1 vol%–5 vol%) is typically interstitial with respect to olivine, or it forms relatively large grains with anhedral morphology, thereby indicating a late growth with respect to olivine. In the forsterite vs. $\delta^{18}O_{Ol}$ diagram (Fig. 10), the dunites, the harzburgites and the lherzolites follow the same trend, with the dunite olivines showing the highest forsterite and the lowest $\delta^{18}O_{Ol}$ values. The whole peridotite sequence of Rocca d'Argimonia may therefore be related to a process of reactive melt flow through

a melt-poor olivine-rich crystal mush or a pre-existing dunite of likely magmatic origin. Following this idea, the studied dunites formed in response to a decrease of melt/crystalline matrix ratio with ongoing melt migration.

The $\delta^{18}O_{Ol}$ of the Rocca d'Argimonia peridotites increases not only with decreasing olivine forsterite proportion (Fig. 10) but also with increasing modal orthopyroxene (Fig. 12). In particular, the $\delta^{18}O_{Ol}$ increases from +5.8 ‰ for dunite BI4/1 to +6.6 ‰ for lherzolite BI30/5, while modal orthopyroxene raises from 1 vol% to 51 vol%. The wide range of modal orthopyroxene in the studied peridotites is therefore attributed to a melt evolution comprising assimilation of crustal material, which promoted the crystallization of orthopyroxene. The $\delta^{18}O_{Ol}$ variability (+6.1 ‰ to +7.2 ‰, Fig. 10) observed for the lherzolites and the olivine websterites from Huangshanxi mafic–ultramafic intrusion (northwestern China) was similarly related to crustal contamination (Mao et al., 2019). In particular, the growth of poikilitic orthopyroxene in these rocks was attributed to downward convection of cool, Si-rich magma from the roof into an olivine-rich crystal mush.

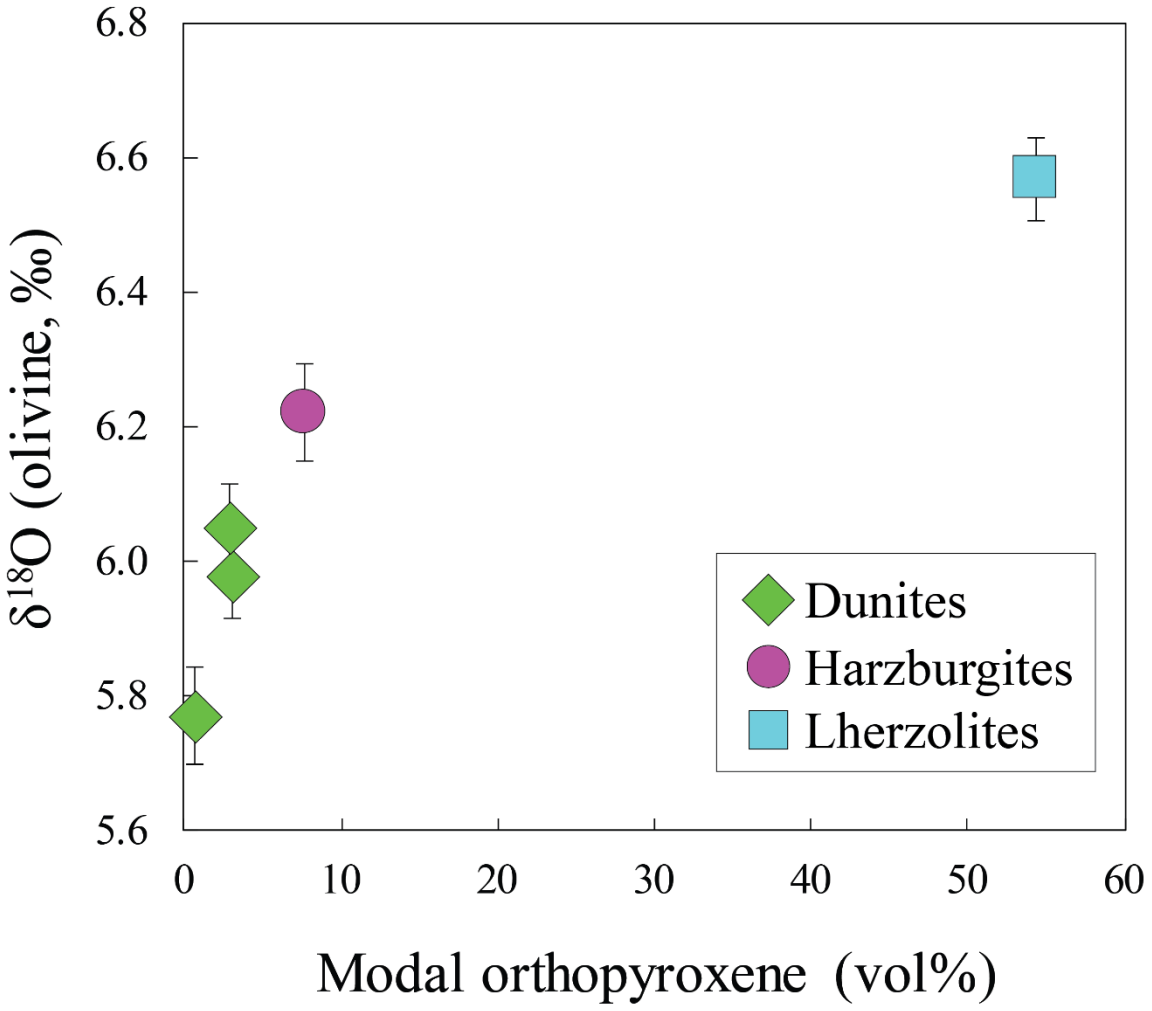

Figure 12. Plot of $\delta^{18}O$ of olivine (weighted average ± 2σ) versus modal orthopyroxene for the Rocca d'Argimonia peridotites.

The Rocca d'Argimonia olivines could crystallize from crustally contaminated magmas. For instance, cooling of a mantle magma emplaced into the lower continental crust could lead to fractional crystallization and concomitant assimilation of basement material (i.e. the AFC process of DePaolo, 1981). Following this hypothesis, the oxygen isotopic signature of olivine was acquired before the reactive melt migration denoted by Reaction (R3). However, we speculate that an AFC-type process would result in direct orthopyroxene crystallization, rather than in the olivine–orthopyroxene replacing relationships (Fig. 5a) typical of the Rocca d'Argimonia harzburgites–lherzolites. The hypothetical AFC-type process is also expected to produce a progressive decrease of forsterite and NiO contents in olivine, which is not observed for the Rocca d'Argimonia peridotites (Fig. 7). Hence, we favour an alternative petrogenetic scenario, which implies that the melt reactively migrating through the olivine-rich matrix possessed a substantial crustal component. Following this model, the reactive melt flow promoted the crystallization of orthopyroxene and modified the mantle-derived $\delta^{18}O$ signature of pre-existing olivine. The envisaged petrogenetic process could be therefore coined as contaminating melt flow.

Two main hypotheses may be formulated for the source of the crustal component. The melt migrating through the olivine-rich matrix could have experienced assimilation of crustal material by mixing with a melt derived from preexisting material of the Ivrea Mafic Complex, either a solid gabbroic rock or a gabbroic crystal mush. This hypothesis is consistent with the Ivrea Mafic Complex made up of gabbroic rocks formed by mantle melts variably contaminated by crustal material (Voshage et al., 1990). Accordingly, the Ivrea Mafic Complex gabbroic rocks have relatively high $\delta^{18}O$ (Fig. 13), which ranges from +6.3 ‰ to +10.1 ‰ (Sinigoi et al., 1991, 1994). In the second hypothesis, the reactively migrating melts mixed with crustal melts released by metasedimentary rocks present at depth, for instance in a septum of country rock embedded within the deepest Ivrea Mafic Complex. The metasediments of the Kinzigite Formation actually have high whole-rock $\delta^{18}O$ ranging from +10.0 ‰ to +14.1 ‰ (Schnetger, 1994) and include quartz grains with $\delta^{18}O$ ranging from +9.1 ‰ to +17.2 ‰ (Baker, 1990).

In spite of the wide range of oxygen isotopic compositions observed for both the rocks of the Kinzigite Formation and the Ivrea Mafic Complex, it is feasible that a lower amount of crustal component is required if the Kinzigite Formation was the contaminant rather than the Ivrea Mafic Complex. The extent of crustal component in the Rocca d'Argimonia peridotites may be roughly evaluated assuming that the $\delta^{18}O_{Ol}$ variations were only related to the process of crustal contamination. The $\Delta\delta^{18}O_{Ol}$ between the most primitive dunite BI4/1 and the most evolved lherzolite BI30/5 (0.8 ‰) implies that the lherzolite had 12% higher crustal contribution than the dunite, if the contaminant material had the average $\delta^{18}O$ of the Kinzigite Formation metasediments (+12.5 ‰, Fig.

13). Assuming the average $\delta^{18}O$ of the mafic rocks from the Ivrea Mafic Complex (+8.1 ‰) as the contaminant material, the lherzolite had 34 % higher mafic crust component than the dunite.

To conclude, we propose that the crustal contamination recorded by the Rocca d'Argimonia peridotites was accomplished by reactive flow of crustally contaminated melts through an olivine-rich spinel-bearing matrix. A possible conceptual model for the contaminating melt flow implies that an evolved melt of mantle origin mixed with a melt derived from either metasedimentary or gabbroic material and subsequently migrates upwards, thereby reacting with the olivine + spinel matrix and ultimately giving rise to the studied peridotites.

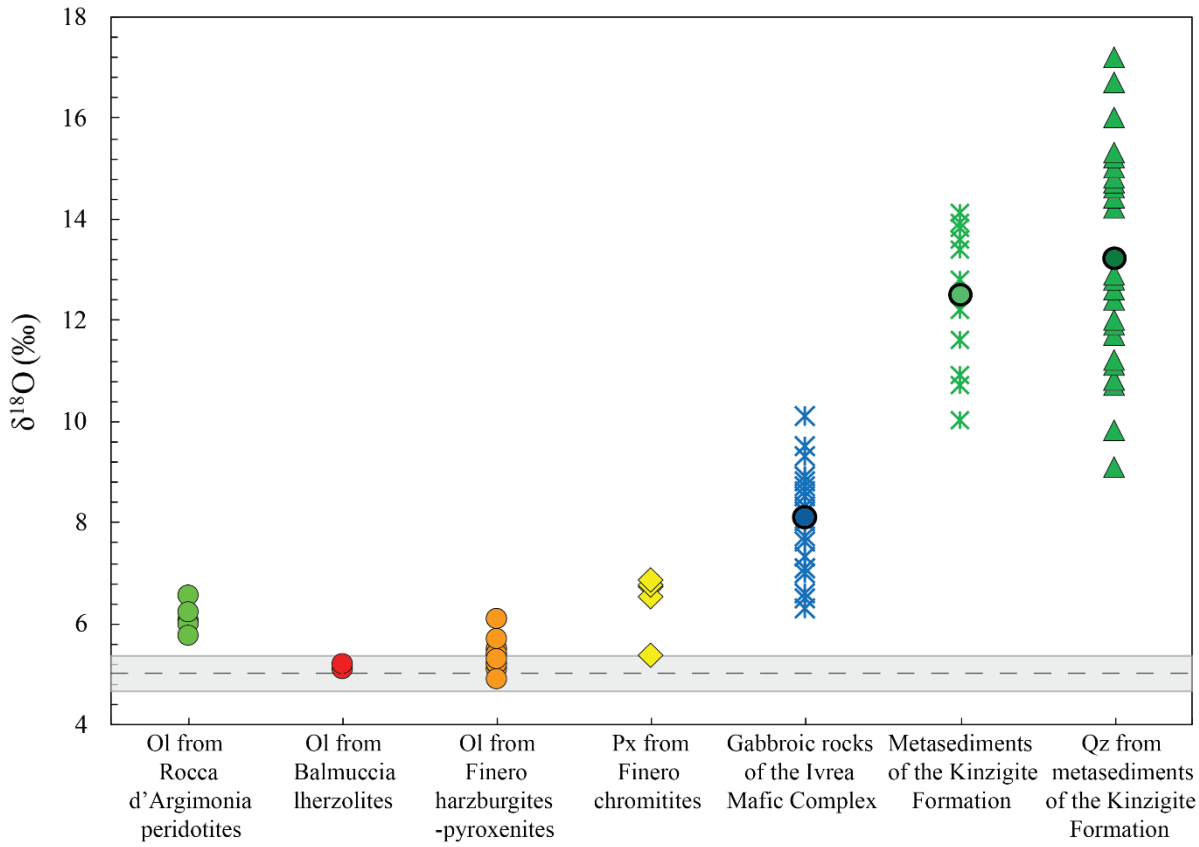

Figure 13. $\delta^{18}O$ of olivine from the Rocca d'Argimonia peridotites compared with $\delta^{18}O$ of other minerals/rocks from the Ivrea–Verbano Zone. Olivines from dunites, harzburgites and lherzolites of Rocca d'Argimonia are reported with the same symbol. Olivine from spinel lherzolites of the Balmuccia mantle sequence after Selverstone and Sharp (2011). Olivine from harzburgites and pyroxenites of the Finero mantle sequence after Selverstone and Sharp (2011). Orthopyroxene and clinopyroxene from chromitites of the Finero mantle sequence after Zanetti et al. (2016). Gabbroic rocks from the Ivrea Mafic Complex after Sinigoi et al. (1991; 1994); the dot represents the mean value of +8.1 ‰. Metasediments of the Kinzigite Formation after Schnetger (1994); the dot represents the mean value of +12.5 ‰. Quartz from metasediments of the Kinzigite Formation after Baker et al. (1990); the dot represents the mean value of +13.2 ‰. The grey field represents the $\delta^{18}O$ of typical mantle olivines (Mattey et al., 1994). Mineral abbreviations after Whitney and Evans (2010).

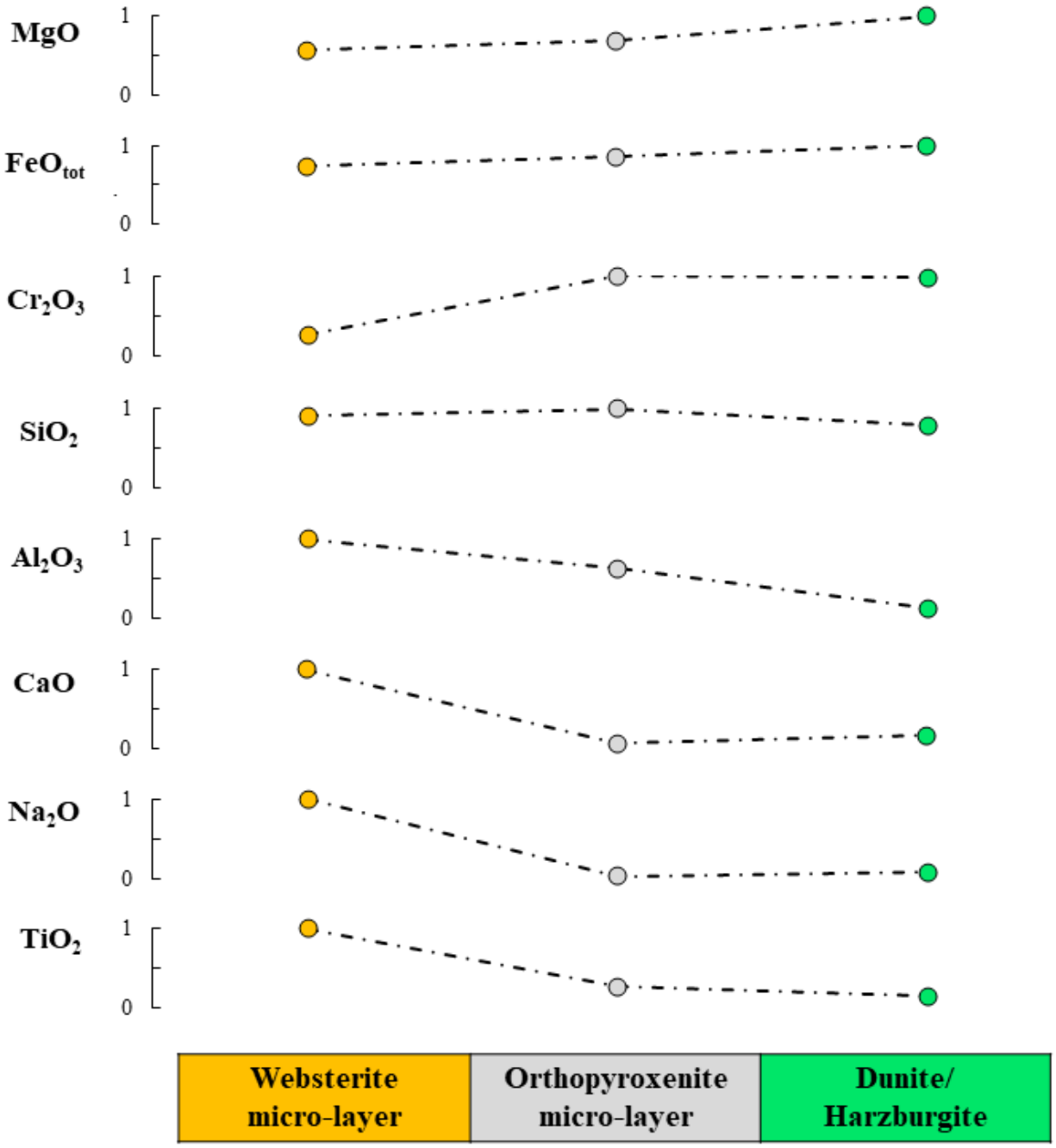

Figure 14. Mean compositions of the Rocca d'Argimonia dunites–harzburgites compared with the mean calculated bulk compositions of orthopyroxenite and websterite micro-layers (Table A2). To show the relative chemical variability from the peridotites across the contact zone, oxide concentrations are normalized to the highest content among peridotite, orthopyroxenite and websterite.

6.5 Implications for mantle sources

The most primitive dunites BI4/1 and BI4/3 of the Rocca d'Argimonia sequence have extremely low orthopyroxene amounts (1 vol%, Table 9). Olivine from these rocks has 89.9 mol% forsterite and 0.34 wt%–0.35 wt% NiO (Fig. 7), and it could therefore be in equilibrium with a primary mantle melt (e.g. Korenaga and Kelemen, 2000). Hence, the most primitive dunites could represent peridotite domains that escaped the process of contaminating melt flow envisaged in the previous section.

The $\delta^{18}O_{Ol}$ of dunite BI4/1 (+5.8 ± 0.1 ‰) slightly exceeds (Fig. 10) the $\delta^{18}O$ range defined by typical mantle olivines (+5.2 ± 0.3 ‰, Mattey et al., 1994). Hence, the melts giving rise to the olivine-rich matrix precursor of the Rocca d'Argimonia peridotites could primarily have anomalously high $\delta^{18}O$, inherited from the mantle source. Locmelis et al. (2016) and Berno et al. (2020) reported similar ideas for other magmatic peridotites from the Ivrea–Verbano Zone, the ultramafic pipes and the Monte Capio–Alpe Cevia sequence, respectively. In particular, they proposed that the primitive melts forming these peridotites were generated from a subcontinental lithospheric mantle variably metasomatized during the Variscan subduction. Notably, olivine and pyroxene from the phlogopite-bearing mantle sequence of Finero (Selverstone and Sharp, 2011; Zanetti et al., 2016), in the northernmost sector of the Ivrea–Verbano Zone, locally show $\delta^{18}O$ exceeding the typical $\delta^{18}O$ mantle range (Fig. 13). These relatively high $\delta^{18}O$ values were attributed to contamination of the Finero mantle sequence through melts sourced in a subducted continental crust, most likely in pre-Permian times (see also Hartmann and Wedepohl, 1993). Hence, the isotopic record in the Finero mantle sequence supports the potential occurrence of mantle sources producing $\delta^{18}O$-enriched primitive melts during the late-post collisional Variscan evolution.

In an alternative petrogenetic scenario, the dunite BI4/1 was affected, to a minor extent, by the process of contaminating melt flow. Following this hypothesis, the low amount of orthopyroxene in this rock, even with respect to clinopyroxene and amphibole, could reflect the evolved nature of the melt reacting with the original olivine-rich matrix. Similar to what is inferred for step 2 of the melt–peridotite reaction forming the contact websterite micro-layer (Fig. 5c), the process of reactive melt flow through the olivine-rich matrix might increase the concentrations of Ca, Na and Ti in the migrating melt. Hence, the highly evolved migrating melts could ultimately lead to a predominance of clinopyroxene and amphibole with respect to orthopyroxene in the mineral reaction products, as observed for the dunites BI4/1 and BI4/3. Assuming that the dunite olivine BI4/1 recorded the process of contaminating melt flow, the olivine-rich matrix precursor of the Rocca d'Argimonia peridotites could for instance originally have +5.5 ‰ $\delta^{18}O$ and 91 mol% forsterite.

We conclude that the process of contaminating melt migration could have erased the original chemical signature of the olivine-rich matrix precursor of the Rocca d'Argimonia peridotites. Further

geochemical investigations are therefore needed to elucidate whether the mantle melts giving rise to the Rocca d'Argimonia ultramafic sequence were derived from mantle sources metasomatized by the Variscan subduction.

7 Summary and concluding remarks

The Ivrea Mafic Complex of the Ivrea Verbano Zone is a ~8 km thick gabbroic–dioritic intrusion in the lower continental crust (e.g. Quick et al., 1992; Sinigoi et al., 2011), developed in conjunction with the post-collisional transtensional regime of the Variscan orogeny (e.g. Handy et al., 1999; Wilson et al., 2004). The Lower Ivrea Mafic Complex includes the peridotite–pyroxenite sequence of Rocca d'Argimonia, which is here considered of magmatic origin, in accordance with Sinigoi et al. (1991) and Quick et al. (2003).

The Rocca d'Argimonia peridotites compositionally range from dunites to harzburgites and minor clinopyroxene-poor lherzolites. Despite the extensive subsolidus re-equilibration under granulite facies conditions, the peridotites and the crosscutting gabbronorite dykes typically retain structures and microstructures of magmatic origin. In particular, the harzburgites and the lherzolites are characterized by the presence of poikilitic orthopyroxenes enclosing partially dissolved olivine and minor spinel. The gabbronorite dykes most likely formed by chemically evolved basalts and show millimetre-scale thick, orthopyroxenite to websterite reaction zones along the contact with host peridotites. The development of these reaction zones is attributed to a melt–peridotite reaction comprising the following: (i) dissolution of a millimetre-scale thick peridotite layer, (ii) orthopyroxenite and websterite crystallization, and (iii) mixing of the melt residual after orthopyroxenite–websterite crystallization with unreacted migrating melt.

The compositional variations of the Rocca d'Argimonia peridotites cannot be related to a magmatic evolution process driven by closed system fractional crystallization. This notion is for instance shown the $\delta^{18}O_{Ol}$ significantly increasing with decreasing olivine forsterite proportion and with increasing modal orthopyroxene. Most likely, the peridotites record a process of reactive melt flow through a melt-poor olivine-rich crystal mush or a pre-existing dunite of likely magmatic origin. We propose that the reactively migrating melts possessed a substantial crustal component, and that they could be compositionally similar to those forming the gabbronorite dykes. The process of contaminating melt flow is considered to be responsible for the olivine dissolution shown by the poikilitic orthopyroxenes in the harzburgites–lherzolites and is inferred to have operated at least at the scale of ~100 m. The nature of the primitive melt forming the precursor olivine-rich matrix remains unknown.

Similar reactive melt flow relationships, with an early olivine-rich matrix percolated by basic melts, were proposed for other peridotite–pyroxenite sequences associated with the Ivrea Mafic Complex of the Ivrea Verbano Zone, namely the so-called ultramafic pipes (Locmelis et al., 2016) and the Monte Capio–Alpe Cevia sequence (Berno et al., 2020). The mineral reaction products in those cases differ in the relatively high proportion of amphibole and, locally, in the presence of

phlogopite, most likely in response to involvement of primitive mantle melts with different compositions. Reactive melt flow through an olivine-dominated matrix in the lower crust, possibly associated with crustal contamination, may therefore represent a common process of large-scale magmatic systems growing in extensional continental settings.

Appendix

Sample	BI4/3	BI4/1	BI10/3	BI10/1	BI5/1	BI2/1	BI2/7	BI6/2	BI30/5	BI2/5	BI10/3	BI8/1	BI50/3
Rock type			**Dunites**			**Harzburgites**		**Lherzolites**		**Gabbronorite dykes**			
SiO_2	39.6	40.0	40.3	39.9	38.9	40.0	41.4	44.3	45.8	48.2	48.9	49.6	48.1
TiO_2	0.06	0.06	0.06	0.05	0.09	0.11	0.06	0.17	0.17	0.36	0.48	0.40	0.38
Al_2O_3	1.45	1.48	1.58	1.37	2.90	2.34	1.82	3.35	4.47	22.2	13.1	18.7	19.6
Cr_2O_3	0.70	0.68	0.49	0.55	1.31	0.89	0.87	0.49	0.67	0.00	0.11	0.02	0.03
FeO (tot)	9.80	9.79	11.2	11.7	11.5	12.1	11.9	11.4	12.0	3.22	5.98	6.26	6.90
MnO	0.15	0.14	0.18	0.15	0.16	0.17	0.18	0.19	0.19	0.08	0.13	0.14	0.14
NiO	0.32	0.33	0.27	0.25	0.32	0.26	0.22	0.14	0.18	0.00	0.03	0.02	0.03
MgO	46.9	46.5	45.1	45.1	43.4	42.9	42.9	36.3	34.7	10.4	14.8	9.91	10.0
CaO	0.95	0.94	0.78	0.83	1.38	1.17	0.68	3.48	1.69	13.9	15.6	13.1	13.2
Na_2O	0.06	0.06	0.05	0.05	0.09	0.08	0.05	0.14	0.12	1.65	0.82	1.75	1.61
K_2O										0.04	0.02	0.05	0.04
Total	100	100	100	100	100	100	100	100	100	100	100	100	100

Table A1. Computed whole-rock chemical compositions of selected samples resulting from mass balance calculations, based on observed mineral compositions (Tables 2 to 7) and estimated mineral proportions (Table 9).

Sample	BI2/5		BI10/3	
Rock type	**Orthopyroxenite**	**Websterite**	**Orthopyroxenite**	**Websterite**
SiO_2	50.0	46.0	48.7	43.8
TiO_2	0.1	0.4	0.1	0.4
Al_2O_3	8.4	13.3	9.9	15.8
Cr_2O_3	0.6	0.2	1.0	0.3
FeO (tot)	9.5	8.0	9.0	8.0
MnO	0.2	0.1	0.2	0.1
NiO	0.1	0.1	0.1	0.1
MgO	30.7	25.6	30.6	24.9
CaO	0.4	5.6	0.4	6.0
Na_2O	0.0	0.7	0.0	0.5
K_2O	0.0	0.1	0.0	0.0
Total	100	100	100	100
Mg#	85.2	85.0	85.8	84.8

Table A2. Computed whole-rock compositions of orthopyroxenite and websterite micro-layers occurring along the contact between peridotites and crosscutting gabbronorite dykes BI2/5 and BI10/3. Calculations were carried out based on mineral (Tables 3 to 6) and modal compositions (Table 10). Volume mineral proportions were converted to weight mineral proportions based on the following densities: orthopyroxene = 3.3 g/cm^3, clinopyroxene = 3.3 g/cm^3, amphibole = 3.2 g/cm^3, spinel = 4.4 g/cm^3. Obtained weight mineral proportions are: (i) 91.8 orthopyroxene and 8.2 spinel for orthopyroxenite BI2/5, (ii) 88.9 orthopyroxene and 11.1 spinel for orthopyroxenite BI10/3, (iii) 56.8 orthopyroxene, 11.8 clinopyroxene, 20.9 amphibole and 10.6 spinel for websterite BI2/5, (iv) 52.4 orthopyroxene, 15.6 clinopyroxene, 16.8 amphibole and 15.2 spinel for websterite BI10/3.

Acknowledgements

We wish to express our gratitude to Jakub Ciazela and Romain Tilhac for their constructive and comprehensive reviews. We also thank Marco Scambelluri and Alberto Vitale Brovarone for stimulating suggestions and Ruben Pilotto for his help during fieldwork. Riccardo Tribuzio acknowledges Silvano Sinigoi for pleasant and inspiring discussions about formation of the Ivrea Mafic Complex.

Chapter II: Origin of the peridotite-pyroxenite sequence from Rocca d'Argimonia, Ivrea Mafic Complex (northern Italy)"

Marta Antonicelli, Riccardo Tribuzio, Tong Liu, Antonio Langone and Fu-Yuan Wu

Manuscript in preparation

Abstract

The lower continental crust section of the Ivrea-Verbano Zone (Italian Alps) was intruded by a ~8 km thick gabbroic-dioritic body (Ivrea Mafic Complex) in the Lower Permian, in conjunction with the post-collisional transtensional regime related to the Variscan orogeny. The present study deals with the origin of the Rocca d'Argimonia mafic-ultramafic magmatic sequence, which is enclosed within the gabbronorites of the lower sector of the Ivrea Mafic Complex. A U-Pb zircon age of 286.0 ± 3.0 Ma has been acquired from these gabbronorites, consistently with a two-point Lu-Hf isochron of 285 ± 22 Ma obtained from clinopyroxene and amphibole separated from a Rocca d'Argimonia dunite. The ~286 Ma age may represent a crystallization age, thereby implying that the Rocca d'Argimonia sequence developed in conjunction with the main phase of the Mafic Complex formation. It cannot be excluded, however, that the ~286 Ma age represents a cooling age, in response to prolonged stay of the Lower Mafic Complex at near solidus temperature conditions. The Sr-Hf isotopic variations of the peridotites suggests formation by melts evolving through fractional crystallization and concomitant assimilation of isotopically enriched crustal material (AFC-type process). The Nd-Sr-Hf isotopic signature of the Rocca d'Argimonia pyroxenites is similar to that of associated peridotites. The lack of a clear radiogenic isotopic distinction between the two rock-types argues against building of the peridotite-pyroxenite sequence through an AFC-type process. In particular, the crystallization of the pyroxenites may be reconciled with a process of pervasive reacting melt flow into an olivine-rich crystal mush. The gabbronorites enclosing the Rocca d'Argimonia sequence show a markedly enriched Nd-Sr-Hf isotopic signature, similar to most gabbroic-dioritic rocks of the Ivrea Mafic Complex. The isotopic and chemical fingerprint of the enclosing gabbronorites documents formation by highly evolved melts possessing a substantial crustal component. These evolved melts were presumably genetically unrelated to the melts forming the peridotite-pyroxenite sequence.

1 Geological setting

The Ivrea-Verbano Zone (Fig. 1) from the inner arc of western Italian Alps exposes a nearly complete section of the pre-Alpine, lower continental crust (e.g., Sinigoi et al., 2016; Pistone et al., 2017), while the Serie dei Laghi represents the upper section of the pre-Alpine continental crust (e.g., Boriani and Giobbi, 2004). To the west and northwest, the Ivrea-Verbano Zone is in tectonic contact with the Austroalpine domain through the Insubric tectonic lineament; to the south and southeast the contact between the Ivrea Verbano Zone and the Serie dei Laghi is defined by two tectonic lineaments, namely the Cossato-Mergozzo-Brissago and the Pogallo Lines (e.g. Sinigoi et al., 2011).

The southwestern sector of the Ivrea-Verbano Zone (Fig. 1) consists of a ~8 km thick gabbroic-dioritic sequence (Mafic Complex) intruding a granulite to amphibolite facies basement (e.g., Quick et al., 1992; Sinigoi et al., 2011), in conjunction with the post-collisional transtensional regime related to the Variscan orogeny (e.g., Handy et al., 1999; Wilson et al., 2004). The basement, locally known as Kinzigite Formation, is made up of metasediments (metapelites with subordinate metagreywackes and impure marbles), minor metabasites and, locally, mantle peridotite blocks (e.g., Quick et al., 1995; Redler et al., 2013). In the Val Strona di Omegna section, adjacent to the northern termination of the Mafic Complex, the basement rocks show pressure and temperature conditions gradually diminishing from ~0.9 GPa and ~940°C near the Insubric Line, to ~0.5 GPa and ~650°C near the Cossato-Mergozzo-Brissago line (see also Kunz and White, 2019). The onset of this metamorphic gradient and the main phase of Mafic Complex formation were inferred to occur at 316 ± 3 Ma (Ewing et al., 2013) and 283.5 ± 2.3 Ma (Karakas et al., 2019).

The Mafic Complex (Fig. 1) was subdivided into two stratigraphically overlying units (Quick et al., 2003). The Lower Mafic Complex is mostly composed of amphibole gabbros that consitute the southwestern sector of the intrusion. The Sesia valley section has been named Layered Zone and subdivided into three domains, the Basal Zone, the Intermediate Zone and the Upper Zone (Rivalenti et al., 1984). The Lower Mafic Complex includes the peridotite-pyroxenite magmatic sequence of Rocca d'Argimonia (Lensch, 1968; Bertolani and Loschi Ghittoni, 1979; Sinigoi et al., 1991). It also includes thin sill-like bodies of cumulus origin which are localized above the Balmuccia mantle sequence. These are ultramafic rocks consisting of dunites, harzburgites and websterites dominated by olivine, orthopyroxene and clinopyroxene (Quick et al., 2003). The Upper Mafic Complex has fairly homogeneous compositions and mainly consists of gabbronorites and, towards the roof, diorites. The lowest level of the Upper Mafic Complex, also referred to as "paragneiss bearing belt", comprises metasedimentary septa and peridotite-pyroxenite sill-like bodies (Rivalenti et al., 1975; Voshage et al., 1990; Sinigoi et al., 1995, 1996). The metasedimentary septa are interpreted as remnants of the Kinzigite Formation that underwent substantial extraction of SiO_2-rich melts in

response to the interaction with melts forming the Mafic Complex. The paragneiss bearing belt also encloses a huge mantle sequence defining a 4.5 km long and 0.8 km wide lens, which is known as Balmuccia peridotite massif (Quick et al., 1995). This mantle body is mostly made up of clinopyroxene-poor lherzolites (e.g., Shervais and Mukasa, 1991) containing replacive dunite lenses (Mazzucchelli et al., 2009) and two major sets of pyroxenite veins dominated by either Cr-diopside or Al-augite (e.g., Voshage et al., 1988; Rivalenti et al., 1995; Mukasa and Shervais, 1999).

Towards the top of the Ivrea Mafic Complex and within the Kinzigite Formation, discordant peridotite-pyroxenite bodies (up to 300 m wide), typically amphibole- and phlogopite-bearing, are exposed (Garuti et al., 2001). They are collectively known as Ultramafic Pipes and most likely formed by primitive alkaline melts at 288-249 Ma (Locmelis et al., 2016; Fiorentini et al, 2018). These Pipes represent a series of metasomatized bodies containing Ni-Cu-PGE sulfide mineralizations (see also Sessa et al., 2017). Along the northern edge of the Mafic Complex, near the Insubric Line, several sill-like peridotite-pyroxenite sequences (up to km-scale in length) crop out (Ferrario et al., 1983; Zaccarini et al., 2014), like the Monte Capio intrusion. These peridotite-pyroxenite sequences are relatively rich in amphibole and phlogopite-free, and formed by H_2O-rich basaltic melts that intruded the lowermost continental crust of the Ivrea-Verbano Zone (Berno et al., 2020). The age of these ultramafic sequences is debated and ranges from 314 ± 5 Ma (Klötzli et al., 2014) to ~200 Ma (Denyszyn et al., 2018).

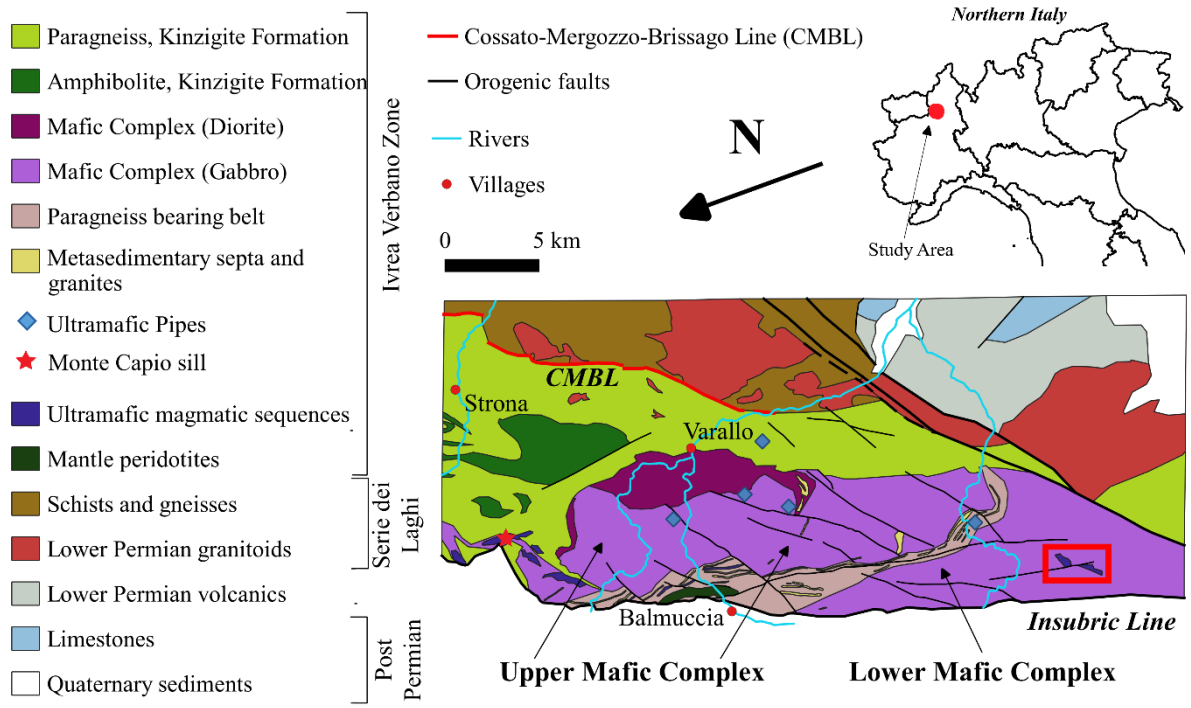

Fig. 1. Geological map of the central Ivrea-Verbano Zone and Serie dei Laghi, after Antonicelli et al. (2020). The North orientation aims at elucidating the inferred Permian stratigraphy. The red frame refers to location of the Rocca d'Argimonia sequence (see Fig. 2).

2 Field relationships and selected samples

The Rocca d'Argimonia ultramafic rocks are enclosed within gabbronorites, which are in turn embedded in the amphibole gabbros of the Lower Mafic Complex (Quick et al., 2003; Antonicelli et al., 2020). Two major ultramafic rock bodies are exposed, characterized by up to 100 m thick peridotite-pyroxenite alternations (Fig. 2). The peridotites are crosscut by up to 0.3 m thick gabbronorite dykes with sharp planar boundaries. Sinuous gabbronorite dykelets (≤2 cm thick) also occur in places, in peridotites and adjacent pyroxenites. Detailed description of petrographic characteristics of peridotites and gabbronorite dykes from Rocca d'Argimonia are reported in Antonicelli et al. (2020).

The pyroxenites are characterized by orthopyroxene modally prevailing over clinopyroxene (77-91 and 8-18 wt%, respectively) and include accessory amounts of plagioclase and amphibole (Fig. 3a-b, Table 1). Orthopyroxene and clinopyroxene typically occur as nearly equant to sub-prismatic grains, thereby defining a nearly granoblastic structure with an average grain size of 1-2 mm. Plagioclase and amphibole are smaller than the pyroxenes and typically display nearly equant morphology and form 120° triple junctions with orthopyroxene and clinopyroxene. Sporadic poikilitic clinopyroxene grains (5-7 mm) also occur. The latter are characterized by: (i) orthopyroxene exsolution lamellae, and (ii) patches (up to hundreds of μm in size) consisting of orthopyroxene and, sporadically, plagioclase and amphibole. Pyroxenite BI50/8 in places includes up to 8 mm long amphibole grains. Spinel also rarely occurs as small grains, with anhedral to elongated shape, interstitial to orthopyroxene and clinopyroxene.

The gabbronorite enclosing the ultramafic sequence frequently exhibit a layering defined by plagioclase/pyroxene and/or amphibole/pyroxene modal variations, and a foliation defined by pronounced alignment of plagioclase, pyroxene, amphibole and, locally, accessory biotite. The gabbronorites have highly variable pyroxene/plagioclase modal ratios (Fig. 3b; Table 1), and orthopyroxene modally prevailing over clinopyroxene (5-17 and 1-9 vol% respectively). Plagioclase, orthopyroxene, clinopyroxene and amphibole typically display fine to medium grained (0.5-2 mm), granoblastic to nearly granoblastic structure; clinopyroxene is typically tinier than orthopyroxene. Amphibole occurs in variable modal amount (up to 53 vol%), and is locally absent. Plagioclase locally shows large sub-prismatic grains (up to 3.5 mm). Ilmenite, magnetite, quartz and apatite are present as accessory phases. Accessory zircon also locally occurs in gabbronorites and is typically localized in amphibole-free portions.

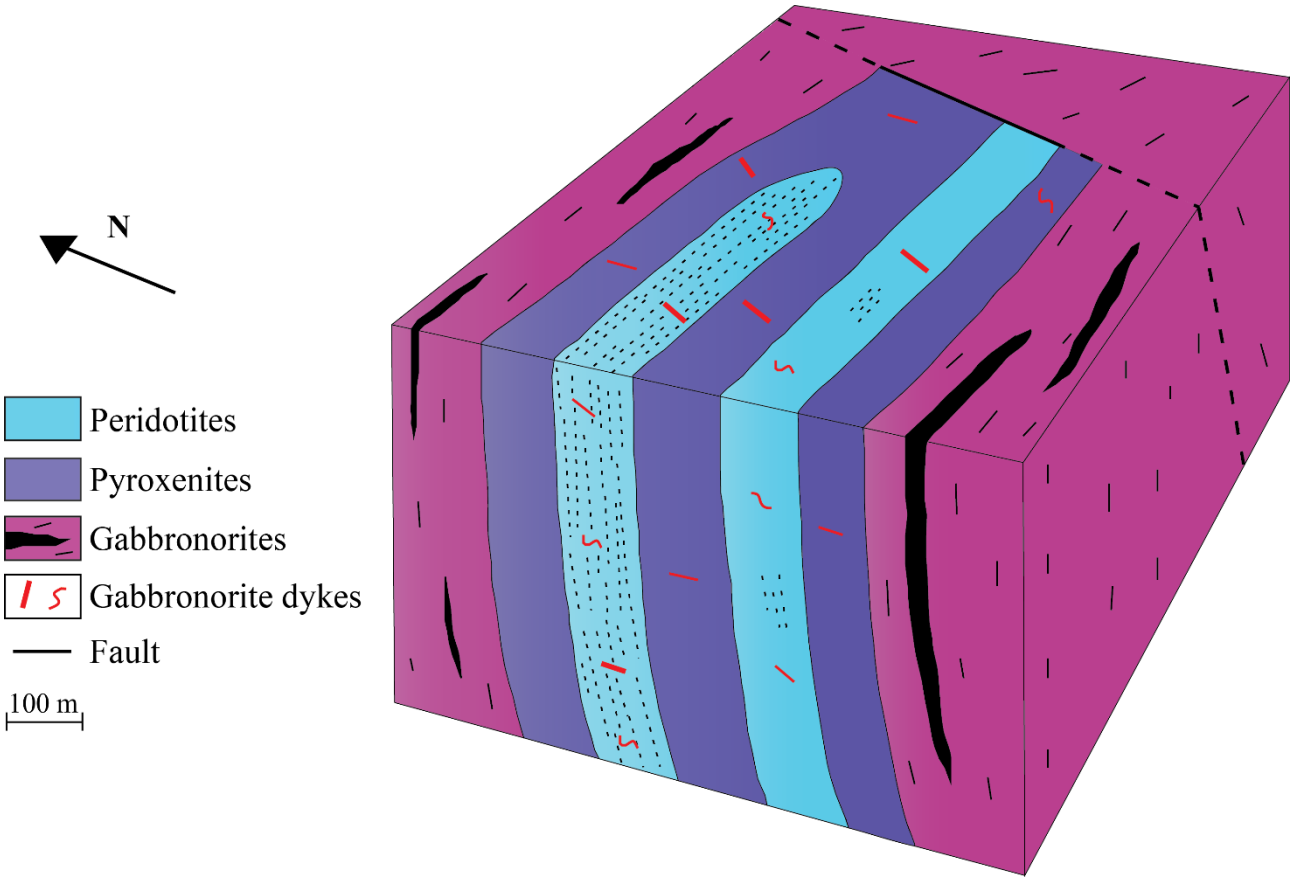

Fig. 2. Synthetic block diagram illustrating the relationships between the different rock types of the Rocca d'Argimonia sequence. The dotted lines within the peridotites represent domains rich in poikilitic orthopyroxene, and the black bands represent amphibole-rich layers within gabbronorites.

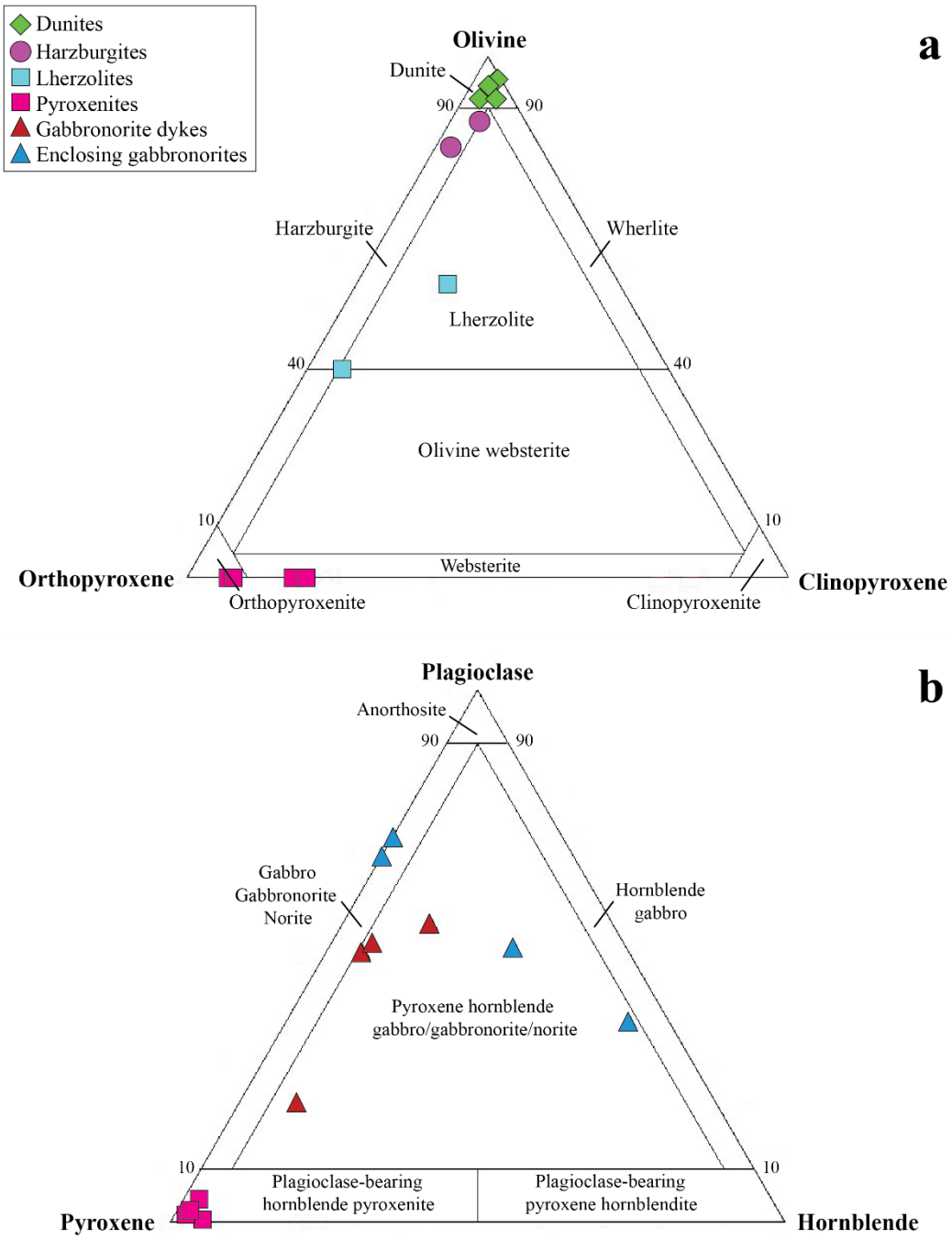

Fig. 3. (a) Peridotite and pyroxenites modal compositions (vol%) reported in the olivine-orthopyroxene-clinopyroxene classification diagram of ultramafic rocks. (b) Modal compositions (vol%) of gabbronorite dykes and of gabbronorites enclosing the ultramafic sequence reported in the plagioclase-total pyroxene-amphibole classification diagram of gabbroic rocks; the compositions of pyroxenites are also reported.

Sample initials	Mineral modes (wt%)								Mineral modes (vol%)								Average grain size of main phases (mm)						Rock nomenclature	Coordinates	
	Opx	Cpx	Amp	Pl	Spl	Opaques	Bt	K-feld	Opx	Cpx	Amp	Pl	Spl	Opaques	Bt	K-feld	Opx	Cpx	Amp	Pl	Spl	Bt		x	y
Pyroxenite BI1/1	79.1	16.7	2.0	2.2	-	-	-	-	78.4	16.9	2.1	2.7	-	-	-	-	1.5	1.5*	0.3	0.3	-	-	Plagioclase-bearing pyroxenite	429893,50	5057797,20
Pyroxenite BI9/2	74.4	18.4	2.5	4.1	0.6	-	-	-	73.4	18.6	2.6	4.9	0.5	-	-	-	2.0	1.5	0.4	0.3	0.3	-	Plagioclase-bearing pyroxenite	429897,00	5057644,16
Pyroxenite BI30/7	89.4	7.6	1.8	1.2	-	-	-	-	89.0	7.7	1.9	1.5	-	-	-	-	1.5	1.0	0.3	0.3	-	-	Plagioclase-bearing pyroxenite	429720,60	5057614,76
Pyroxenite BI50/8	86.5	7.9	4.8	0.5	0.3	-	-	-	86.1	8.0	5.0	0.6	0.2	-	-	-	5.0	5.0	0.5*	0.3	0.2	-	Plagioclase-bearing pyroxenite	429457,80	5056883,00
Gabbronorite BI23/2	12.3	5.9	29.9	51.3	-	0.2	0.4	-	10.4	5.3	27.6	56.2	-	0.1	0.4	-	0.8	0.8	0.8	1.0	-	0.3	Hornblende gabbronorite	429844,50	5057854,17
Gabbronorite BI23/5	21.1	10.0	-	68.2	-	0.7	-	-	17.3	8.7	-	73.6	-	0.4	-	-	0.7	0.7	-	1.0	-	-	Gabbronorite	429838,50	5057849,00
Gabbronorite BI40/4	5.6	0.9	55.9	37.3	-	0.3	-	-	4.8	0.8	52.7	41.5	-	0.2	-	-	1.0	0.7	1.0	1.5	-	-	Hornblende gabbronorite	430032,80	5057086,70
Gabbronorite BI50/10	21.4	5.6	-	70.7	-	0.6	-	1.7	17.0	4.8	-	75.9	-	0.4	-	1.9	1.0	0.7	-	1.7	-	-	Gabbronorite	430741,00	5057492,90
* = large grains are not considered in the average grain size																									

Table 1. Location and main petrographic characteristics of selected samples. Mineral proportion calculations (wt%) were carried out on anhydrous basis, assuming all Fe as Fe^{2+}. We used a least squares mixing program to reproduce the observed whole-rock compositions (Table 5) based on mineral compositions. Computed whole-rock compositions based on observed mineral compositions and estimated mineral proportions are listed in Table 2. Mineral abbreviations are after Whitney and Evans (2010), and rock nomenclature follows the classification of the International Union of Geological Sciences.

Rock type	Pyroxenites				Gabbronorites			
Sample	**BI1/1**	**BI9/2**	**BI30/7**	**BI50/8**	**BI23/2**	**BI23/5**	**BI40/4**	**BI50/10**
SiO_2	52.5	52.2	52.4	52.6	49.1	52.3	45.9	54.9
TiO_2	0.27	0.30	0.30	0.31	0.96	0.73	1.78	0.34
Al_2O_3	5.73	6.24	5.39	5.38	20.19	20.01	19.47	19.99
Cr_2O_3	0.49	0.49	0.54	0.53	0.01	0.02	0.01	0.02
FeO (tot)	9.76	9.30	10.0	10.3	7.9	7.9	10.9	8.2
MnO	0.19	0.19	0.19	0.21	0.15	0.18	0.16	0.18
NiO	0.05	0.03	0.04	0.05	0.08	0.02	0.01	0.02
MgO	26.0	25.5	28.6	27.6	6.9	5.8	6.7	3.7
CaO	4.73	5.48	2.38	2.72	11.03	9.25	11.44	7.65
Na_2O	0.26	0.31	0.14	0.24	3.03	3.46	3.00	4.51
K_2O	0.01	0.01	0.01	0.03	0.62	0.35	0.61	0.48
Total	100.0	100.0	100.0	100.0	100.0	100.0	100.0	100.0

Table 2. Computed whole-rock chemical compositions of selected samples resulting from mass balance calculations, based on observed mineral compositions and estimated mineral proportions (Table 1).

3 Analytical methods

Zircon grains as free as possible from fractures and inclusions were selected by hand picking under a binocular microscope, mounted in epoxy resin and polished down to 1 μm. The internal zoning pattern of the crystal sections was observed by cathodoluminescence (CL) at the scanning electron microscope (SEM). In situ U–Pb geochronology was determined at the Istituto di Geoscienze e Georisorse-C.N.R., Unità di Pavia (Italy) by using an ArF excimer laser microprobe at 193 nm (Geolas200Q-Microlas) with a Triple Quadrupole (QQQ 8900) from Agilent. Analytical conditions are 25 μm in diameter of spot size, 8 J/cm^2 of energy density, and 5 Hz of repetition rate. Laser-induced elemental fractionation and mass bias were corrected using zircon standard (GJ1 zircon, Jackson et al., 2004). The same integration intervals and spot sizes were used on both the external standard and unknowns. During each analytical run reference zircon 91,500 (Wiedenbeck et al., 1995) and Plešovice (Sláma et al., 2008) were analyzed together with the unknowns for quality control. Data reduction was carried out with GLITTER software package (Van Achterbergh et al., 2001). Concordant ages were calculated using the ISOPLOT 3.0 macro for Excel (Ludwig, 2003), concordia diagrams and density plots were obtained by using the IsoplotR software (Vermeesch, 2018).

Whole-rock trace element analyses of selected peridotites and gabbronorite dykes (Table 1) were carried out at Activation Laboratories (Ancaster, Ontario), following commercial package 4Lithores. Sample preparation implies a lithium metaborate/tetraborate fusion and digestion in 5 % nitric acid. Analyses of SiO_2, Al_2O_3, Fe_2O_3, MnO, MgO, CaO, Na_2O, K_2O, TiO_2 and P_2O_5 were performed by inductively coupled plasma optical emission spectroscopy. Cr_2O_3 and NiO contents, together with REE and trace elements, were measured by inductively coupled plasma mass spectroscopy. Detection limits are 0.01 wt% for SiO_2, Al_2O_3, Fe_2O_3, MgO, CaO, Na_2O, K_2O and P_2O_5, 0.001 wt% for MnO and TiO_2, and 0.003 wt% for Cr_2O_3 and NiO. Trace elements' detection limits are included between 0.002 and 5 ppm, whereas Zn detection limit is 30 ppm.

Whole-rock trace element concentrations of five peridotite samples were determined using an Agilent 7500a ICP-MS instrument at the MC-ICPMS Laboratory, Institute of Geology and Geophysics, Chinese Academy of Sciences, Beijing, using procedures similar to those outlined in Yang et al. (2012). Prior to analysis, 50 mg of sample powder was dissolved in a mixture of HNO_3 and HF, and was heated then at 195°C for 72 h. The solution was then evaporated and refluxed with HNO_3 and re-dissolution in a mixed acid of 6N HNO_3 at 165°C for additional 48 h. The sample was subsequently diluted with Rh internal standard and Milli-Q water.

The Hf, Sr and Nd isotopic compositions and Lu-Hf, Rb-Sr, Sm-Nd concentrations were measured on whole-rock samples, amphibole and clinopyroxene separates. The amphiboles and clinopyroxenes were checked under a binocular microscope and handpicked. The Lu-Hf and Sm-Nd data were

obtained at State Key Laboratory of Lithospheric Evolution (Institute of Geology and Geophysics, Chinese Academy of Sciences, Beijing) using a Thermo Fisher Scientific Neptune Plus (Bremen, Germany) MC-ICP-MS, equipped with nine Faraday cups. A detailed description of this instrument can be found in Weyer and Schwieters (2003) and Wu et al. (2006).

In Lu-Hf procedure samples were initially dissolved by acid digestion and then processed through columns with HCl, HNO_3 and HF acids for chemical dissolution (complete procedure in Yang et a., 2010). The mass bias behavior of Lu was assumed to follow that of Yb for the interference correction of ^{176}Yb on ^{176}Lu using the exponential law (Vervoort et al., 2004). The Hf isotopic data were reduced off-line in order to correct for instrumental mass bias and tracer contribution with normalization to $^{179}Hf/^{177}Hf = 0.7325$ using the exponential law. The concentrations of Lu and Hf were determined using the isotope dilution equation (see also Yang et al., 2010 and Ma et al., 2019).

Complete procedure for Sm-Nd sample preparation is available in Yang et al., 2010 and Chu et al., 2014. The Nd standard solution was corrected for mass bias by measuring $^{146}Nd/^{144}Nd = 0.721929$ and using the exponential law (Russell et al., 1978). Nd concentrations were calculated from the corrected $^{150}Nd/^{144}Nd$ mixture ratio, using the isotope dilution equation. The data reduction was performed computing interference corrections and spike subtractions, followed by a mass fractionation correction using the exponential law ($^{146}Nd/^{144}Nd = 0.7219$). These calculations are performed cycle by cycle. In the case of the Sm isotopic measurements, the $^{147}Sm/^{149}Sm$ ratio for the spiked samples was externally corrected for mass bias by measuring Alfa Sm standard solution ($^{147}Sm/^{149}Sm = 1.0868032$). Then the Sm concentration of the actual sample is calculated from the corrected $^{147}Sm/^{149}Sm$ ratio, using the isotope dilution equation (Yang et al., 2010).

Sample preparation for Rb-Sr is described in (Yang et al., 2010), then the analyses were performed through Thermal ionization mass spectrometry using a Triton Plus instrument (ThermoFisher) at the Institute of Geology and Geophysics, Chinese Academy of Sciences (IGGCAS) in Beijing. Approximately 1 mL of 0.20M H_3PO_4 was first dried on a ~1mm spot in the middle of the Ta filament at 0.8 A. The Sr analyte was dissolved with 1 mL of 2.5M HCl, then loaded on the spot and dried at 1.0 A. Once the sample was dry, the current was then increased further to ~2 A until a dull red glow was achieved for 4 s. ^{88}Sr ion beam intensities of 5–7 V were obtained for all samples with 1–5 mg sample loading sizes. Data acquisition was started when the signal intensity of ^{88}Sr had reached ~4 V. The ^{87}Sr signal intensity was corrected for the potential bias caused by the remaining isobaric overlap of ^{87}Rb on ^{87}Sr using an $^{87}Rb/^{85}Rb$ value of 0.385041 before mass fractionation correction. Then, corrected $^{87}Sr/^{86}Sr$ values were normalized to $^{88}Sr/^{86}Sr = 8.375209$ using an exponential law (Li et al., 2015 and references therein). Usually, a single analysis consisted of minimum of 140 ratios (7 blocks of 20 cycles). See Li et al. (2015) for complete instrument tuning and sample preparation.

4 U-Pb zircon geochronology

The samples considered for U-Pb zircon geochronology were collected from gabbronorites enclosing the Rocca d'Argimonia peridotite-pyroxenite sequence. In particular, we selected the amphibole gabbronorite BI40/4 and the amphibole-free gabbronorite BI50/10.

4.1 Amphibole gabbronorite BI40/4

This sample gave a uniform population of sub-rounded zircons that are clear and bright, and 80 to 200 μm in diameter. Within the zircon population, grains exhibit many colors, including white clear, white milky, pale yellow and dark yellow. CL images show that the core of some grains consists of heterogeneous domains with patchy zoning locally containing mineral inclusions (Fig. 4a-d). Similar inner structures were observed in zircons from the Lower Mafic Complex, called "mantle domains", which were interpreted to represent a stage of rapid zircon growth associated with the incorporation of micron-sized crystals (Peressini et al., 2007). Some zircon grains show a faint oscillatory zoning with low cathodoluminescence emission contrast (Fig. 4c). The core of these faintly zoned crystals is in places homogeneously grey (Fig. 4b). Most grains display a thick white bright rim, up to 50 μm in thickness (Fig. 4a-b-c-d). Similar bright rims were frequently observed in zircons from the Lower Mafic Complex (e.g., the "white pest" zircons of Peressini et al., 2007). The zircon bright rims are typically characterized by low U contents and interpreted as the result of fluid-assisted zircon recrystallization (see also Vavra et al., 1999).

The U-Pb analyses were conducted on zircon cores characterized by faint-absent oscillatory zoning and on zircon thick bright rims. In particular, thirty-six spot analyses were performed, on thirty-three zircons (Table 3). I obtained eleven concordant data, with U-Pb discordance $<\pm 2\%$, and ten sub-concordant data, with U-Pb discordance $<\pm 10\%$.

Eight concordant core spot dates yielded a mean concordia age of 286.6 ± 4.6 Ma (2σ, MSWD of concordance = 0.05). Combining the eight concordant dates with the five sub-concordant U-Pb dates obtained by zircon cores, we obtained a similar mean concordia age of 286.3 ± 3.7 Ma (2σ, MSWD of concordance = 0.22; Fig. 5b and Table 4).

Analyses from the rim portion of zircons typically show high percentage of discordance and high errors, presumably related to the low U contents. Three concordant rim spot ages yielded a mean concordia age of 285.0 ± 11 Ma (2σ, MSWD of concordance = 0.66). Combining the three concordant data with the five sub-concordant U-Pb ages obtained by zircon rims, we obtained a mean concordia age of 290.2 ± 5.9 Ma (2σ, MSWD of concordance = 0.63; Table 4).

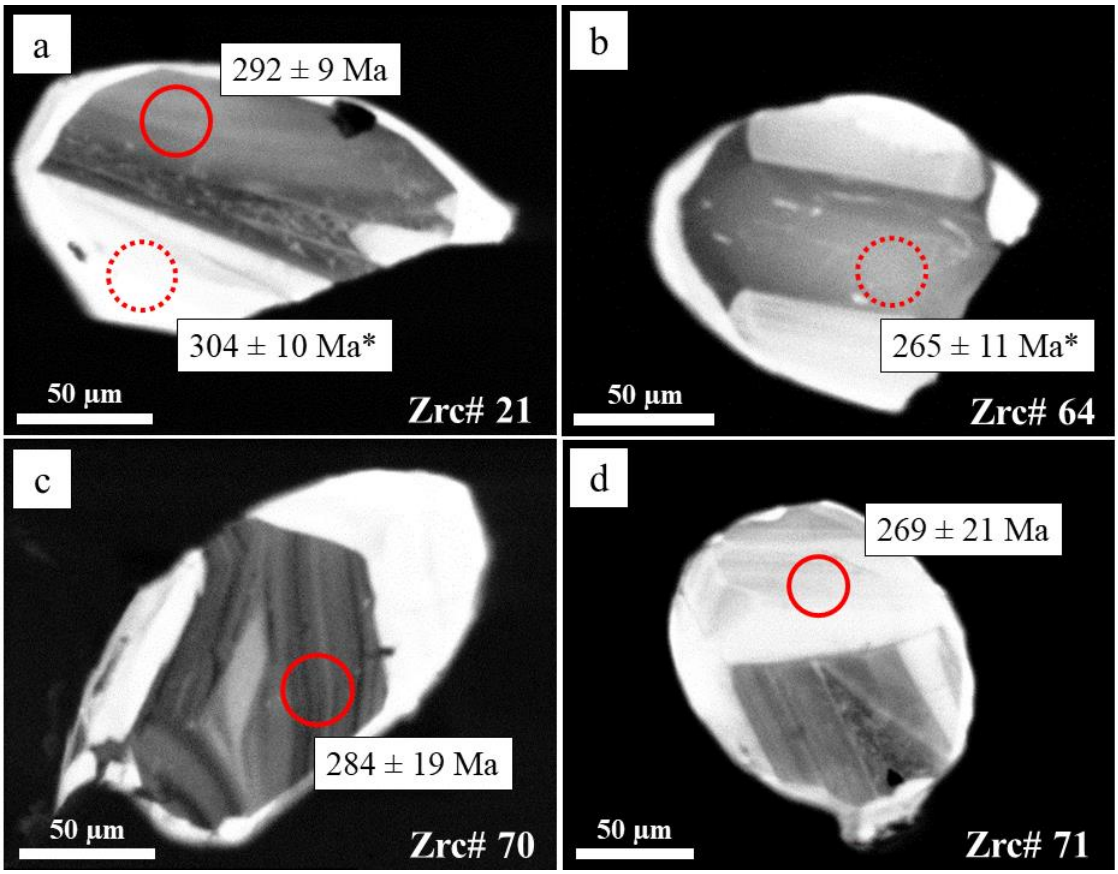

Fig. 4. SEM-CL image of zircon grains from amphibole gabbronorite sample BI40/4. U-Pb spot analyses yielding concordant (red circles) and discordant (dotted circles; * = $^{206}Pb/^{238}U$) ages.

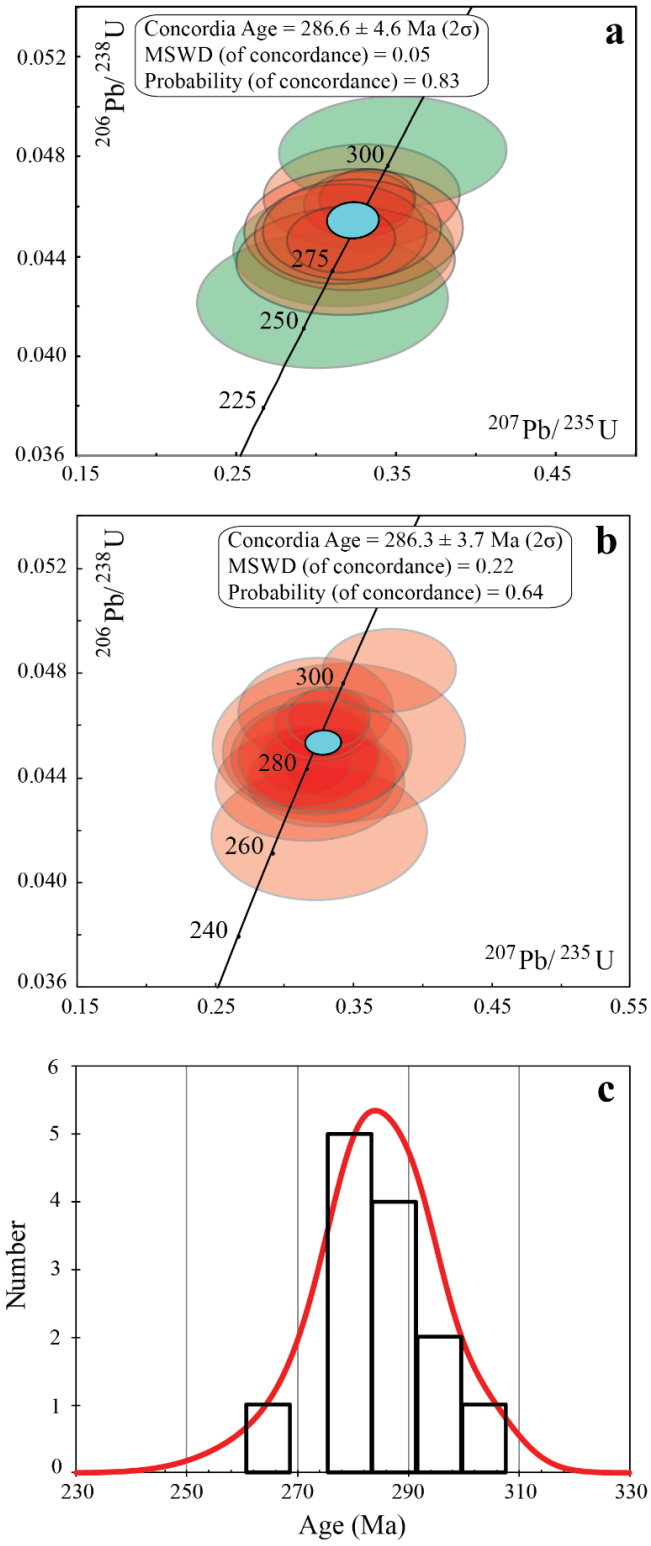

Fig. 5. U–Pb geochronology data on zircons from sample BI40/4. (a) Concordia diagram of concordant dates: cores (red) and rims (green); error ellipses are 2σ. The light blue ellipse represents mean concordia age of core dates (286.6 ± 4.6 Ma, 2σ). (b) Concordia diagram of concordant and discordant core dates; error ellipses are 2σ. The light blue ellipse represents the mean value of concordant and sub-concordant core dates (286.3 ± 3.7 Ma, 2σ). (c) Probability density plot of concordant and sub-concordant $^{206}Pb/^{238}U$ (± 1σ) core dates.

4.2 Gabbronorite BI50/10

Two main zircon populations were found in this sample. One population has rounded shape (80 to 230 μm) and the other consists of elongated prisms (100 to 260 μm). Both zircon populations display white clear, white milky and pale-yellow colors. The rounded zircons are characterized by thick bright CL rims (typically ~25 μm) and cores showing faint oscillatory (Fig. 6d) to patchy zoning. The elongated zircons (Fig. 6c) typically show cores characterized by magmatic oscillatory zoning with light grey intermediate areas (up to 30 μm) and a thin CL bright rim (up to 10 μm in thickness; Fig. 6a-c).

The analyses were mainly carried out at the cores and intermediate domains of the zircon grains, characterized by faint-absent oscillatory zoning. Only few analyses were carried out on the thick bright rims. In particular, thirty-five U-Pb analyses were performed on thirty zircons, obtaining fifteen concordant data, with U-Pb discordance <±2%, and eighteen sub-concordant data, with U-Pb discordance <±10% (Table 3).

Nine concordant core spot dates yielded a mean concordia age of 285.4 ± 4.9 Ma (2σ, MSWD of concordance = 0.001). Combining the nine concordant dates with the seven sub-concordant core dates, we obtained a mean concordia age of 279.5 ± 4.1 Ma (95% confidence level, MSWD of concordance = 1.8; Fig. 7b and Table 4). Notably, the mean concordia age obtained considering only the core spots of prismatic zircons, both concordant and subconcordant dates, is 276.6 ± 3.7 Ma (2σ, MSWD of concordance = 1.6, n = 10), significantly younger than the age of 286.2 ± 5.7 Ma (2σ, MSWD of concordance = 0.33, n = 6) returned from the core spots of rounded zircons, both concordant and subconcordant dates.

Analyses from the zircon rims typically show high percentage of discordance and high errors, presumably related to low U concentrations. Six concordant rim spot dates yielded a mean concordia age of 292.7 ± 7.5 Ma (2σ, MSWD of concordance = 1.40). Combining these concordant dates with the nine sub-concordant U-Pb dates obtained from zircon rims, we acquired a mean concordia age of 288.9 ± 4.1 Ma (2σ, MSWD of concordance = 0.001; Table 4).

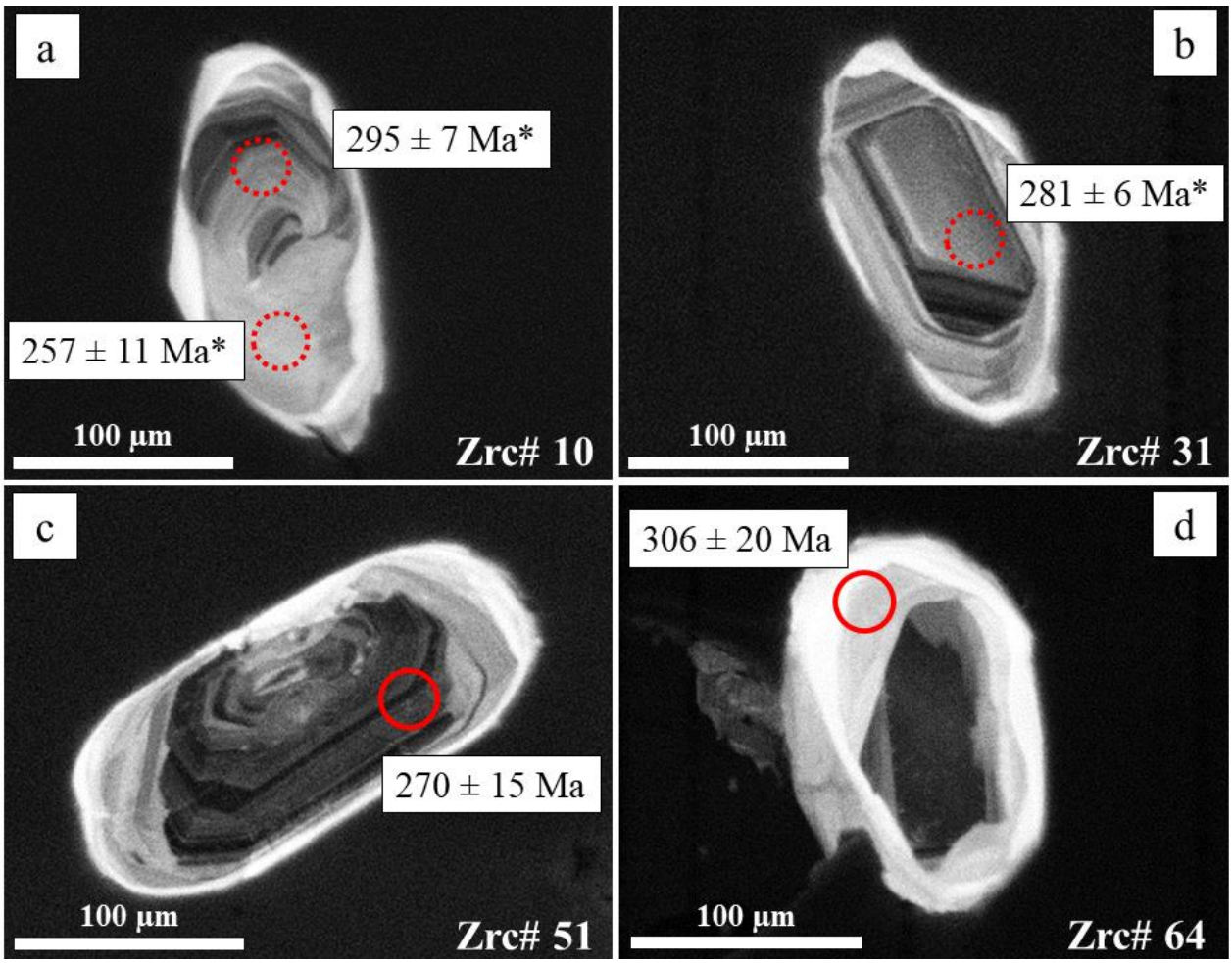

Fig. 6. SEM-CL image of zircon grains from gabbronorite sample BI50/10. U–Pb spot analyses yielding concordant (red circles) and discordant (dotted circles; * = $^{206}Pb/^{238}U$) ages. Photos 6a to 6c = elongated zircons; photo 6d = rounded zircon.

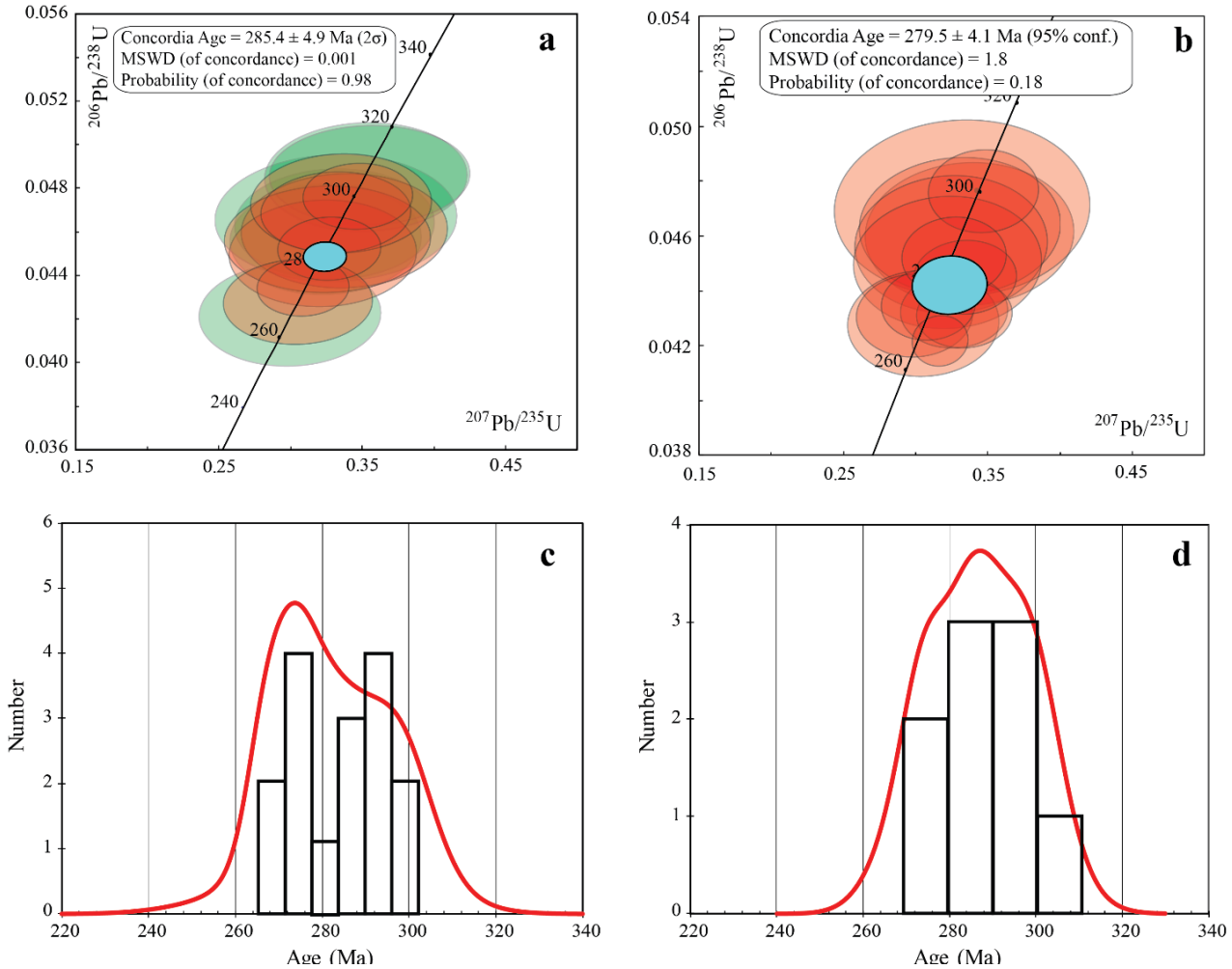

Fig. 7. U–Pb geochronology data on zircons from sample BI50/10. (a) Concordia diagram of concordant dates: cores (red) and rims (green); error ellipses are 2σ. The light blue ellipse represents the mean concordia age of core dates (285.4 ± 4.9 Ma, 2σ). (b) Concordia diagram of concordant and sub-concordant core dates; error ellipses are 2σ. The light blue ellipse represents the mean value of concordant and sub-concordant core dates (279.5 ± 4.1 Ma, 95% confidence level). (c) Probability density plot of concordant and sub-concordant $^{206}Pb/^{238}U$ (± 1σ) core dates. (d) Probability density plot of concordant $^{206}Pb/^{238}U$ (± 1σ) dates.

Identifier	Zrc#	Position	Shape	$^{207}Pb/^{206}Pb$	1s %	$^{207}Pb/^{235}U$	1s %	$^{206}Pb/^{238}U$	1s %	Rho*	$^{207}Pb/^{206}Pb$	1s abs	$^{207}Pb/^{235}U$	1s abs	$^{206}Pb/^{238}U$	1s abs	% U-Pb disc
Amphibole gabbro BI40/4																	
039SMPL	64	Core	Rounded	0.05629	0.010	0.32516	0.052	0.04192	0.002	0.033	464	79	286	45	265	11	7.4
040SMPL	69	Rim	Rounded	0.05222	0.009	0.30391	0.052	0.04223	0.002	0.034	295	54	269	46	267	11	1.0
016SMPL	27	Core	Rounded	0.0516	0.019	0.30175	0.108	0.04240	0.002	0.020	268	96	268	96	268	14	0.0
034SMPL	51	Core	Rounded	0.08187	0.021	0.47869	0.119	0.04244	0.002	0.021	1242	320	397	99	268	16	32.5
045SMPL	84	Rim	Rounded	0.04979	0.009	0.29381	0.051	0.04281	0.002	0.037	185	35	262	45	270	12	-3.3
010SMPL	16	Rim	Rounded	0.10671	0.028	0.63097	0.164	0.04286	0.003	0.017	1744	465	497	129	271	17	45.5
031SMPL	44	Core	Rounded	0.06323	0.020	0.37523	0.115	0.04307	0.003	0.024	716	224	324	99	272	17	16.0
035SMPL	52	Rim	Rounded	0.05939	0.012	0.35733	0.072	0.04366	0.002	0.028	581	122	310	63	275	13	11.2
046SMPL	88	Rim	Rounded	0.07213	0.027	0.43413	0.160	0.04367	0.004	0.022	990	375	366	135	276	22	24.7
038SMPL	58	Rim	Rounded	0.06763	0.045	0.40749	0.266	0.04371	0.005	0.018	857	567	347	226	276	29	20.5
033SMPL	47	Core	Rounded	0.08718	0.029	0.52535	0.171	0.04374	0.003	0.020	1364	458	429	140	276	21	35.6
027SMPL	35	Core	Rounded	0.05274	0.008	0.31844	0.045	0.04380	0.001	0.031	318	47	281	40	276	9	1.6
026SMPL	34	Core	Rounded	0.05385	0.006	0.32663	0.035	0.04401	0.001	0.034	365	41	287	31	278	8	3.3
037SMPL	55	Rim	Rounded	0.05196	0.008	0.31711	0.046	0.04429	0.002	0.033	284	43	280	40	279	10	0.1
029SMPL	36	Rim	Rounded	0.05871	0.009	0.35856	0.052	0.04431	0.002	0.030	556	83	311	45	279	10	10.2
032SMPL	46	Core	Rounded	0.06965	0.056	0.42603	0.338	0.04441	0.006	0.018	918	740	360	286	280	39	22.3
009SMPL	12	Rim	Rounded	0.10235	0.036	0.62722	0.217	0.04442	0.003	0.016	1667	590	494	171	280	22	43.3
019SMPL	32	Core	Rounded	0.05422	0.004	0.33388	0.023	0.04465	0.001	0.038	380	27	293	20	282	5	3.7
017SMPL	28	Core	Rounded	0.05123	0.004	0.31565	0.022	0.04467	0.001	0.039	251	19	279	20	282	5	-1.1
036SMPL	53	Core	Rounded	0.05097	0.006	0.31534	0.035	0.04489	0.001	0.037	239	29	278	31	283	8	-1.7
030SMPL	41	Core	Rounded	0.05193	0.006	0.32259	0.037	0.04507	0.001	0.036	282	34	284	32	284	8	-0.1
042SMPL	70	Core	Rounded	0.05205	0.008	0.32339	0.045	0.04508	0.002	0.036	288	43	285	40	284	10	0.1
043SMPL	79	Core	Rounded	0.05433	0.010	0.33960	0.060	0.04535	0.002	0.033	385	73	297	53	286	13	3.7
028SMPL	36	Core	Rounded	0.05908	0.012	0.37156	0.072	0.04568	0.002	0.030	570	117	321	63	288	14	10.2
015SMPL	26	Rim	Rounded	0.05726	0.005	0.36158	0.032	0.04578	0.001	0.032	502	46	313	28	289	6	7.9
007SMPL	5	Core	Rounded	0.05142	0.004	0.32676	0.023	0.04608	0.001	0.038	260	19	287	20	290	5	-1.2
011SMPL	21	Core	Rounded	0.05195	0.003	0.33193	0.020	0.04631	0.001	0.040	283	17	291	17	292	5	-0.3
014SMPL	24	Core	Rounded	0.05128	0.007	0.32831	0.041	0.04640	0.001	0.034	253	32	288	36	292	9	-1.4
018SMPL	30	Rim	Rounded	0.04948	0.007	0.31845	0.046	0.04667	0.002	0.033	171	25	281	41	294	9	-4.8
006SMPL	4	Rim	Rounded	0.05528	0.005	0.35609	0.029	0.04668	0.001	0.036	424	36	309	25	294	7	4.9
008SMPL	6	Core	Rounded	0.05659	0.005	0.37573	0.032	0.04813	0.001	0.033	476	41	324	27	303	7	6.4
020SMPL	33	Rim	Rounded	0.05235	0.007	0.34781	0.047	0.04819	0.001	0.031	301	42	303	41	303	9	-0.1
012SMPL	21	Rim	Rounded	0.05926	0.009	0.39445	0.055	0.04825	0.002	0.029	577	83	338	47	304	10	10.0
013SMPL	22	Rim	Rounded	0.08470	0.035	0.58645	0.240	0.05020	0.004	0.017	1309	546	469	192	316	26	32.6
044SMPL	83	Rim	Rounded	0.08087	0.047	0.58997	0.335	0.05294	0.005	0.016	1218	704	471	267	333	33	29.4
041SMPL	70	Rim	Rounded	0.05491	0.010	0.41068	0.068	0.05427	0.002	0.033	409	73	349	58	341	14	2.5

Table 3. U-Pb isotopic data from zircons from amphibole gabbro BI40/4 and gabbronorite BI50/10. Accuracy and reproducibility were checked by repeated analyses (n = 25) of reference zircon GJ-1, whereas 91,500 and Plešovice reference zircons were analysed a few times within the run; data given as mean with 1 standard deviation uncertainties. (*) rho is the $^{206}Pb/^{238}U/^{207}Pb/^{235}U$ error correlation coefficient.

Identifier	Zrc#	Position	Shape	$^{207}Pb/^{206}Pb$	1s %	$^{207}Pb/^{235}U$	1s %	$^{206}Pb/^{238}U$	1s %	Rho*	$^{207}Pb/^{206}Pb$	1s abs	$^{207}Pb/^{235}U$	1s abs	$^{206}Pb/^{238}U$	1s abs	% U-Pb disc
Gabbronorite BI50/10																	
012SMPL	10	Rim	Elongated	0.06172	0.011	0.34578	0.062	0.04063	0.002	0.029	664	122	302	54	257	11	14.9
020SMPL	36	Core	Rounded	0.03795	0.011	0.21833	0.061	0.04172	0.002	0.035	-489	-138	201	56	263	13	-31.4
009SMPL	7	Core	Elongated	0.05459	0.002	0.31731	0.013	0.04214	0.001	0.049	395	16	280	11	266	4	4.9
040SMPL	73	Rim	Rounded	0.05147	0.007	0.2994	0.042	0.0422	0.002	0.037	262	37	266	37	266	10	-0.2
030SMPL	51	Core	Elongated	0.05174	0.006	0.3052	0.034	0.04279	0.001	0.037	274	31	270	31	270	8	0.1
038SMPL	71	Rim	Rounded	0.05384	0.016	0.31914	0.092	0.04301	0.003	0.032	364	107	281	81	271	18	3.5
015SMPL	24	Core	Elongated	0.05039	0.005	0.29917	0.027	0.04305	0.001	0.038	213	19	266	24	272	6	-2.2
008SMPL	5	Core	Elongated	0.05619	0.004	0.33412	0.022	0.04311	0.001	0.038	460	30	293	19	272	5	7.0
007SMPL	1	Core	Rounded	0.0548	0.004	0.32673	0.025	0.04323	0.001	0.036	404	31	287	22	273	6	5.0
014SMPL	18	Core	Elongated	0.05154	0.004	0.30889	0.021	0.04345	0.001	0.041	265	18	273	19	274	5	-0.3
016SMPL	26	Rim	Rounded	0.05558	0.008	0.33334	0.048	0.04349	0.002	0.031	436	64	292	42	274	10	6.1
028SMPL	48	Rim	Rounded	0.04911	0.007	0.29963	0.041	0.04427	0.001	0.036	153	21	266	36	279	9	-4.9
017SMPL	31	Core	Elongated	0.05449	0.004	0.33429	0.023	0.04448	0.001	0.038	391	27	293	20	281	6	4.2
027SMPL	46	Rim	Rounded	0.05493	0.010	0.33833	0.059	0.04467	0.002	0.031	409	72	296	51	282	11	4.8
035SMPL	68	Core	Rounded	0.05198	0.007	0.32255	0.043	0.04502	0.002	0.037	285	39	284	38	284	10	0.0
018SMPL	34	Core	Rounded	0.05243	0.004	0.32709	0.024	0.04524	0.001	0.040	304	22	287	21	285	6	0.7
037SMPL	69	Rim	Elongated	0.04886	0.006	0.30592	0.039	0.04543	0.002	0.040	141	18	271	35	286	10	-5.7
042SMPL	81	Rim	Elongated	0.0475	0.009	0.29804	0.055	0.04551	0.002	0.037	74	14	265	49	287	13	-8.3
033SMPL	58	Rim	Elongated	0.05177	0.008	0.32588	0.047	0.04567	0.002	0.034	275	41	286	42	288	10	-0.5
043SMPL	85	Core	Elongated	0.05157	0.007	0.32466	0.044	0.04567	0.002	0.038	266	37	285	39	288	11	-0.8
045SMPL	87	Core	Rounded	0.05316	0.008	0.33749	0.048	0.04605	0.002	0.036	336	48	295	42	290	11	1.7
041SMPL	75	Rim	Elongated	0.04964	0.008	0.31519	0.051	0.04606	0.002	0.038	178	30	278	45	290	12	-4.3
019SMPL	34	Rim	Rounded	0.05531	0.004	0.35279	0.028	0.04625	0.001	0.037	425	34	307	24	291	7	5.0
032SMPL	53	Core	Rounded	0.05178	0.007	0.33083	0.046	0.04635	0.002	0.036	276	39	290	40	292	11	-0.6
046SMPL	87	Rim	Rounded	0.05457	0.011	0.35034	0.070	0.04657	0.002	0.034	395	80	305	61	293	15	3.8
036SMPL	68	Rim	Rounded	0.0516	0.009	0.33171	0.056	0.04664	0.002	0.034	268	46	291	49	294	12	-1.0
044SMPL	86	Rim	Rounded	0.05202	0.014	0.33445	0.090	0.04664	0.003	0.032	286	79	293	79	294	18	-0.3
011SMPL	10	Core	Elongated	0.05713	0.005	0.36944	0.033	0.04689	0.001	0.034	497	45	319	28	295	7	7.5
013SMPL	12	Rim	Elongated	0.0513	0.005	0.33176	0.034	0.0469	0.001	0.035	254	27	291	30	295	8	-1.6
039SMPL	72	Core	Elongated	0.05129	0.009	0.33231	0.058	0.04701	0.002	0.036	254	46	291	51	296	13	-1.7
029SMPL	50	Core	Elongated	0.05143	0.006	0.33538	0.042	0.04731	0.001	0.036	260	32	294	36	298	9	-1.5
021SMPL	43	Core	Rounded	0.05285	0.004	0.34708	0.025	0.04763	0.001	0.040	322	24	303	22	300	6	0.8
031SMPL	53	Rim	Rounded	0.05269	0.013	0.34718	0.082	0.04781	0.002	0.028	315	75	303	71	301	15	0.5
034SMPL	64	Rim	Rounded	0.05274	0.007	0.35277	0.047	0.04853	0.002	0.035	318	43	307	41	305	10	0.4
010SMPL	7	Rim	Elongated	0.05302	0.007	0.35532	0.046	0.0486	0.001	0.032	330	44	309	40	306	9	0.9
Standard data																	
005SMPL	91500	-	-	0.0764	0.003	1.93763	0.084	0.1839	0.003	0.034	1106	50	1094	47	1088	17	0.5
006SMPL	91500	-	-	0.07777	0.003	1.7899	0.072	0.16691	0.003	0.036	1141	46	1042	42	995	16	4.5
025SMPL	Plesovice	-	-	0.05491	0.004	0.40804	0.030	0.05391	0.001	0.036	409	32	347	26	338	7	2.6
026SMPL	Plesovice	-	-	0.05272	0.004	0.39443	0.032	0.05427	0.001	0.040	317	26	338	27	341	8	-0.9

Table 3. Continued.

Age (Ma)	BI40/4			BI50/10			BI40/4 and BI50/10		
	Concordia age (Ma)	MSWD (of concordance)	N	Concordia age (Ma)	MSWD (of concordance)	N	Concordia age (Ma)	MSWD (of concordance)	N
Concordant cores	286.6 ± 4.6 (2σ)	0.05	8	285.4 ± 4.9 (2σ)	0.001	9	286.0 ± 3.0 (95% c. l.*)	0.019	17
Cores, all analyses	286.3 ± 3.7 (2σ)	0.22	13	279.5 ± 4.1 Ma (95% c. l.*)	1.8	16	282.3 ± 2.4 (95% c. l.*)	1.6	29
Concordant rims	285.0 ± 11 (2σ)	0.66	3	292.7 ± 7.5 (2σ)	1.40	6	290.3 ± 7.3 (95% c. l.*)	0.010	9
Rims, all analyses	290.2± 5.9 (2σ)	0.63	8	288.9 ± 4.1 (2σ)	0.001	17	289.4 ± 7.3 (95% c. l.*)	0.25	25
*c.l. = confidence level									

Table 4. U-Pb mean concordia ages, MSWD and number of analyses (N) for: (i) amphibole gabbronorite BI40/4, (ii) amphibole-free gabbronorite BI50/10, and both samples together. “All analyses” implies both concordant and sub-concordant U-Pb zircon analyses.

4.3 Comparison with literature U-Pb zircon data from the Ivrea Mafic Complex

The U-Pb mean concordia ages obtained from zircon cores and rims of gabbronorites BI40/4 and BI50/10 are equivalent within error (Table 4). Taken as a whole, concordant U-Pb core zircon dates from both samples gave a mean concordia age of 286.0 ± 3.0 Ma (95% confidence level, MSWD of concordance = 0.019). Concordant and sub-concordant U-Pb core zircon dates provided a mean concordia age of 282.3 ± 2.4 Ma (2σ, MSWD of concordance = 1.6). These two mean concordia ages are also equivalent within error. The slightly lower average value obtained considering both concordant and sub-concordant U-Pb core zircon dates reflects the presence of a date cluster (Fig. 7c) at ~277 Ma resulting from analyses of the prismatic zircons from gabbronorite BI50/10.

The zircon rims from gabbronorites BI40/4 and BI50/10 most likely represent the product of a zircon recrystallization event. Concordant U-Pb rim zircon dates obtained from both samples yielded a mean concordia age of 290.3 ± 7.3 Ma (95% confidence level, MSWD of concordance = 0.010). Concordant and sub-concordant U-Pb rim zircon dates gave a mean concordia age of 289.4 ± 7.3 Ma (95% confidence level, MSWD of concordance = 0.25). Hence, the U-Pb zircon data do not allow deciphering an age difference between cores and rims. Nevertheless, they indicate that the zircon recrystallization event occurred soon after the magmatic crystallization. The zircon rim age also suggests that the slightly younger age returned from core spot analyses, typically giving sub-concordant dates, of BI50/10 prismatic zircons (276.6 ± 3.7 Ma) is due to a U-Pb isotopic disturbance, such as loss of radiogenic Pb. The age of 286.0 ± 3.0 Ma obtained from concordant spot analyses on zircon cores from both gabbronorites could therefore represent the best age estimate for the crystallization of the gabbronorites enclosing the peridotite-pyroxenite sequence.

Peressini et al. (2007) carried out high-resolution ion microprobe (SHRIMP) analyses on zircons from 12 rocks samples of the Ivrea Mafic Complex. Two of the twelve samples analyzed by Peressini et al. (2007) were collected from gabbronoritic bands within the amphibole gabbro of the Lower Mafic Complex, in the upper Val Sessera. These zircons, labelled 11ag and 12ag, have up to 100 mm thick, inclusion-free, bright rims without zoning in cathodoluminescence. The zircon cores display recurrent values of Th/U>1, compatible with zircons crystallized from a mafic magma. 11ag zircon cores gave nearly concordant U-Pb dates spanning from 265 ± 4 to 287 ± 4 Ma, with a cluster of six spot analyses with relatively high U contents and low percentage of discordance returning a weighted average $^{206}Pb/^{238}U$ age of 281 ± 3 Ma (2σ, MSWD =0.73). The bright-rim zircon domains from gabbronorite 11ag have same Th/U ratio as the cores, but systematically show lower Th and U abundances. The ages resulting from analyses on these domains are not distinguishable from those obtained on other domains, but are inevitably affected by larger analytical errors. Peressini et al. (2007) proposed that the zircon rims were leached of U, Th and Pb by an interstial fluid of late

magmatic origin. Only two of the analyzed spots for 12ag zircons are concordant and define a mean concordia age of 279 ± 5 Ma (2σ, MWSD = 0.53). Peressini et al. (2007) interpreted the relatively young age of samples 11ag and 12ag (~280 Ma), compared to the age of 288 ± 4 Ma obtained from the Upper Mafic Complex, to indicate a cooling front that descended slowly through the crust after the growth of the Mafic Complex. Accordingly, the intrusion of mantle-derived magma at ~288 Ma with the formation of the voluminous Upper Mafic Complex could produce a thermal anomaly large enough (10 Myr) to maintain partially molten rocks in the lower crust.

Fourty-eight new U-Pb isotope analyses were carried out by SHRIMP on core domains of 11ag zircons by Sinigoi et al. (2011). The gabbronorite is notably rich in Zr (700 ppm) but free of inherited zircons, thereby leading Sinigoi et al. (2011) to propose that the 11ag zircons were not directly related to the gabbronorite-forming melt but resulted from assimilation of zircon-rich crustal components. Following this idea, inherited crustal zircons could be completely reset or digested by hot magma undersaturated in zirconium. The analyses carried out on 11ag elongated zircon grains define a peak at ~285 Ma with a shoulder at ~273 Ma. The gabbronorite 11ag also enclose big bright zircons with an age of ~280 Ma, and pink yellow zircons with an age of ~273 Ma. Sinigoi et al. (2011) argued against the interpretation of Peressini et al. (2007) for the growth of the Mafic Complex by an intrusive front advancing upward through the deep crust, which would be expected to result in upwardly youngling intrusive ages, and instead proposed that the deepest levels of the Mafic Complex underwent remelting and recrystallization during growth of the Upper Mafic Complex.

The age of 286.0 ± 3.0 Ma obtained here based on concordant U-Pb core zircon dates from gabbronorites BI40/4 and BI50/10 is not younger than the age of 288 ± 4 Ma proposed by Peressini et al. (2007) for the main magmatic event forming the Upper Mafic Complex. The ~286 Ma age may thus represent the crystallization of the gabbronorites of the Lower Mafic Complex. Alternatively, the ~286 Ma age represents a cooling age, in response to prolonged stay of the Lower Mafic Complex at the solidus transition zone.

Further U-Pb zircon ages have been recently obtained by chemical abrasion isotope dilution thermal ionization mass spectrometry for a variety of rock samples collected from the Sesia valley section (Karakas et al., 2019). These samples include lower- and upper-crustal intrusive rocks and erupted products (the so-called Sesia Magmatic System) and have given ages ranging from 285.52 ± 0.15 Ma to 281.58 ± 0.44 Ma (2σ uncertainty). The laser ablation ICP-MS investigations carried out in the present study gave low precision ages compared to the isotope dilution TIMS ages reported by Karakas et al. (2019). Nevertheless, the age of 286.0 ± 3.0 Ma obtained from gabbronorites BI40/4 and BI50/10 may be reconciled with the peak of magma accretion proposed for the Sesia Magmatic System.

5 Whole-rock chemical compositions

The Mg# [molar Mg/(Mg+Fe^{2+}_{tot}) × 100] decreases from the peridotites (84-90) to the plagioclase pyroxenites (82-84). Al_2O_3 shows a rough negative correlation with Mg# and increases from 1.4 wt% to 4.9 wt% in peridotites and from 5.1 wt% to 6.3 wt% in plagioclase-pyroxenites (Fig. 8). CaO is below 5.5 wt% in peridotites and pyroxenites. The thin gabbronorite dykes BI2/5 and BI10/3 (see Antonicelli et al., 2020) have higher Mg# than the thick dykes. Enclosing gabbronorites show lower and more variable Mg# than the gabbronorite dykes (37-56). Taken as a whole, the gabbronorites have high Al_2O_3 contents and CaO exhibits a rough positive correlation with Mg#, decreasing from 15.9 wt% to 12.7 wt% in gabbronorite dykes and from 11.1 wt% to 7.6 wt% in enclosing gabbronorites. Al_2O_3 and CaO compositions are mostly controlled by the high modal proportions of plagioclase and clinopyroxene, respectively (Table 1). Enclosing gabbronorite BI40/4 exhibits lower SiO_2 and higher TiO_2 than the other gabbronorites, in agreement with the high amphibole proportion. Detailed description of major element whole-rock compositions of peridotites and gabbronorite dykes from the Rocca d'Argimonia sequence are reported in Antonicelli et al. (2020).

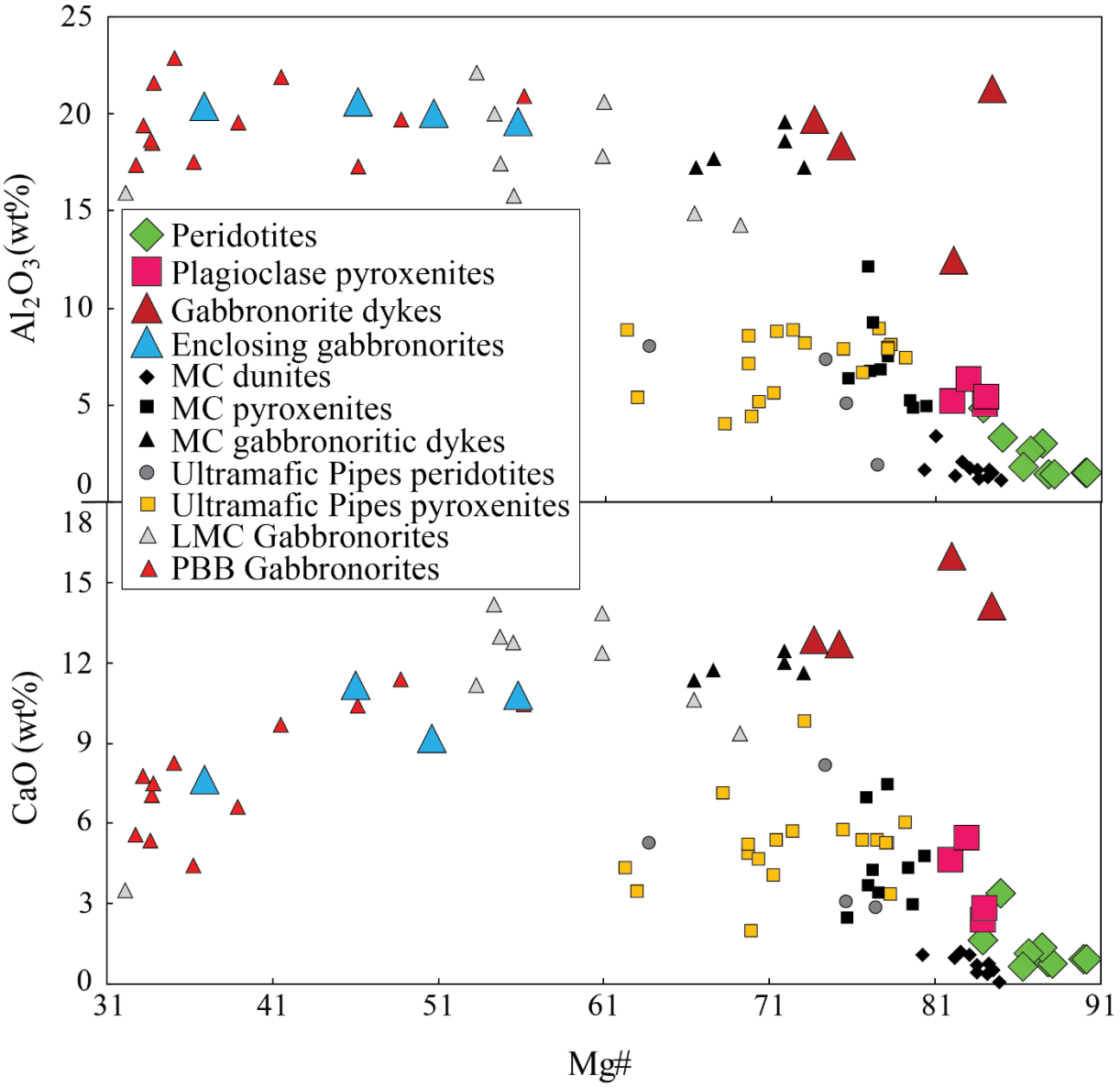

Fig. 8. Diagrams showing the whole-rock chemical compositions of the selected samples from the Rocca d'Argimonia sequence. Al_2O_3 and CaO, calculated on anhydrous basis, versus Mg# [molarMg/(Mg+Fe^{2+}_{tot}) × 100]. Whole-rock compositions of samples from the Rocca d'Argimonia sequence are compared with other rocks from the Ivrea Mafic Complex. Dunites, pyroxenites and gabbronoritic dykes from Monte Capio (MC) ultramafic sequence after Denyszyn et al. (2018) and Berno et al. (2020). Peridotites and pyroxenites from the Ultramafic Pipes after Denyszyn et al. (2018) and Garuti et al. (2001), respectively. Gabbronoritic rocks from the Lower Mafic Complex (LMC) and from the paragneiss-bearing belt (PBB) from Val Sessera after Sinigoi et al. (2011).

Rock type	Dunites					Harzburgites		Lherzolites		Pyroxenites				Gabbronorite dykes				Gabbronorites			
Sample	BI4/3	BI4/1	BI10/3	BI10/1	BI5/1	BI2/1	BI2/7	BI6/2	BI30/5	BI1/1	BI9/2	BI30/7	BI50/8	BI2/5	BI10/3	BI8/1	BI50/3	BI23/2	BI23/5	BI40/4	BI50/10
SiO_2	38.2	38.4	39.3	39.2	37.1	39.5	40.1	43.5	44.7	52.0	51.5	50.4	51.2	45.9	47.8	49.1	47.0	47.89	51.39	44.62	54.08
Al_2O_3	1.48	1.51	1.39	1.40	3.00	2.66	1.75	3.30	4.86	5.2	6.3	5.1	5.3	21.3	12.5	18.4	19.3	19.61	19.94	20.43	20.25
Fe_2O_3 (tot)	10.4	10.5	12.1	12.7	12.4	13.0	13.3	12.5	13.0	11.0	10.1	10.8	10.6	4.04	6.69	6.50	7.27	9.48	9.19	13.19	9.11
MnO	0.14	0.14	0.16	0.16	0.15	0.17	0.17	0.17	0.18	0.2	0.2	0.2	0.2	0.07	0.13	0.12	0.13	0.16	0.17	0.19	0.14
MgO	47.5	47.5	45.3	45.8	43.2	42.6	42.2	35.6	34.0	25.1	24.8	28.5	28.0	11.0	15.4	10.0	10.3	6.01	4.76	5.67	2.68
CaO	0.92	0.96	0.75	0.82	1.38	1.17	0.63	3.42	1.67	4.6	5.5	2.4	2.8	14.1	16.0	12.7	12.6	10.75	9.24	10.99	7.58
Na_2O	0.05	0.05	0.04	0.04	0.06	0.06	0.04	0.13	0.10	0.2	0.3	0.1	0.2	1.27	0.68	1.57	1.61	2.71	3.41	2.49	3.99
K_2O	<0.01	<0.01	<0.01	<0.01	<0.01	<0.01	<0.01	<0.01	<0.01	<0.01	<0.01	<0.01	0.0	0.06	0.05	0.13	0.12	0.35	0.37	0.36	0.71
TiO_2	0.05	0.05	0.04	0.05	0.09	0.10	0.05	0.17	0.19	0.3	0.3	0.3	0.3	0.33	0.43	0.40	0.39	1.04	1.14	1.73	1.18
Cr_2O_3	0.64	0.65	0.59	0.52	1.27	0.88	0.92	0.41	0.70	0.4	0.5	0.5	0.6	0.02	0.10	0.02	0.01	0.01	0.00	<0.003	<0.003
NiO	0.31	0.31	0.27	0.28	0.34	0.24	0.23	0.16	0.18	0.1	0.1	0.1	0.1	0.08	0.08	0.03	0.02	0.01	0.01	<0.003	<0.003
P_2O_5	0.01	<0.01	<0.01	<0.01	<0.01	0.01	0.01	<0.01	0.02	<0.01	<0.01	<0.01	0.0	<0.01	<0.01	<0.01	<0.01	0.19	0.23	0.35	0.34
LOI	<0.01	0.20	0.11	<0.01	1.12	0.05	0.46	0.83	0.52	0.7	0.8	0.5	0.8	1.80	0.92	0.95	2.03	0.94	0.25	0.64	0.31
Total	99.7	100.2	100.0	100.9	100.0	100.4	99.8	100.1	100.1	99.8	100.4	98.9	100.1	100.0	100.7	99.8	100.8	99.14	100.10	100.66	100.37
Mg#	90.1	90.0	88.1	87.8	87.4	86.7	86.3	84.9	83.8	81.9	82.9	83.9	84.0	84.4	82.0	75.2	73.7	55.7	50.6	46.0	36.8

Table 5. Whole-rock major element compositions of selected samples.

The peridotites have high Ni and Cr concentrations, which progressively decrease from the dunites to the harzburgites, the lherzolites and the plagioclase pyroxenites (Ni = 2580-610 ppm; Cr = 7700-2830 ppm). High Cr amounts are likely related to relatively high proportions of spinel in the peridotites (see also Antonicelli et al., 2020). Ni and Cr amounts in the gabbronorite dykes and the enclosing gabbronorites are negligible. Thin gabbronorite dyke samples have anomalously high Ni and Cr values, which most likely reflects a role of host dunites–harzburgites, in response to local dissolution and assimilation of peridotite material by the migrating melt (see Antonicelli et al., 2020).

REE concentrations of whole-rock peridotite samples are low. Chondrite-normalized REE patterns are characterized by nearly flat middle REE (MREE) and heavy REE (HREE) and no evident Eu anomaly. Light REE (LREE) are slightly depleted to slightly enriched with respect to MREE-HREE (Fig. 9, Table 6). Whole-rock REE compositions of plagioclase-bearing pyroxenites are slightly higher than that of peridotites, and display nearly homogeneous chondrite-normalized patterns. The samples exhibit slight LREE depletion, no evident Eu anomaly and nearly flat to slightly enriched MREE-HREE. The hornblende gabbronorite dykes have nearly flat REE patterns and positive Eu anomaly. The gabbronorites enclosing the peridotite-pyroxenite sequence have high REE concentrations, with patterns broadly characterized by LREE enrichment over MREE and HREE. Gabbronorites BI23/2 and BI40/4 show nearly flat to moderately enriched LREE and no or weak negative Eu anomaly, whereas gabbronorites BI23/5 and BI50/10 display a LREE enrichment over MREE and weak positive Eu anomaly.

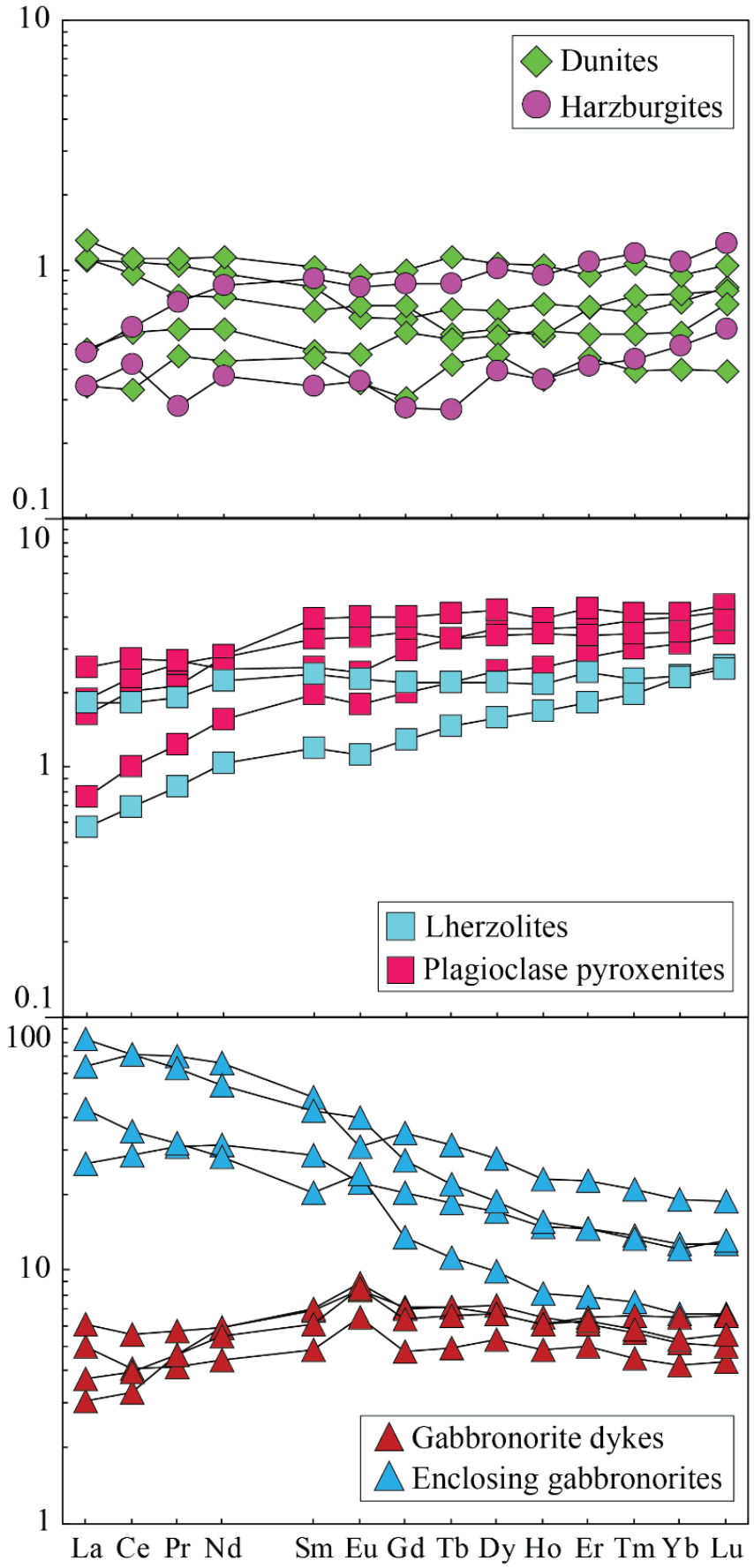

Fig. 9. Whole-rock REE compositions normalized to CI chondrite (Sun and McDonough, 1989).

Rock type	Dunites					Harzburgites		Lherzolites		Pyroxenites				Gabbronorite dykes				Gabbronorites			
Sample	BI4/3	BI4/1*	BI10/3	BI10/1*	BI5/1*	BI2/1*	BI2/7	BI6/2	BI30/5*	BI1/1	BI9/2	BI30/7	BI50/8	BI2/5	BI10/3	BI8/1	BI50/3	BI23/2	BI23/5	BI40/4	BI50/10
Sc	8	7.43	6	6.45	9.13	9.62	8	23	20.0	39	42	33	30	33	57	35	40	37	24	40	23
V	35	43.8	36	34.1	70.6	64.4	52	100	129	186	199	164	161	193	308	226	229	232	204	330	144
Cr	4370	4752	4020	3489	7665	5841	6275	2830	4755	2970	3480	3440	3880	110	690	110	80	50	30	<20	<20
Co	132	142	140	136	123	131	134	111	104	77	72	73	74	38	41	36	36	27	22	30	16
Ni	2450	2581	2095	2207	2548	1874	1840	1260	1463	630	680	630	610	620	630	220	140	<20	<20	<20	<20
Cu	30	26	40	47	104	42	70	180	40	90	120	90	50	300	180	90	60	30	<10	20	10
Zn	60	73.6	70	97.6	94.9	91.3	100	80	107	70	70	70	90	40	30	<30	<30	90	90	110	120
Ga	3	2.84	2.5	2.32	4.66	4.66	4	5	7.19	7	8	7	8	13	10	15	13	21	22	22	24
Ge	0.9	1.04	1	0.98	0.945	1.04	1.2	1	1.31	1.5	1.8	1.3	1.5	1	1.4	1.3	1	1.2	1.1	1.3	1.2
Rb	<1	0.162	<1	0.050	0.162	0.072	<1	<1	0.121	<1	<1	<1	<1	1	1	4	3	<1	<1	<1	2
Sr	4	3.92	4	3.13	5.39	3.79	2.5	7	5.34	12	27	4	14	410	135	424	319	398	496	373	393
Y	0.9	0.956	0.6	0.785	1.46	1.37	0.55	3.2	2.47	5.3	6.2	3.7	4.6	6.9	8.8	9.2	8.3	21.4	11.7	33.6	23.1
Zr	3	2.21	3	1.28	2.44	3.09	2.5	5	4.95	12	12	7	12	8	9	14	13	36	36	92	330
Nb	<0.2	0.075	<0.2	0.046	0.104	0.0730	<0.2	<0.2	0.080	<0.2	<0.2	<0.2	0.2	<0.2	<0.2	<0.2	<0.2	1.6	4.4	10.9	14.7
Cs	<0.1	0.005	<0.1	0.002	0.013	0.005	<0.1	<0.1	0.003	0.3	<0.1	<0.1	<0.1	<0.1	<0.1	0.1	<0.1	0.8	0.3	0.7	0.9
Ba	<2	1.79	4	0.97	1.77	1.40	4.5	<2	2.15	6	2	<2	10	21	10	47	37	130	172	97	512
La	0.26	0.2569	0.08	0.112	0.306	0.109	0.08	0.43	0.135	0.38	0.44	0.18	0.59	1.17	0.71	1.43	0.87	6.23	10.1	14.9	19.3
Ce	0.58	0.650	0.2	0.339	0.664	0.355	0.25	1.09	0.422	1.23	1.38	0.61	1.64	2.47	1.98	3.38	2.39	17.2	21.5	42.7	42.7
Pr	0.07	0.093	0.04	0.051	0.099	0.065	0.025	0.17	0.075	0.19	0.23	0.11	0.24	0.37	0.41	0.51	0.41	2.74	2.84	6.28	5.63
Nd	0.35	0.437	0.195	0.261	0.505	0.392	0.17	1.01	0.472	1.25	1.28	0.7	1.13	1.99	2.67	2.68	2.48	14.2	12.6	29.7	24.5
Sm	0.1	0.125	0.065	0.070	0.152	0.135	0.05	0.35	0.177	0.48	0.58	0.29	0.37	0.71	1.02	1.04	0.9	4.2	2.99	7.15	6.29
Eu	0.04	0.036	0.0195	0.026	0.053	0.048	0.02	0.127	0.063	0.186	0.225	0.1	0.134	0.366	0.466	0.495	0.478	1.25	1.35	1.73	2.23
Gd	0.14	0.125	0.06	0.110	0.197	0.172	0.055	0.43	0.255	0.69	0.79	0.39	0.58	0.94	1.41	1.39	1.27	3.98	2.64	6.85	5.33
Tb	0.02	0.025	0.015	0.019	0.041	0.032	0.01	0.08	0.053	0.12	0.15	0.08	0.12	0.18	0.26	0.26	0.24	0.67	0.41	1.13	0.79
Dy	0.14	0.166	0.11	0.131	0.256	0.244	0.095	0.53	0.385	0.88	1.03	0.59	0.82	1.29	1.75	1.64	1.64	4.12	2.42	6.66	4.56
Ho	0.03	0.040	0.02	0.031	0.057	0.053	0.02	0.12	0.093	0.2	0.22	0.14	0.19	0.27	0.36	0.34	0.34	0.83	0.45	1.27	0.86
Er	0.11	0.113	0.07	0.088	0.151	0.171	0.065	0.38	0.289	0.58	0.69	0.44	0.54	0.8	0.97	1.03	1	2.32	1.25	3.59	2.33
Tm	0.019	0.016	0.0095	0.013	0.026	0.028	0.0105	0.055	0.047	0.094	0.1	0.072	0.083	0.109	0.137	0.161	0.141	0.33	0.18	0.508	0.322
Yb	0.13	0.120	0.065	0.091	0.153	0.174	0.08	0.38	0.375	0.65	0.67	0.51	0.57	0.68	0.84	1.05	0.87	2.06	1.09	3.09	1.96
Lu	0.02	0.021	0.0095	0.018	0.025	0.031	0.014	0.062	0.061	0.102	0.108	0.084	0.094	0.106	0.122	0.16	0.135	0.31	0.162	0.457	0.319
Hf	<0.1	0.067	<0.1	0.039	0.089	0.111	<0.1	0.2	0.198	0.3	0.4	0.2	0.4	0.3	0.4	0.5	0.4	1.3	1.1	2.4	8.1
Ta	<0.01	0.046	<0.01	0.029	0.060	0.048	<0.01	<0.01	0.030	<0.01	0.03	<0.01	0.02	0.02	<0.01	0.01	<0.01	0.07	0.24	0.59	0.61
Pb	<5	0.478	<5	1.422	1.561	1.997	<5	<5	0.432	<5	<5	<5	<5	8	<5	<5	<5	<5	<5	<5	6
Th	<0.05	0.056	<0.05	0.007	0.081	0.012	<0.05	0.07	0.018	<0.05	<0.05	<0.05	0.06	0.12	<0.05	0.14	<0.05	0.05	<0.05	<0.05	0.1
U	<0.01	0.011	0.01	0.002	0.021	0.005	<0.01	0.02	0.007	0.01	0.02	<0.01	0.01	0.03	0.01	0.04	0.01	0.02	<0.01	0.03	0.32

Table 6. Whole-rock trace element compositions of selected samples. (*) = analyses performed at the Institute of Geology and Geophysics, Chinese Academy of Sciences, Beijing.

6 Nd-Sr-Hf isotopic compositions

According to U–Pb zircon age determinations from the present study, initial Nd-Sr-Hf isotopic compositions were calculated at 286 Ma.

6.1 Nd isotopic compositions

Peridotites and pyroxenites display similar $\varepsilon_{Nd(286\ Ma)}$ values. In particular, $\varepsilon_{Nd(286\ Ma)}$ ranges from +0.4 to -1.1 for the peridotites and from +1.6 to -1.2 for the pyroxenites. Dunite BI4/1 and BI10/1 notably show significant discrepancies in initial Nd isotopic compositions between whole-rock and mineral separates, with the latter showing a slightly more depleted Nd isotopic signature compared to the whole-rock. The $\varepsilon_{Nd(286\ Ma)}$ of hornblende gabbronorite dykes ranges from -0.8 to -2.5, with the lowest value pertaining to the thin gabbronorite dyke BI10/3. The initial ε_{Nd} compositions of enclosing gabbronorites range from -4.5 to -5.6.

6.2 Sr isotopic compositions

The initial $^{87}Sr/^{86}Sr$ whole-rock compositions are similar in the peridotites and the pyroxenites, and ranges from 0.7060 to 0.7048 (Fig. 10, Table 7). The mineral separates from dunites BI4/1 and BI10/1 have slightly lower $^{87}Sr/^{86}Sr_{(286\ Ma)}$ than the whole-rock. The $^{87}Sr/^{86}Sr_{(286)}$ ratio of hornblende gabbronorite dykes and enclosing gabbronorites range from 0.7057 to 0.7066 and from 0.7073 to 0.7086, respectively.

6.3 Hf isotopic compositions

Whole-rock and mineral separates $\varepsilon_{Hf(286\ Ma)}$ values range from +8.8 to +3.3, from dunites to harzburgites to lherzolites (Fig. 10, Table 7). For the dunites BI4/1 and BI10/1, the mineral separates show higher $\varepsilon_{Hf(286\ Ma)}$ than the whole-rock. The $\varepsilon_{Hf(286\ Ma)}$ whole-rock values of pyroxenites range from +7.1 to +3.2 and fall within the range of the peridotite. The hornblende gabbronorite dykes and enclosing gabbronorites have $\varepsilon_{Hf(286\ Ma)}$ ranging from +4.9 to +3.0 and from +0.2 to -2.5.

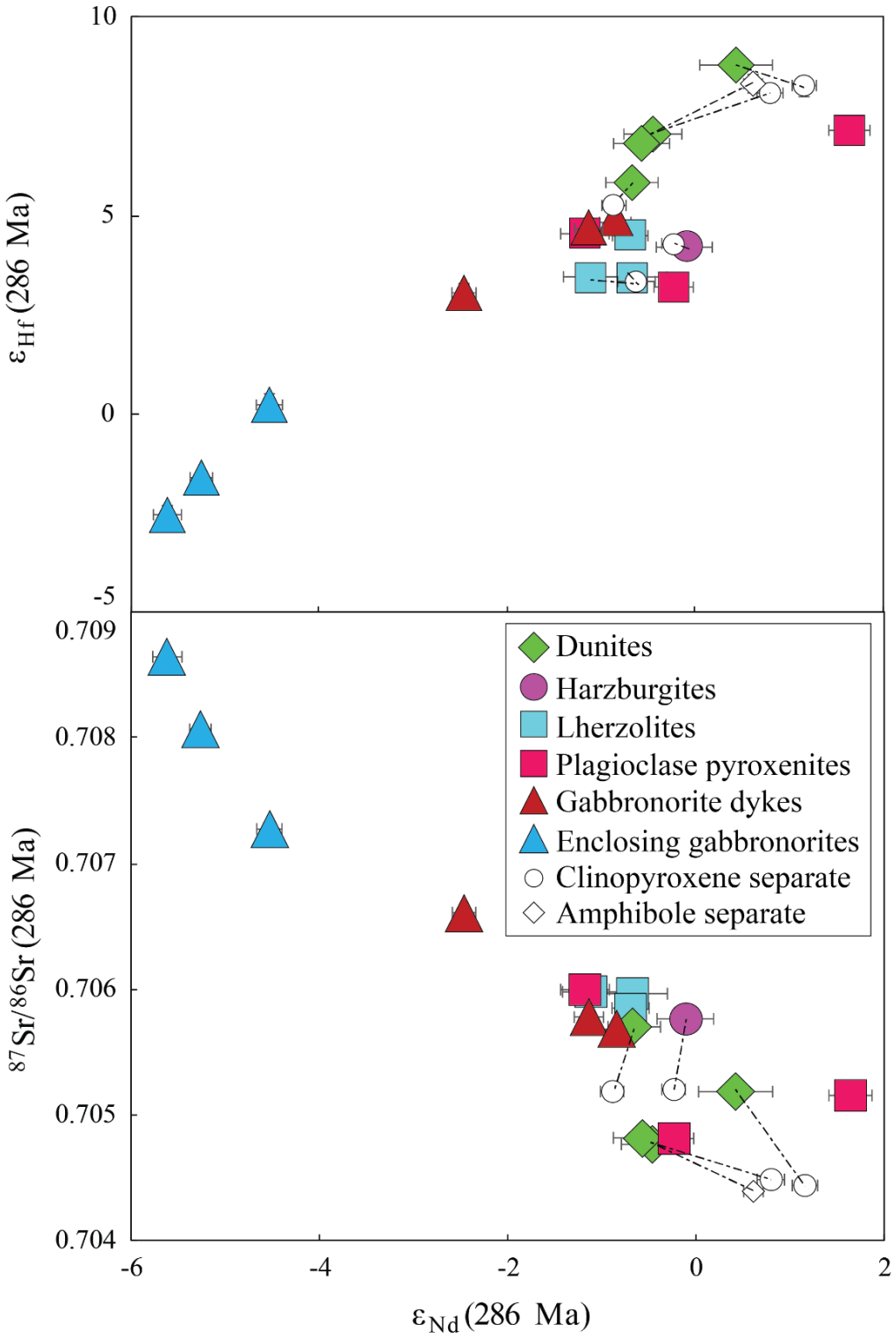

Fig. 10. Plot of initial ε_{Hf} and initial $^{87}Sr/^{86}Sr$ versus initial ε_{Nd} of the selected samples from the Rocca d'Argimonia sequence. The compositions of clinopyroxene and amphibole separates from peridotites are also reported; the dotted tie lines refer to peridotite and related mineral separate(s). The error bars represent the calculated error per each analysis (1σ).

	Dunites								Harzburgites		Lherzolites				
	BI4/1	BI4/1	BI4/1	BI4/1	BI10/1	BI10/1	BI5/1	BI5/1	BI2/1	BI2/1	BI6/2	BI30/5	BI30/5	BI30/5	BI30/5
	W.R.	W.R. (*replicate*)	Amp	Cpx	W.R.	Cpx	W.R.	Cpx	W.R.	Cpx	W.R.	W.R.	W.R. (*replicate*)	Amp-Cpx mix	Cpx
Sm ppm	0.107	0.108	3.320	1.752	0.080	1.876	0.164	1.739	0.132	1.995	0.326	0.173	0.174	-	1.876
Nd ppm	0.377	0.379	10.91	5.693	0.257	5.140	0.500	5.358	0.366	5.542	0.919	0.445	0.448	-	4.803
$^{147}Sm/^{144}Nd$	0.172279	0.172327	0.184069	0.186049	0.187544	0.220640	0.198683	0.196259	0.217586	0.217581	0.214518	0.234603	0.234801	-	0.236149
$^{143}Nd/^{144}Nd$	0.512563	0.512569	0.512646	0.512659	0.512643	0.512742	0.512607	0.512592	0.512672	0.512665	0.512636	0.512652	0.512675	-	0.512680
2se	1.6E-05	1.6E-05	5.2E-06	7.2E-06	2.0E-05	6.8E-06	1.5E-05	6.4E-06	1.5E-05	6.7E-06	1.0E-05	1.5E-05	1.9E-05	-	1.0E-05
$^{143}Nd/^{144}Nd$ i	0.512240	0.512247	0.512302	0.512310	0.512292	0.512329	0.512235	0.512225	0.512265	0.512258	0.512234	0.512213	0.512236	-	0.512238
ε_{Nd} i	-0.6	-0.5	0.6	0.8	0.4	1.2	-0.7	-0.9	-0.1	-0.2	-0.7	-1.1	-0.7	-	-0.6
Calculated 1σ (ε_{Nd} i)	0.3	0.3	0.1	0.1	0.4	0.1	0.3	0.1	0.3	0.1	0.2	0.3	0.4	-	0.2
Rb ppm	0.135	0.147	10.138	0.049	0.048	0.039	0.192	0.069	0.072	0.058	0.170	0.146	0.148		0.056
Sr ppm	4.060	4.061	183.2	48.85	3.556	27.59	6.136	33.53	4.202	27.95	7.745	7.059	6.007		29.731
$^{87}Rb/^{86}Sr$	0.096453	0.104588	0.160048	0.002926	0.039011	0.004101	0.090491	0.005940	0.049839	0.006003	0.064718	0.059740	0.071132	-	0.005426
$^{87}Sr/^{86}Sr$	0.705205	0.705191	0.705047	0.704498	0.705342	0.704450	0.706065	0.705203	0.705972	0.705233	0.706096	0.706229	0.706256	0.705451	-
2se	1.4E-05	1.2E-05	1.4E-05	1.1E-05	1.3E-05	1.3E-05	1.2E-05	1.1E-05	1.3E-05	1.3E-05	1.2E-05	1.3E-05	1.2E-05	1.3E-05	-
$^{87}Sr/^{86}Sr$ i	0.704812	0.704765	0.704396	0.704486	0.705183	0.704433	0.705697	0.705179	0.705769	0.705209	0.705833	0.705986	0.705967	-	-
Calculated 1σ ($^{87}Sr/^{86}Sr$ i)	1.4E-05	1.2E-05	1.4E-05	1.1E-05	1.3E-05	1.3E-05	1.2E-05	1.1E-05	1.3E-05	1.3E-05	1.2E-05	1.3E-05	1.2E-05	-	-
Lu ppm	0.018	0.018	0.682	0.245	0.017	0.238	0.025	0.237	0.029	0.272	0.060	0.058	0.057	0.323	0.248
Hf ppm	0.061	0.061	1.630	1.133	0.043	1.212	0.084	1.147	0.102	1.685	0.234	0.186	0.186	1.877	1.734
$^{176}Lu/^{177}Hf$	0.041451	0.041233	0.059442	0.030737	0.056945	0.027918	0.041787	0.029331	0.040716	0.022948	0.036326	0.043962	0.043943	0.024434	0.020301
$^{176}Hf/^{177}Hf$	0.283007	0.283014	0.283146	0.282987	0.283147	0.282977	0.282982	0.282899	0.282931	0.282837	0.282915	0.282925	0.282925	0.282824	0.282796
2se	5.0E-06	6.1E-06	6.9E-06	6.7E-06	5.6E-06	6.7E-06	5.4E-06	6.6E-06	6.0E-06	6.0E-06	7.7E-06	6.1E-06	5.5E-06	6.5E-06	3.5E-06
$^{176}Hf/^{177}Hf$ i	0.282786	0.282794	0.282829	0.282823	0.282843	0.282828	0.282759	0.282742	0.282714	0.282714	0.282721	0.282691	0.282691	0.282694	0.282688
ε_{Hf} i	6.8	7.1	8.3	8.1	8.8	8.3	5.9	5.2	4.2	4.3	4.5	3.4	3.4	3.5	3.3
Calculated 1σ (ε_{Hf} i)	0.2	0.2	0.2	0.2	0.2	0.2	0.2	0.2	0.2	0.2	0.3	0.2	0.2	0.2	0.1

Table 7. Sm-Nd, Rb-Sr and Lu-Hf isotope results of whole-rock and mineral separates for selected samples from Rocca d'Argimonia sequence. Initial isotopic compositions were carried out at 286 Ma. Mineral abbreviations are after Whitney and Evans (2010); W.R. = whole-rock.

	Pyroxenites			Gabbronorite dykes			Gabbronorites		
	BI9/2	BI30/7	BI50/8	BI10/3	BI8/1	BI50/3	BI23/2	BI40/4	BI50/10
	W.R.	W.R.	W.R.	W.R.	W.R.	W.R.	W.R.	W.R.	W.R.
Sm ppm	0.553	0.266	0.401	1.030	0.907	0.900	3.703	6.467	5.415
Nd ppm	1.436	0.663	1.218	2.524	2.574	2.423	13.29	27.11	24.01
$^{147}Sm/^{144}Nd$	0.232795	0.242718	0.198764	0.246774	0.213023	0.224614	0.168413	0.144197	0.136318
$^{143}Nd/^{144}Nd$	0.512789	0.512664	0.512630	0.512606	0.512625	0.512632	0.512353	0.512270	0.512238
2se	1.1E-05	1.3E-05	1.1E-05	6.6E-06	8.6E-06	7.8E-06	7.0E-06	6.2E-06	7.8E-06
$^{143}Nd/^{144}Nd$ i	0.512354	0.512209	0.512258	0.512144	0.512226	0.512212	0.512038	0.512000	0.511982
ε_{Nd} i	1.6	-1.2	-0.2	-2.5	-0.8	-1.1	-4.5	-5.3	-5.6
Calculated 1σ (ε_{Nd} i)	0.2	0.3	0.2	0.1	0.2	0.2	0.1	0.1	0.2
Rb ppm	0.453	0.374	0.501	1.711	3.972	2.892	0.823	0.512	1.865
Sr ppm	27.64	6.418	10.45	140.17	397.3	335.9	414.4	363.6	399.3
$^{87}Rb/^{86}Sr$	0.047374	0.168372	0.138736	0.035307	0.028920	0.024905	0.005748	0.004073	0.013518
$^{87}Sr/^{86}Sr$	0.705352	0.70668	0.705375	0.706748	0.705796	0.705875	0.707291	0.708084	0.708705
2se	1.3E-05	1.3E-05	1.2E-05	1.2E-05	1.3E-05	1.3E-05	1.2E-05	1.1E-05	1.1E-05
$^{87}Sr/^{86}Sr$ i	0.705159	0.705995	0.704810	0.706604	0.705678	0.705774	0.707268	0.708067	0.708650
Calculated 1σ ($^{87}Sr/^{86}Sr$ i)	1.3E-05	1.3E-05	1.2E-05	1.2E-05	1.3E-05	1.3E-05	1.2E-05	1.1E-05	1.1E-05
Lu ppm	0.109	0.087	0.096	0.114	0.150	0.135	0.281	0.469	0.257
Hf ppm	0.426	0.276	0.393	0.498	0.596	0.482	1.395	2.359	1.958
$^{176}Lu/^{177}Hf$	0.036194	0.044931	0.034901	0.032540	0.035771	0.039588	0.028635	0.028253	0.018679
$^{176}Hf/^{177}Hf$	0.282989	0.282923	0.282910	0.282853	0.282924	0.282938	0.282753	0.282700	0.282622
2se	6.8E-06	5.4E-06	6.4E-06	6.9E-06	5.9E-06	5.1E-06	8.2E-06	4.4E-06	7.0E-06
$^{176}Hf/^{177}Hf$ i	0.282796	0.282684	0.282723	0.282679	0.282733	0.282727	0.282600	0.282549	0.282522
ε_{Hf} i	7.1	3.2	4.6	3.0	4.9	4.7	0.2	-1.6	-2.5
Calculated 1σ (ε_{Hf} i)	0.2	0.2	0.2	0.2	0.2	0.2	0.3	0.2	0.2

Table 7. Continued.

7 Discussion

7.1 Comparison with other mafic-ultramafic sequences from the Ivrea Mafic Complex

7.1.1 Balmuccia mantle body

The Balmuccia massif is a subcontinental mantle peridotite body enclosed within the Ivrea Mafic Complex (Quick et al., 1995). The Balmuccia massif shows an igneous contact at its eastern margin and a tectonic one at its western margin, where metasedimentary septa of the paragneiss-bearing belt are also exposed (Mazzucchelli et al., 2009). The dominant peridotite type is lherzolite. The lherzolites are widely crosscut by two series of websterite dykes, an older Cr-diopside suite and a later Al-augite suite. Locally, the Balmuccia massif includes dunite bodies formed by focused reactive flow of olivine-saturated melts into lherzolites.

These mantle replacive dunites are compositionally distinct from the peridotites of the Rocca d'Argimonia sequence (Antonicelli et al., 2020). For instance, the Balmuccia replacive dunites have forsterite-richer olivine and Cr-richer spinel than the Rocca d'Argimonia dunites (Fig. 12). The Nd-Sr whole-rock isotopic compositions of Balmuccia rocks (Voshage et al., 1990) overall reveal a more depleted isotopic signature compared to the Rocca d'Argimonia rocks, as shown in Fig. 11, where the Balmucccia Nd-Sr isotopic compositions were calculated at 286 Ma. In particular, $\varepsilon_{Nd(286\ Ma)}$ and $^{87}Sr/^{86}Sr_{(286\ Ma)}$ decrease and increase from the Balmuccia peridotites (three lherzolites and one dunite) to the included websterite veins and gabbroic pods. Similar relationships are observed based on clinopyroxene separates (Shervais and Mukasa, 1991; Mukasa and Shervais, 1999). Consistently, the clinopyroxenes from the Rocca d'Argimonia peridotites are isotopically enriched with respect to clinopyroxenes from the Balmuccia mantle massif. Notably, the only isotopic analysis reported in the literature for the Balmuccia replacive dunites ($\varepsilon_{Nd(286\ Ma)} = +2.9$, $^{87}Sr/^{86}Sr_{(286\ Ma)} = 0.7041$; Voshage et al., 1988) shows a distinct Nd-Sr fingerprint with respect to the Rocca d'Argimonia dunites, which in turn have $\varepsilon_{Nd(286\ Ma)}$ of -0.7 to +0.4 and $^{87}Sr/^{86}Sr_{(286\ Ma)}$ of 0.7048 to 0.7057. No isotopic inheritance from the Balmuccia mantle body is therefore retained by the Rocca d'Argimonia peridotite-pyroxenite sequence.

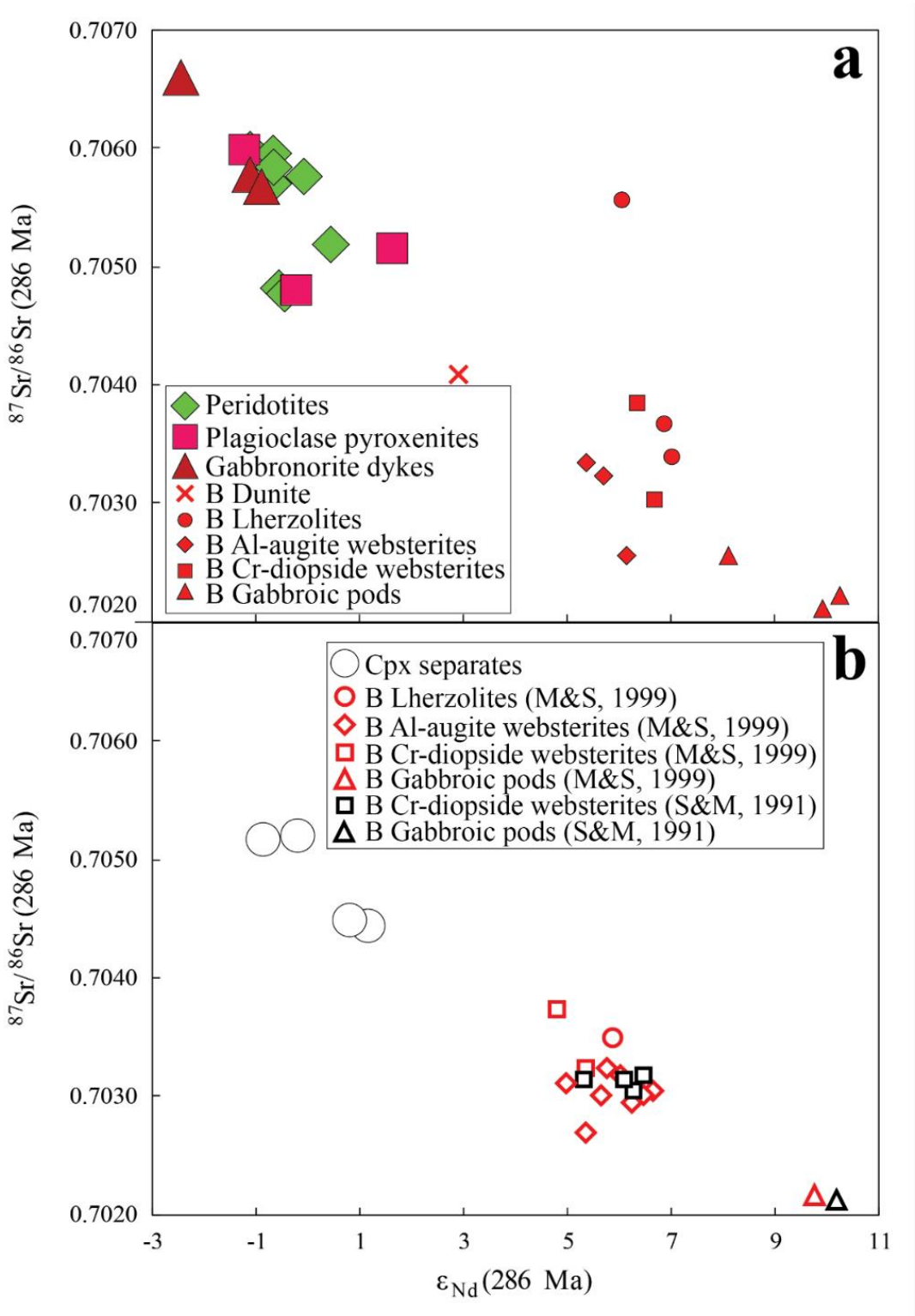

Fig. 11. Plot of initial $^{87}Sr/^{86}Sr$ versus initial ε_{Nd} of the selected samples from the Rocca d'Argimonia sequence. (a) Whole-rock compositions of Balmuccia (B) mantle body calculated at 286 Ma are reported for comparison. Dunite, lherzolites, Al-augite websterites, Cr-diopside websterites and gabbroic pods after Voshage et al. (1988). (b) Clinopyroxene separates compositions of Balmuccia mantle body are reported for comparison. Lherzolites, Al-augite websterites, Cr-diopside websterites and gabbroic pods after Mukasa and Shervais (1999). Cr-diopside websterites and gabbroic pods after Shervais and Mukasa (1991).

7.1.2 Monte Capio magmatic sequence

The Monte Capio sequence is a sill-like mafic-ultramafic sequence (up to 2.5 km in length and ~0.3 km thick) that is exposed along the northern edge of the Ivrea Mafic Complex, near the Insubric Line. The sequence is at least partially embedded into metasediments of the Kinzigite Formation (Denyszyn et al., 2018; Berno et al., 2020). Both Monte Capio and Rocca d'Argimonia sequences mainly consist of dunites, harzburgites and orthopyroxene-rich pyroxenites. The Monte Capio sequence characteristically includes Ni-Cu-PGE sulfide mineralizations (Garuti et al., 1986; Denyszyn et al., 2018).

The Monte Capio ultramafic rocks are typically relatively rich in amphibole, mostly 5 to 10 vol% (Berno et al., 2020). Conversely, amphibole in the Rocca d'Argimonia ultramafic rocks is an accessory phase (1-2 vol%; Antonicelli et al., 2020). In addition, the gabbroic dykes cross-cutting Monte Capio sequence are characterized by extremely high amounts of amphibole (80-90 vol% in hornblende-rich gabbros, 45-55 vol% in hornblende gabbronorites; Berno et al., 2020), whereas the amphibole amount in the gabbronoritic dykes crosscutting Rocca d'Argimonia peridotites varies from 6 to 14 vol% (Antonicelli et al., 2020). The high modal proportions of amphibole in the Monte Capio sequence suggest the involvement of H_2O-richer melts in its formation compared to the melts developing the Rocca d'Argimonia sequence.

The peridotites and the pyroxenites from Monte Capio sequence show lower Mg# than the Rocca d'Argimonia counterparts (Fig. 8). The overall chemically evolved signature of the Monte Capio sequence is confirmed by the relatively low amount of forsterite observed for the olivine (Fig. 12). Conversely, spinel from the peridotites of Monte Capio and Rocca d'Argimonia sequences has similar Cr#.

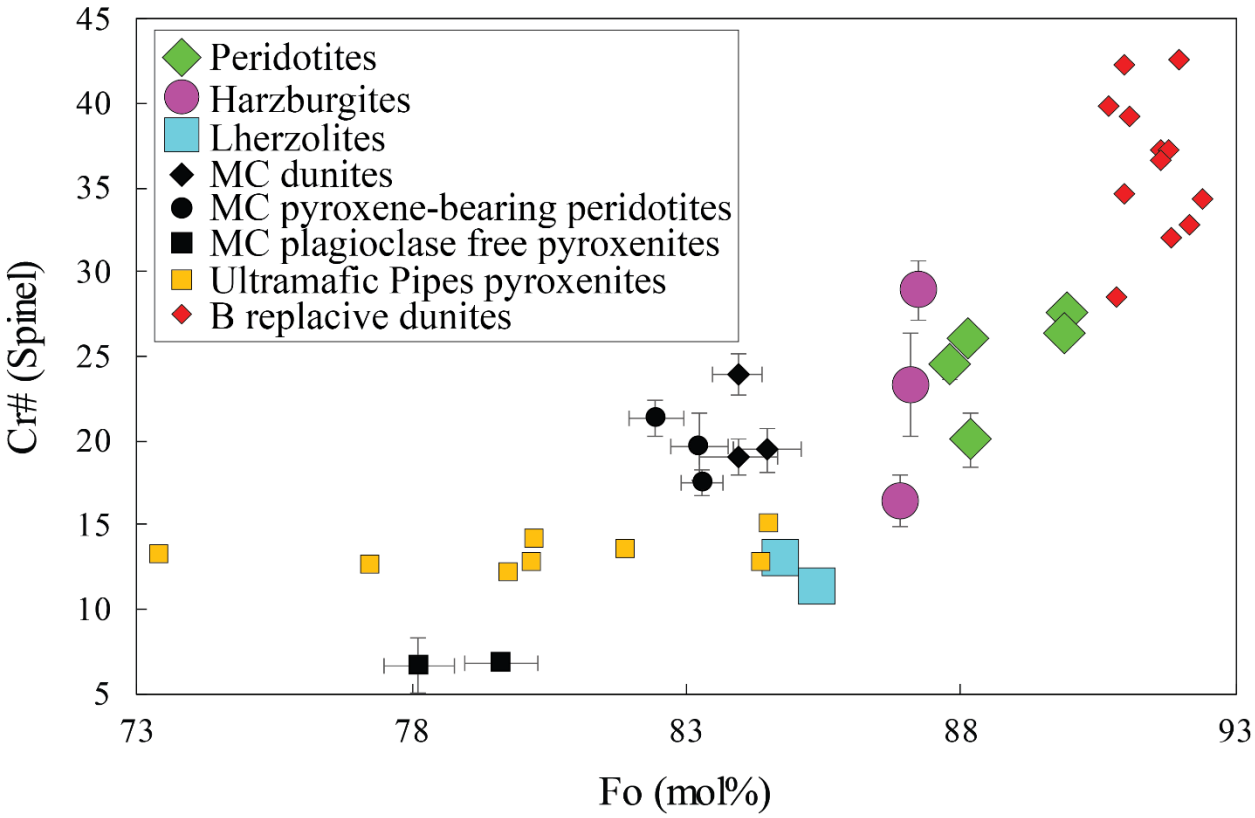

Fig. 12. Plot of Cr# [100 × Cr/(Cr+Al), mol%] of spinel versus forsterite proportion of coexisting olivine (mol%) for the Rocca d'Argimonia peridotites. Data are averaged per sample; error bars represent the standard deviation of the mean value (2σ). Dunites, pyroxene-bearing peridotites and plagioclase free pyroxenites from Monte Capio (MC) ultramafic sequence after Berno et al. (2020) are reported. Data are averaged per sample; error bars represent the standard deviation of the mean value (2σ). The error bars are in some cases within the symbol area. The compositions of spinel–olivine pairs from mantle replacive dunites of the Balmuccia (B) mantle sequence (Mazzucchelli et al., 2009) and of pyroxenites from the Ultramafic Pipes (Garuti et al., 2001) are reported for comparison.

The chondrite-normalized REE patterns of the Monte Capio dunites are characterized by nearly flat to slightly LREE enriched patterns (Fig. 13, data after Denyszyn et al., 2018), which are grossly similar to those of the Rocca d'Argimonia dunites and harzburgites (Fig. 9). Conversely, the Monte Capio pyroxenites exhibit nearly flat REE patterns, with a slight positive Eu anomaly, distinctly from the Rocca d'Argimonia pyroxenites, which typically show a slight MREE-HREE enrichment over the LREE.

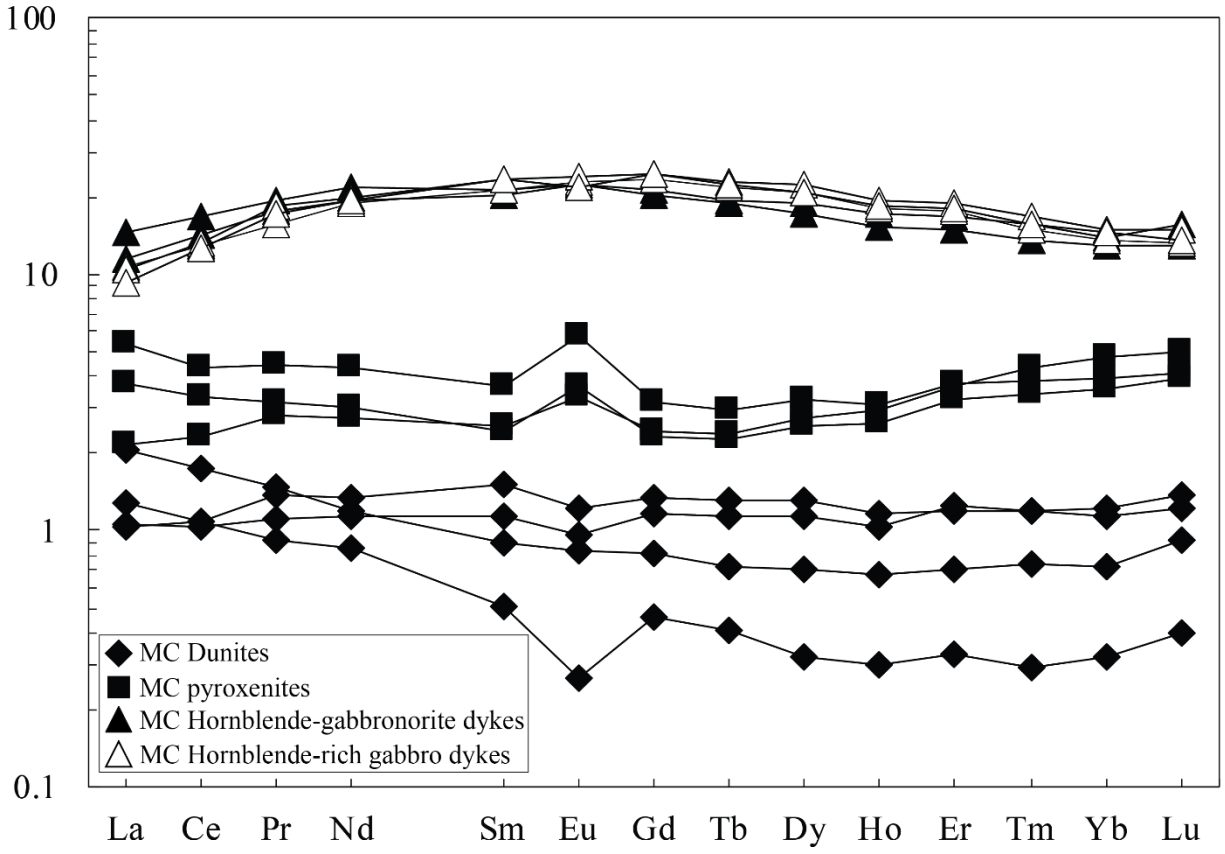

Fig. 13. Whole-rock REE compositions of rocks from Monte Capio (MC) sequence, normalized to CI chondrite (Sun and McDonough, 1989). Dunites and pyroxenites after Denyszyn et al. (2018); hornblende gabbronorite dykes and hornblende-rich gabbro dykes are unpublished data.

Because of the uncertainty in the crystallization age of the Monte Capio sequence (Klötzli et al., 2014; Denyszyn et al., 2018), the initial Nd-Sr isotopic compositions of Monte Capio samples (Berno et al., 2020) were calculated at 314 and 200 Ma (Fig. 14). Regardless of the age isotope corrections, the Monte Capio ultramafic rocks are isotopically slightly enriched compared to Rocca d'Argimonia peridotites and pyroxenites. On the other hand, Rocca d'Argimonia and Monte Capio gabbronoritic dykes display similar initial Nd-Sr isotopic signature.

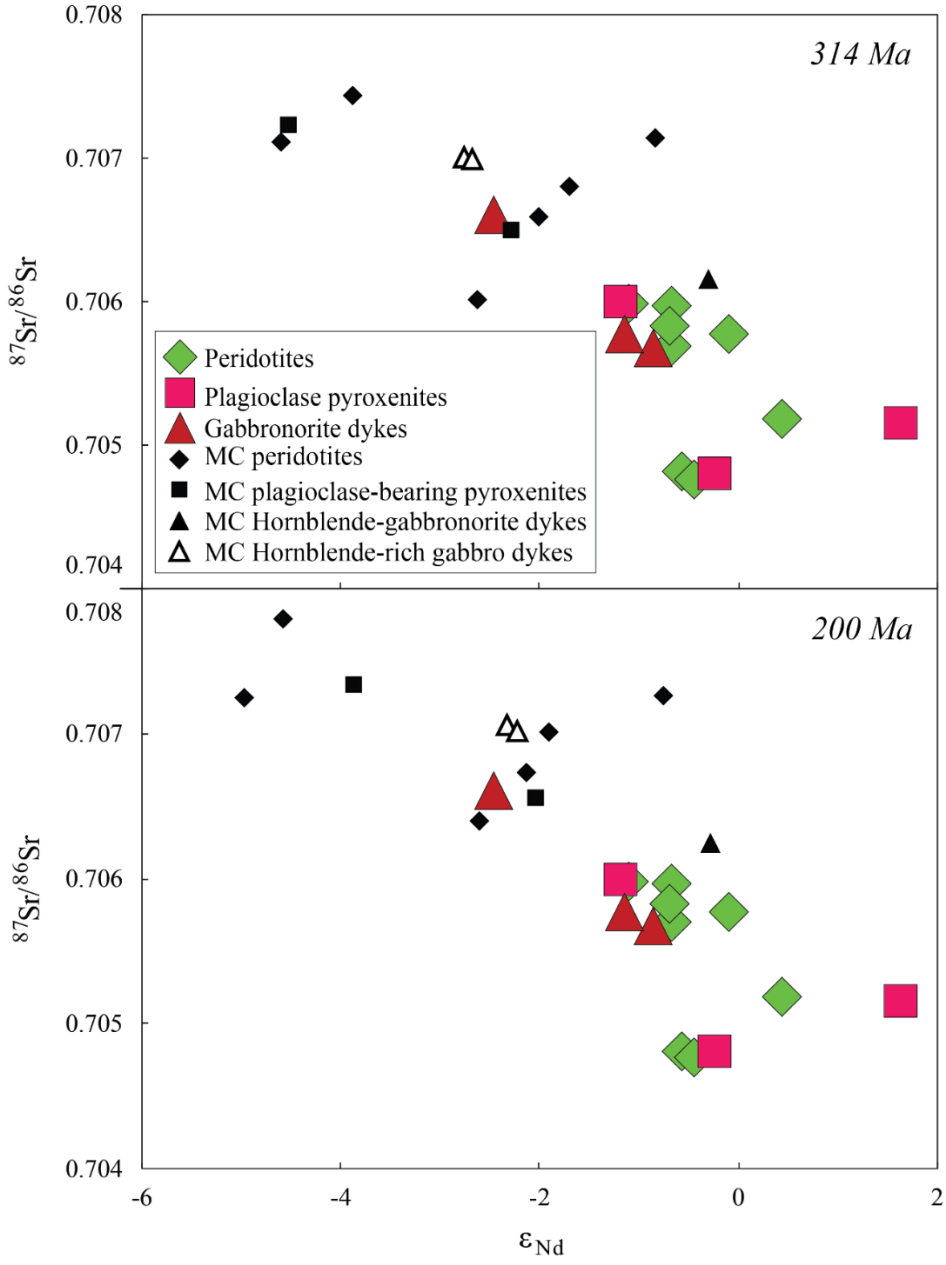

Fig. 14. Plot of initial $^{87}Sr/^{86}Sr$ versus initial ε_{Nd} compositions of the selected samples from the Rocca d'Argimonia sequence, calculated at 286 Ma. The whole-rock compositions of Monte Capio (MC) rocks (Berno et al. 2020) are reported for comparative purposes, and calculated at 314 Ma (following Klötzli et al., 2014) and 200 Ma (following Denyszyn et al., 2018).

7.1.3 Ultramafic Pipes

The Ultramafic Pipes are ultramafic bodies mostly consisting of plagioclase pyroxenites including relatively high amounts of amphibole and phlogopite, locally associated with olivine-rich cumulates (Garuti et al., 2001). They are located in the Main Gabbro and in the stratigraphically overlying metasediments of the Kinzigite Formation, and host Ni-Cu-PGE sulphide mineralizations. The Ultramafic Pipes were proposed to have crystallized at 287 Ma to 249 Ma from alkaline basalts (Locmelis et al., 2016; Fiorentini et al., 2018). In particular, textural relationships suggest the early formation of olivine-rich cumulates that were subsequently pervasively percolated by hydrous basic melts, thereby producing orthopyroxene, amphibole and phlogopite (Locmelis et al., 2016). It was suggested that the melts forming the olivine-rich cumulates and those crystallizing orthopyroxene, amphibole and phlogopite formed by the same primary magma, in turn originated from partial melting of subcontinental lithospheric mantle metasomatized in response to the Varisican subduction.

Compared to the Ultramafic Pipes, the Rocca d'Argimonia peridotites and pyroxenites are mineralogically distinct in the lack of phlogopite and in the occurrence of amphibole as an accessory phase (≤2 wt%, Antonicelli et al., 2020). In addition, the peridotites and the pyroxenites from the Ultramafic Pipes (Garuti et al., 2001; Denyszyn et al., 2018) have lower Mg# than the Rocca d'Argimonia counterparts (Fig. 8). The chemically evolved signature of the Ultramafic Pipes is sustained by the olivine compositions, which are relatively poor in forsterite component (Fig. 12). The spinel from the Ultramafic Pipes rocks has low Cr#, similar to spinel from the most evolved peridotites of the Rocca d'Argimonia sequence.

The pyroxenites from the Ultramafic Pipes (Garuti et al., 2001) show chondrite-normalized REE patterns characterized by LREE enrichment over MREE and HREE (Fig. 15). These pyroxenites have one to two orders of magnitude higher LREE concentrations than the Rocca d'Argimonia pyroxenites, which in turn display moderate LREE depletion compared to MREE and HREE (Fig. 9). On the other hand, the peridotites, the pyroxenites and the gabbroic pods from the Ultramafic Pipes (see also Fiorentini et al., 2018) have initial ε_{Nd} and $^{87}Sr/^{86}Sr$ similar to those of the rocks from the Rocca d'Argimonia sequence (Fig. 16). Hypothetically, the magmas forming the Ultramafic Pipes and the Rocca d'Argimonia sequences could therefore be derived from mantle sources with similar compositions, with the primary melts forming the Ultramafic Pipes developing in response to low degrees of partial melting.

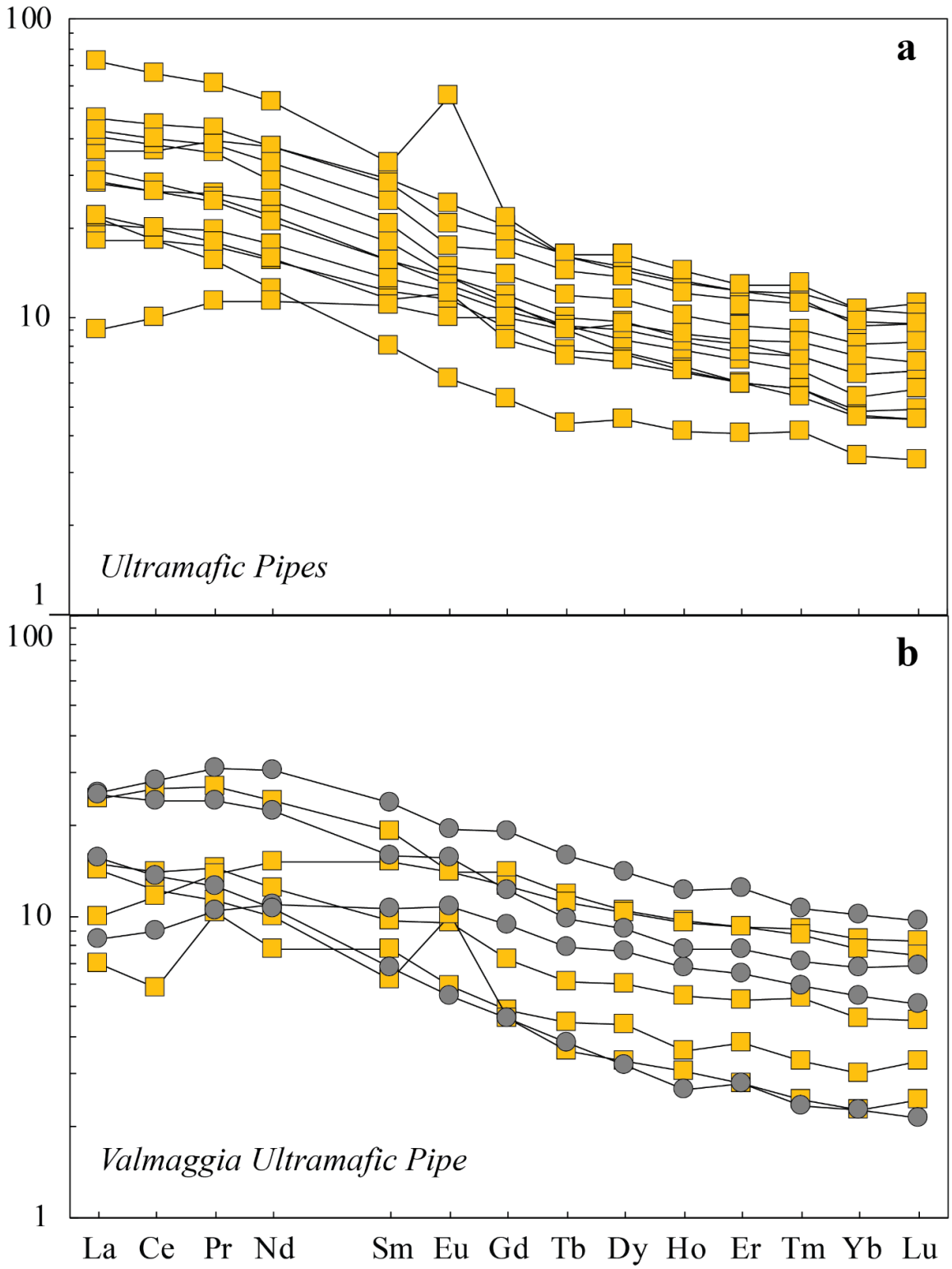

Fig. 15. Whole-rock REE compositions of Ultramafic Pipes rocks, normalized to CI chondrite (Sun and McDonough, 1989). (a) Patterns of pyroxenites from the Ultramafic Pipes (Bec d'Ovaga, Fei di Doccio, Castello di Gavala, Piancone la Frera) after Garuti et al. (2001). (b) Patterns of dunites (gray circles) and pyroxenites (orange squares) from Valmaggia ultramafic pipe after Denyszyn et al. (2018) and Garuti et al. (2001), respectively.

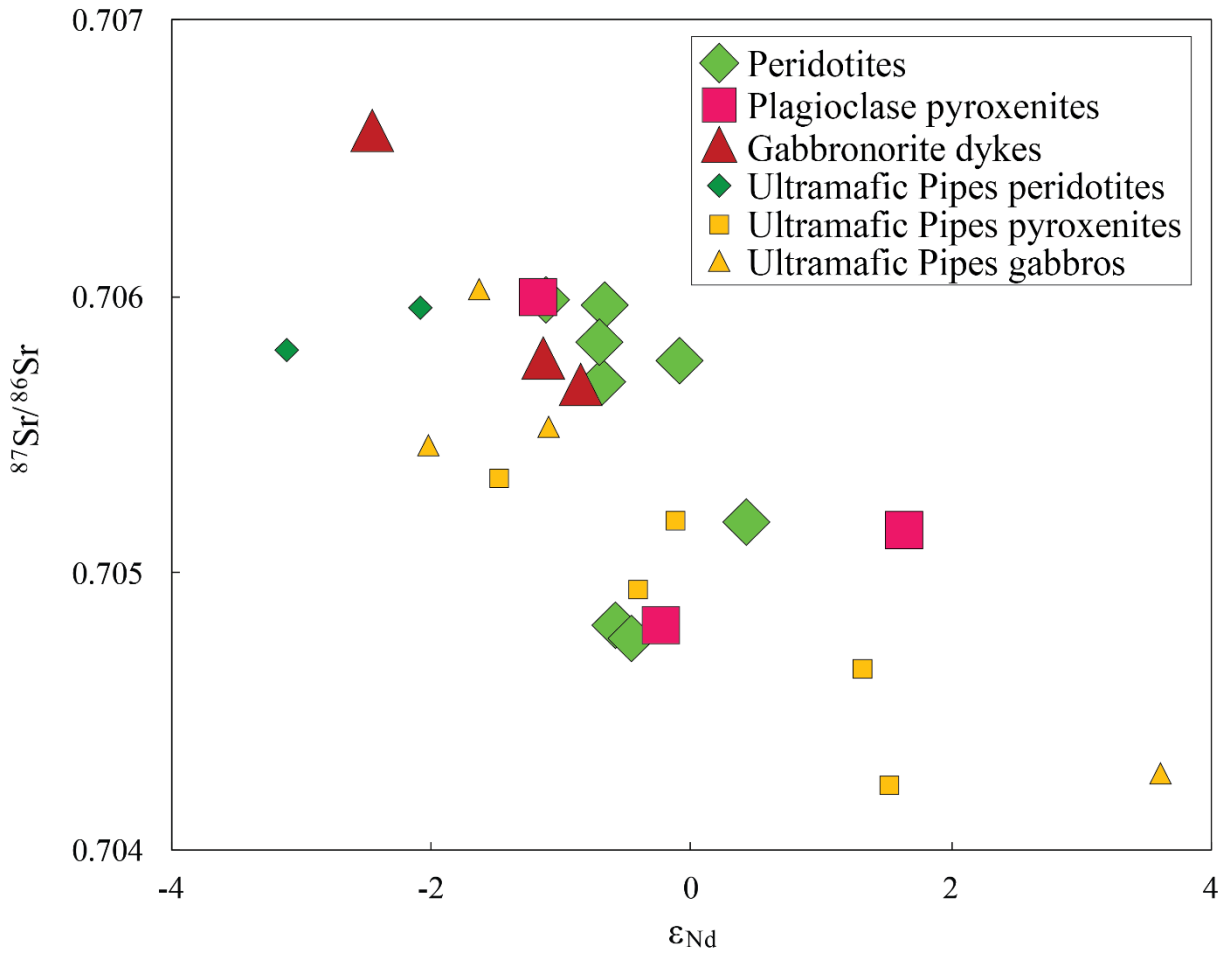

Fig. 16. Plot of initial $^{87}Sr/^{86}Sr$ versus initial ε_{Nd} compositions of the selected samples from the Rocca d'Argimonia sequence, calculated at 286 Ma. The compositions of peridotites, pyroxenites and gabbros from the ultramafic pipes (Garuti et al., 2001; Locmelis et al., 2016) are reported for comparison. The isotopic compositions of Ultramafic Pipes rocks were calculated at 286 Ma. Rocks from Valmaggia pipe were calculated at 249 Ma, following Locmelis et al. (2016).

7.1.4 Ultramafic cumulates from Sesia valley section

In the Sesia valley section of the Mafic Complex, ultramafic cumulate lenses are relatively frequent, and consist of peridotites (mainly dunites and harzburgites) and pyroxenites (Quick et al., 2003), similar to the Rocca d'Argimonia sequence. Little is known about the compositional characteristics and origin of the Sesia valley ultramafic lenses, but their Nd-Sr isotopic compositions were reported by Voshage et al. (1990).

We calculated the initial ε_{Nd} and initial $^{87}Sr/^{86}Sr$ of the ultramafic cumulates from Sesia valley section (Voshage et al., 1990) at 286 Ma. The pyroxenites show a wide range of Nd-Sr isotopic compositions, with $\varepsilon_{Nd(286\ Ma)}$ ranging from -7.5 to +3.0 and $^{87}Sr/^{86}Sr_{(286\ Ma)}$ ranging from 0.7099 to 0.7033, which depict a negative correlation (Fig. 17). The Nd-Sr isotopic compositions of two peridotites were reported by Voshage et al. (1990) and plot along the pyroxenite array. The Nd-Sr isotopic variability of the Sesia valley ultramafic cumulates was related to variable amounts of crustal contamination. The Rocca d'Argimonia peridotites and pyroxenites plot within the isotopically depleted range defined by the Sesia valley ultramafic cumulates.

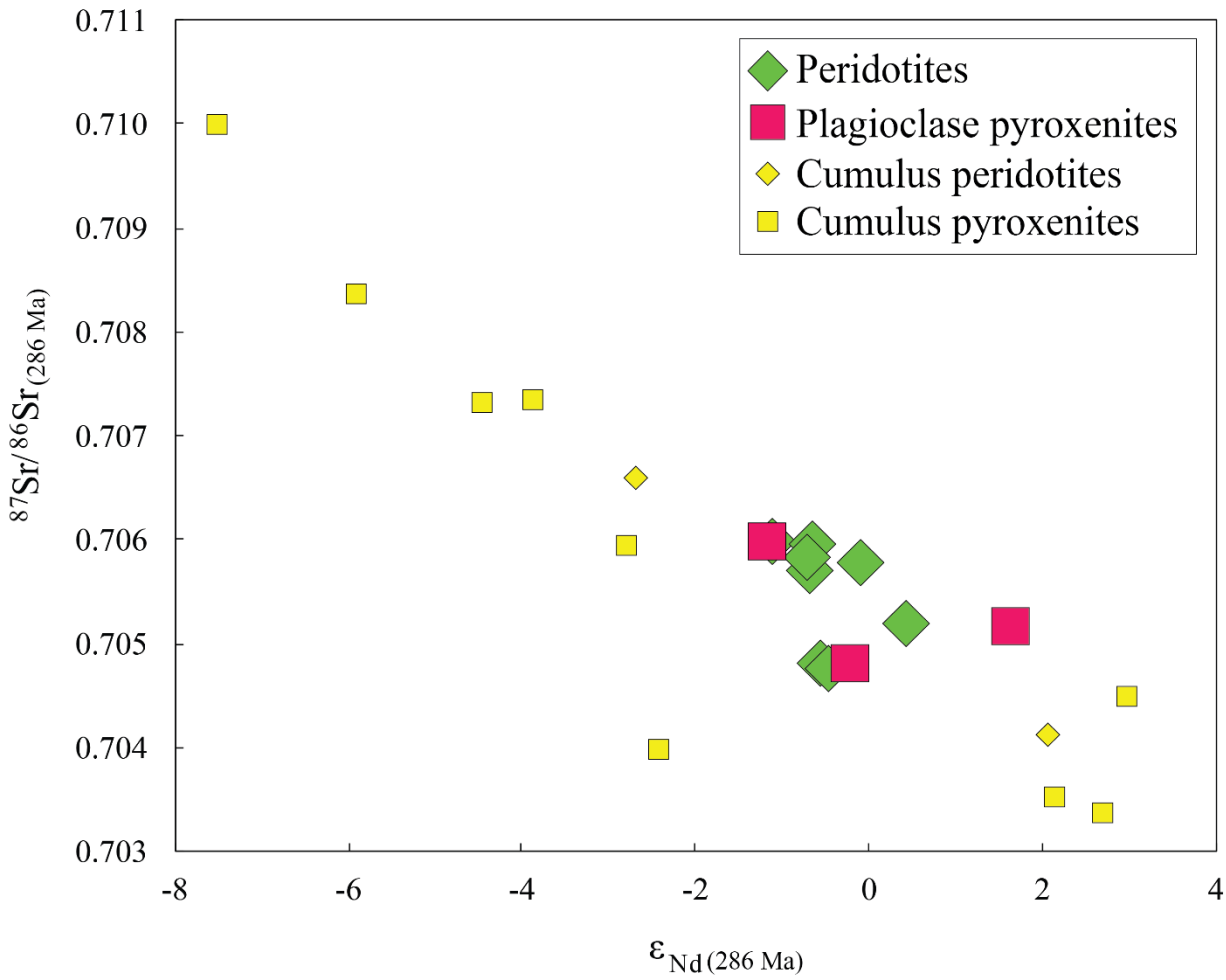

Fig. 17. Plot of initial $^{87}Sr/^{86}Sr$ versus initial ε_{Nd} compositions of the selected samples from the Rocca d'Argimonia sequence, calculated at 286 Ma. The compositions of ultramafic cumulus peridotites and pyroxenites from the Lower Mafic Complex (Voshage et al., 1990) calculated at 286 Ma are reported for comparison.

7.1.5 Gabbroic rocks from the Ivrea Mafic Complex

The Ivrea Mafic Complex was subdivided into two stratigraphically overlying units (Quick et al., 2003). The Lower Mafic Complex mainly consists of granoblastic amphibole gabbros that make up the southwestern sector of the intrusion, interlayered with minor norites and gabbronorites. The Upper Mafic Complex consists of nearly homogeneous gabbronorites and, towards the roof, of the so-called diorites. The transition between the Lower and the Upper Mafic Complex includes abundant paragneiss septa interlayered with gabbroic and noritic rocks, and is locally known as paragneiss-bearing belt (Sinigoi et al., 2011).

The gabbroic rocks from the Lower Mafic Complex and the paragneiss-bearing belt in the Val Sessera section show a wide Mg# range (Fig. 8). In particular, these rocks define a negative correlation between Mg# and CaO. The gabbronorites enclosing the Rocca d'Argimonia peridotite-pyroxenite association plot along this array.

Taken as a whole, the gabbroic rocks from the Lower and Upper Mafic Complex (Sinigoi et al., 1991; 2011) depict a positive correlation between Mg# and initial $^{87}Sr/^{86}Sr$ (Fig. 18). The Rocca d'Argimonia gabbronorite dykes and the gabbronorites enclosing the peridotite-pyroxenite association follow this correlation, which could be mostly related to a melt evolution driven by fractional crystallization and concomitant assimilation of crustal material (i.e. the AFC process of DePaolo, 1981).

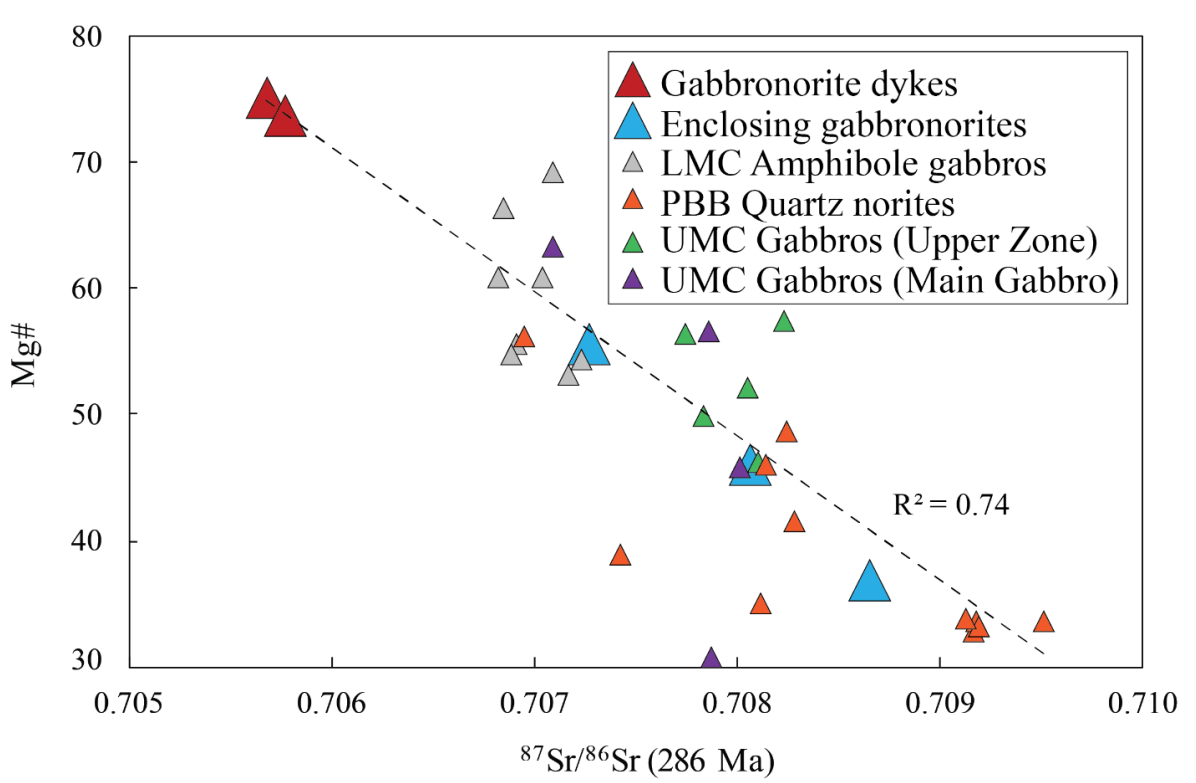

Fig. 18. Plot of Mg# [molarMg/(Mg+Fe^{2+}_{tot})×100] versus initial $^{87}Sr/^{86}Sr$ of gabbronorite dykes and enclosing gabbronorites from Rocca d'Argimonia. The compositions of gabbroic rocks from Lower Mafic Complex, Upper Mafic Complex and paragneiss-bearing belt calculated at 286 Ma are reported for comparison. Amphibole gabbros from the Lower Mafic Complex (LMC) and quartz norites from the paragneiss-bearing belt (PBB) of Val Sessera after Sinigoi et al. (2011). Gabbros from the Upper Zone and the Main Gabbro of the Upper Mafic Complex (UMC) after Sinigoi et al. (2016). The dashed line represents the correlation trend calculated for all samples.

The $\varepsilon_{Nd(286\ Ma)}$ of the gabbronorites enclosing the Rocca d'Argimonia peridotite-pyroxenite association is included within the range defined by the gabbroic rocks from the Sesia valley (Fig. 19). Notably, three Sesia valley gabbroic rocks are distinct in the depleted Nd-Sr isotopic signature. Voshage et al. (1990) proposed that these rocks retain their primary mantle signature, whereas most gabbroic rocks of the Mafic Complex record variable degrees of crustal contamination.

The Rocca d'Argimonia gabbronorite dykes show a moderate Nd-Sr isotopic depletion compared to most Sesia valley gabbroic rocks. Nevertheless, the Rocca d'Argimonia gabbronorite dykes exhibit Nd-Sr (and Hf) isotopic variations that could be reconciled with formation by variably contaminated melts.

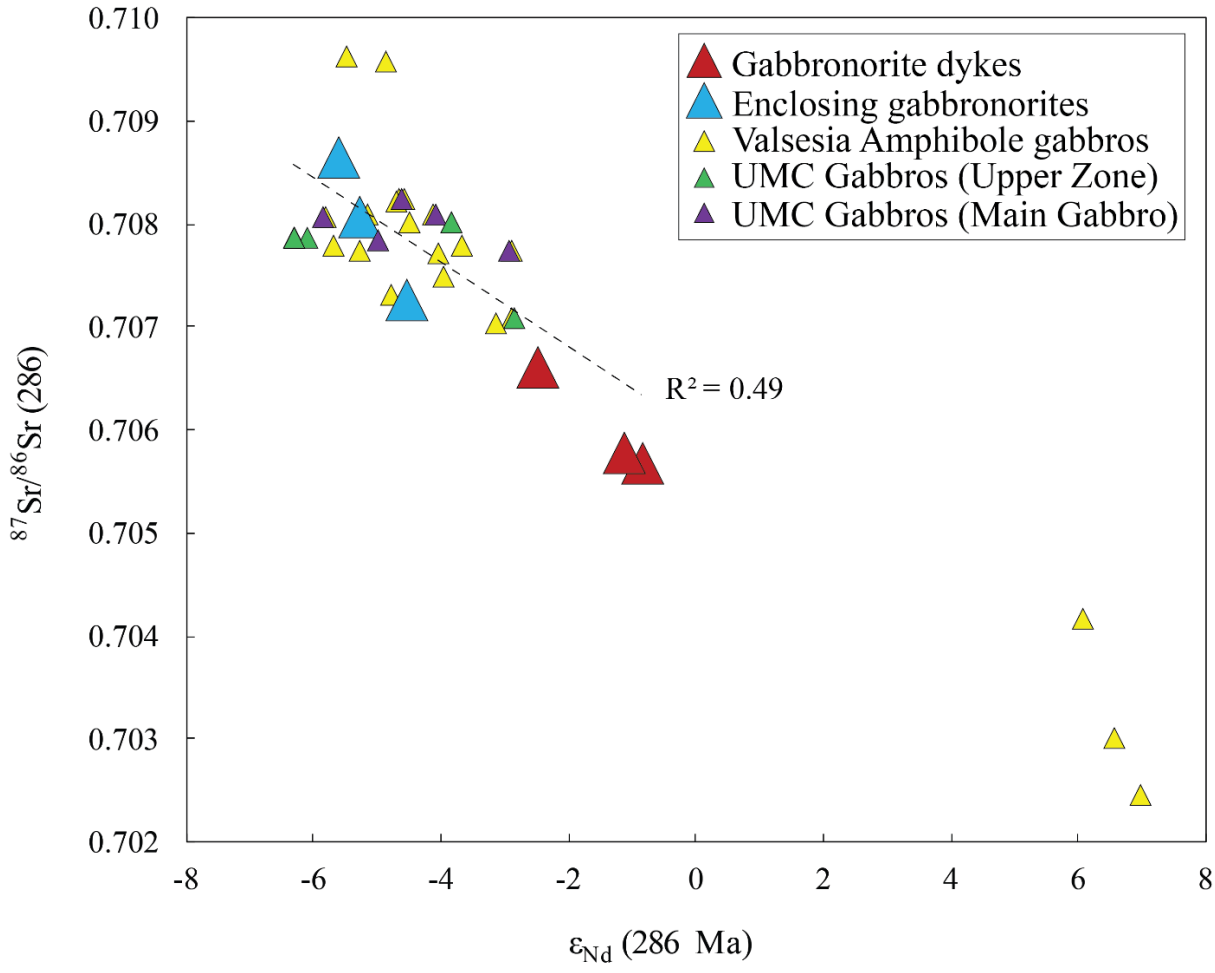

Fig. 19. Plot of initial ε_{Nd} versus initial $^{87}Sr/^{86}Sr$ of gabbronorite dykes and enclosing gabbronorites from Rocca d'Argimonia. The compositions of gabbroic rocks from Lower Mafic Complex and Upper Mafic Complex calculated at 286 Ma are reported for comparison. Amphibole gabbros from Sesia valley after Voshage et al. (1990). Gabbros from the Upper Zone and the Main Gabbro of the Upper Mafic Complex (UMC) after Sinigoi et al. (2016). The dashed line represents the correlation trend for all samples, excluding the three isotopically depleted samples.

7.2 Evidence for Nd-Sr-Hf isotopic disequilibrium in dunites

For the most primitive dunite BI4/1, the Nd-Sr-Hf isotopic analyses were carried out not only for the bulk rock, but also for clinopyroxene and amphibole separates. In addition, whole-rock isotope analyses were duplicated for this sample. The Nd-Sr-Hf isotopic compositions calculated at 286 Ma depict significant differences between mineral separates and whole-rock. In particular, the initial ratios of clinopyroxene and amphibole are slightly higher than initial $^{143}Nd/^{144}Nd$ and $^{176}Hf/^{177}Hf$ of the whole-rock, whereas the opposite relationship is observed for the initial $^{87}Sr/^{86}Sr$ ratio (Table 7). A similar discrepancy is found for dunite BI10/1, with the clinopyroxene separate showing a slightly more depleted Nd-Sr-Hf isotopic signature than the whole-rock.

The four Sm-Nd isotope analyses carried out for the dunite BI4/1 define an alignment corresponding to an age of 1034 ± 160 Ma (ε_{Nd} = -1.9, MSWD = 0.13; Fig. 20a). Notably, the clinopyroxene and the amphibole separates have closely similar $^{143}Nd/^{144}Nd$ and $^{147}Sm/^{144}Nd$ isotopic concentrations, despite different Sm and Nd concentrations. In particular, $^{143}Nd/^{144}Nd$ ratio calculated at 286 Ma of clinopyroxene and amphibole defines similar values, within the analytical uncertainty. (Table 7). In addition, the whole-rock duplicates correctly display $^{143}Nd/^{144}Nd$ and $^{147}Sm/^{144}Nd$ isotopic ratios within the analytical uncertainty. The "four-point isochron" observed in dunite BI4/1 could therefore be defined by the alignment of two main compositions, the clinopyroxene-amphibole pair and the whole-rock, with no geological meaning. Hence, the Nd isotope discrepancy between the whole-rock and the clinopyroxene (+ amphibole) in the dunites is interpreted to reflect the presence of at least one phase characterized by lower initial $^{143}Nd/^{144}Nd$ than clinopyroxene and amphibole (Fig. 21a). The whole-rock also exhibits lower $^{147}Sm/^{144}Nd$ than clinopyroxene and amphibole, thereby indicating that the Nd-isotopically enriched phase had relatively low $^{147}Sm/^{144}Nd$ (i.e., enriched in LREE over MREE).

In $^{176}Hf/^{177}Hf$ vs. $^{176}Lu/^{177}Hf$ plot, whole-rock, clinopyroxene and amphibole of dunite BI4/1 do not define a statistically representative alignment (Fig. 20b). In addition, clinopyroxene and amphibole produce a "two-point isochron" defining an age of 285 ± 22 Ma (initial ε_{Hf} = +7.8), which is consistent with the U-Pb zircon age obtained from the gabbronorites enclosing the peridotite-pyroxenite association. The whole-rock $^{176}Hf/^{177}Hf$ calculated at 286 Ma is lower compared to that of clinopyroxene and amphibole, thereby suggesting the occurrence in the dunite BI4/1 of at least one phase characterized by relatively low $^{176}Hf/^{177}Hf$ (Fig. 21b).

In $^{87}Sr/^{86}Sr$ vs. $^{87}Rb/^{86}Sr$ plot, whole-rock, clinopyroxene and amphibole of dunite BI4/1 do not define a statistically representative alignment (Fig. 20c). In particular, the clinopyroxene and the amphibole separates produce a "two-point isochron" defining an age of 245.6 ± 8.1 Ma (initial $^{87}Sr/^{86}Sr$ = 0.7045). This age is younger than the U-Pb zircon age obtained from the gabbronorites

enclosing the peridotite-pyroxenite sequence. Because of the low closure temperature for the Rb-Sr isotopic system in amphibole (e.g., Tribuzio et al., 1999), this Rb-Sr two-point alignment presumably dates a cooling event, in conjunction with either a Lower-Middle Triassic thermal perturbation or a slow cooling evolution following the intrusion in the lower continental crust. Notably, a Sm-Nd internal isochron of 267 ± 21 Ma (95% confidence level, MSWD = 0.72, n = 4) was reported by Mayer et al. (2000) for an amphibole gabbronorite from the Lower Mafic Complex. This age was interpreted either as a minimum age of formation of the metamorphic texture in the amphibole gabbronorite or as a cooling age after a thermal overprint. Irrespective of the geological meaning of the two-point Rb-Sr alignment of 245.6 ± 8.1 Ma, the whole-rock Sr isotopic ratio calculated at 286 Ma of dunite BI4/1 is significantly higher than the Sr isotopic ratio of clinopyroxene and amphibole separates. This finding suggests the occurrence in this dunite of at least one phase characterized by relatively Sr isotopic ratio (Fig. 21c).

In summary, the Nd-Hf-Sr isotopic systematics show significantly different values between whole-rock and clinopyroxene and amphibole separates for the most primitive dunites BI4/1 and BI10/1. The isotopic discrepancy documents the presence of at least one phase in these rocks that is isotopically Nd-Sr-Hf enriched compared to clinopyroxene and amphibole. In addition, the $^{147}Sm/^{144}Nd$ ratios of whole-rock, clinopyroxene and amphibole indicate that this phase has LREE enrichment over MREE. Dunites BI4/1 and BI10/1 include 91-92 vol% olivine (Antonicelli et al., 2020). Olivine typically shows negligible concentrations of Sm, Nd, Lu, Hf, Rb and Sr, and MREE enrichment over LREE. The other recognized accessory phases in the dunites (orthopyroxene, spinel and sulphides) also characteristically have low to negligible Sm, Nd, Hf, Rb and Sr concentrations. We conclude that olivine, orthopyroxene spinel and sulphides are not responsible for the Nd-Sr-Hf isotopic and LREE enrichment of the whole-rock compared to clinopyroxene and amphibole. This Nd-Sr-Hf isotopic and LREE enrichment must reflect the presence of a "hidden" fine-grained accessory phase in the dunites.

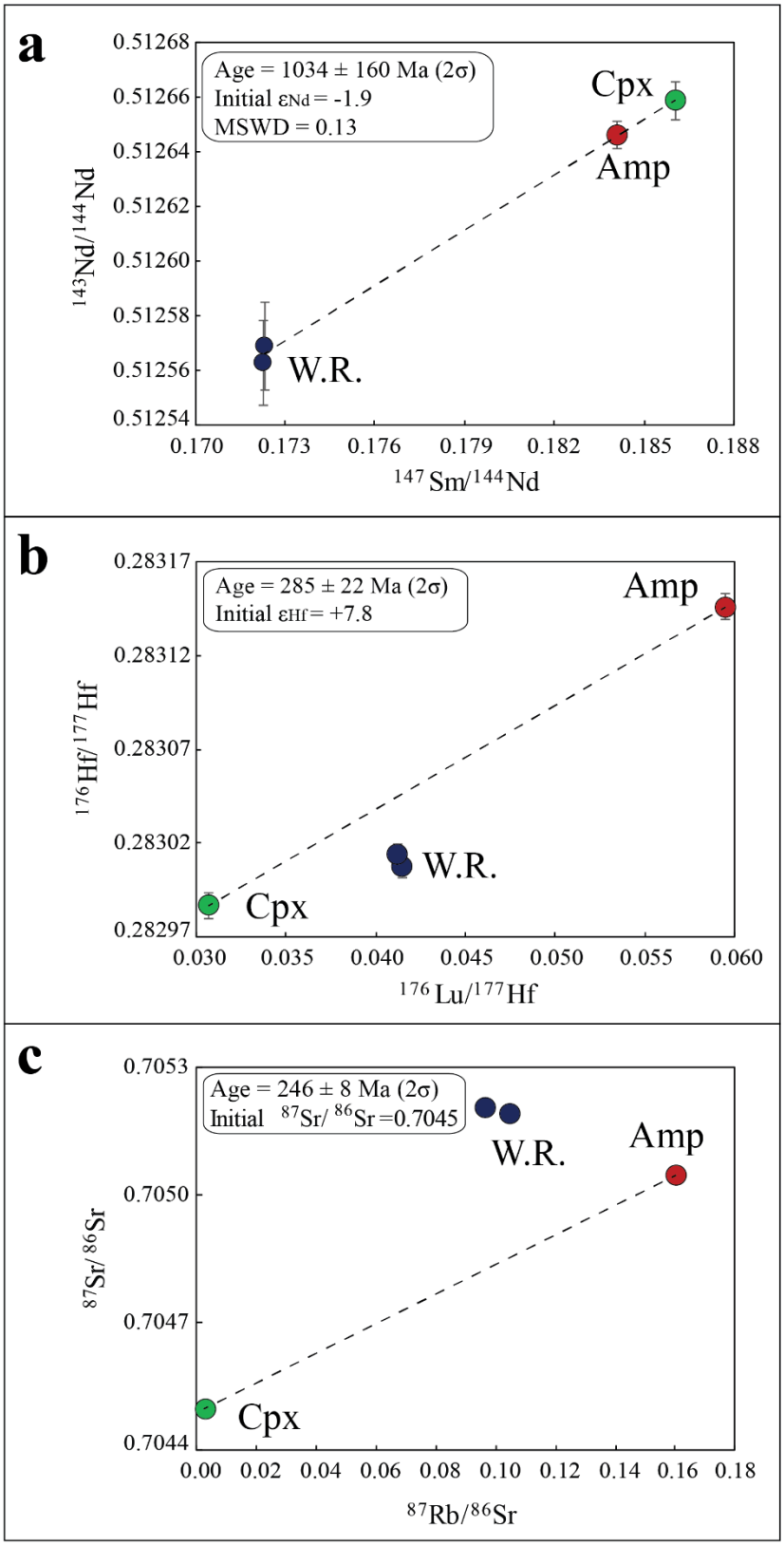

Fig. 20. Isochron plots for dunite BI4/1. W.R: whole-rock, Cpx: clinopyroxene separate, Amp: amphibole separate. The error bars represent the calculated error per each analysis (1σ) and are in most cases within the symbol area. (a) $^{143}Nd/^{144}Nd$ versus $^{147}Sm/^{144}Nd$. (b) $^{176}Hf/^{177}Hf$ versus $^{176}Lu/^{177}Hf$. (c) $^{87}Sr/^{86}Sr$ versus $^{87}Rb/^{86}Sr$.

Based on major element mass balance calculations, the clinopyroxene and the amphibole amounts in dunite BI4/1 were estimated to be 3.4 wt% and 1.1 wt%, respectively (Antonicelli et al., 2020). We use these mineral proportions to estimate the isotopic ratios of a hypothetical "hidden" phase in this dunite (Table 8). In this calculation, we assumed that: (i) olivine, orthopyroxene, spinel and sulphides have negligible Sm, Nd, Rb, Sr, Lu e Hf concentrations, and (ii) the proportion of the "hidden" phase is for instance 1 wt% and 2 wt%. The calculation consists in balancing isotopic ratios of whole-rock with the "hidden" phase maintaining fixed the contribution of clinopyroxene + amphibole at 3.4 wt% and 1.1 wt%, respectively. Assuming 1 wt% "hidden" phase, we obtain $\varepsilon_{Nd(286\ Ma)}$ = -6.2, $\varepsilon_{Hf(286\ Ma)}$ = +1.4, $^{87}Sr/^{86}Sr_{(286\ Ma)}$ = 0.7062 (Fig. 21). If the "hidden" phase was 2 wt%, we obtain $\varepsilon_{Nd(286\ Ma)}$ = -3.4, $\varepsilon_{Hf(286\ Ma)}$ = +4.2, $^{87}Sr/^{86}Sr_{(286\ Ma)}$ = 0.7055. The mass balance calculations also indicate that the "hidden" phase was not only characterized by LREE enrichment over MREE but also by high Rb/Sr ratio.

The potential occurrence of an isotopically enriched "hidden" phase in the dunites BI4/1 and BI10/1 needs to be verified with further analyses, such as scanning electron microscopy investigations and Nd-Hf-Sr isotopic analysis of olivine separates. The hypothetical "hidden" phase could be interstitial with respect to olivine, similar to clinopyroxene, orthopyroxene and amphibole, or be present as inclusion within olivine. In the first scenario, the formation of an isotopically enriched accessory phase (e.g., apatite) could be related to percolation of late stage melts through the dunite, after the crystallization of clinopyroxene and amphibole, for instance released from the isotopically enriched gabbronorites (Fig. 10) enclosing the peridotite-pyroxenite sequence.

The hypothesis of an isotopically enriched phase included in olivine is consistent with the petrogenetic scenario depicted by Antonicelli et al. (2020). Following this scenario, the growth of clinopyroxene, amphibole and orthopyroxene in the dunites was due to a process of reactive melt flow through a pre-existing olivine-rich matrix. The hypothetical "hidden" phase included in olivine could be the product of the inclusion of melts trapped during olivine growth, before the process of reactive melt migration. Notably, the Nd-Sr isotopic signature of calculated 2 wt% "hidden" phase is similar to that of the peridotites of the Monte Capio magmatic sequence (Berno et al., 2020; see also Fig. 14) and the Finero mantle body (Voshage et al., 1987).

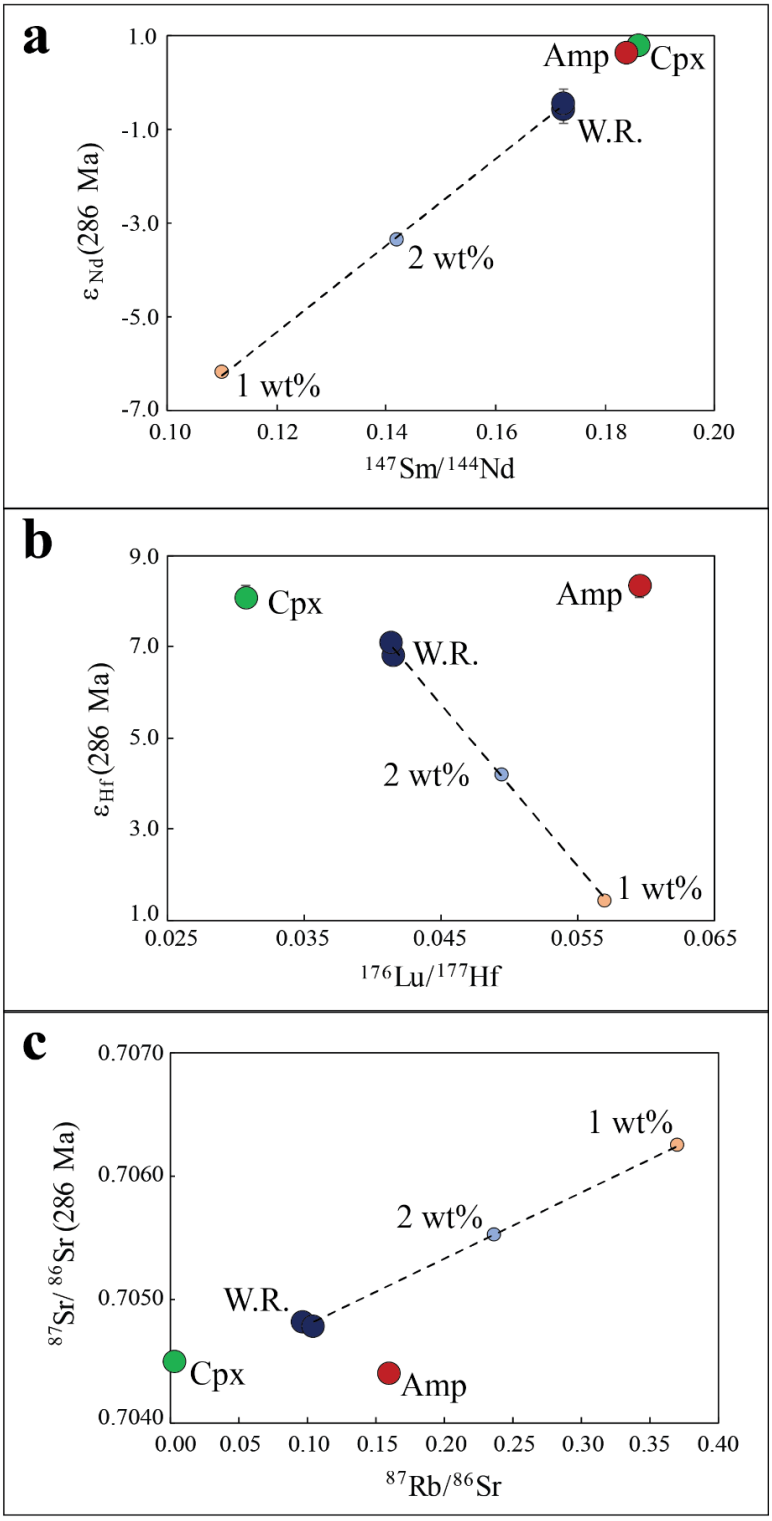

Fig. 21 Plot of isotopic compositions of dunite BI4/1. W.R: whole-rock, Cpx: clinopyroxene separate, Amp: amphibole separate. The error bars represent the calculated error per each analyses (1σ) and are in most cases within the symbol area. The light blue and the pink circles are the isotopic compositions of a hypothetic "hidden phase" calculated based on mass balance considerations (see text for further details), assuming that it represents 1 and 2 wt% of the dunite, respectively. (a) Initial ε_{Nd} versus $^{147}Sm/^{144}Nd$. (b) Initial ε_{Hf} versus $^{176}Lu/^{177}Hf$. (c) Initial $^{87}Sr/^{86}Sr$ versus $^{87}Rb/^{86}Sr$.

	$^{147}Sm/^{144}Nd$	ε_{Nd} i	$^{87}Rb/^{86}Sr$	$^{87}Sr/^{86}Sr$ i	$^{176}Lu/^{177}Hf$	ε_{Hf} i
W.R.	0.172	-0.5	0.101	0.70479	0.041	+6.9
Cpx + Amp	0.186	+0.8	0.041	0.70446	0.038	+8.2
Hidden phase 2%	0.142	-3.4	0.236	0.70552	0.049	+4.2
Hidden phase 1%	0.110	-6.2	0.370	0.70624	0.057	+1.4

Table 8. Calculated Sm/Nd, Rb/Sr and Lu/Hf isotopic compositions of the presumed hidden phase in dunite BI4/1; ε_{Nd}, $^{87}Sr/^{86}Sr$ and ε_{Hf} calculated at 286 Ma. W.R: whole-rock, average of two analyses reported in Table 7. Cpx + Amp: weighted average of clinopyroxene and amphibole compositions (see Table 7), based on their mineral proportions (3.4 wt% and 1.1 wt%, respectively, following the calculations reported in Antonicelli et al., 2020). Hidden phase 2% = calculated compositions of the presumed hidden phase obtained balancing "Cpx + Amp" and W.R., assuming a 2 wt% proportion of the hidden phase. Hidden phase 1% = calculated composition of the presumed hidden phase obtained balancing "Cpx + Amp" and W.R., assuming a 1 wt% proportion of the hidden phase.

7.3 Implications for the formation of the Rocca d'Argimonia ultramafic sequence

7.3.1 Relationships between peridotites, pyroxenites and gabbronorite dykes

Based on a negative correlation between forsterite proportion and $\delta^{18}O$ of olivine, Antonicelli et al. (2020) inferred an open system magmatic origin for the Rocca d'Argimonia peridotites, involving a crustal contamination component. It was proposed that the peridotites formed by a process of pervasive reactive melt migration of crustally contaminated, chemically evolved melts through an olivine-rich matrix. Following this hypothesis, the percolating melt triggered partial dissolution of olivine coupled with crystallization of orthopyroxene, clinopyroxene and amphibole. This process was named "contaminating melt flow" and was associated with chemical modification of the pre-existing olivine, such as decreasing forsterite proportion and increasing $\delta^{18}O$. The negative correlation between forsterite proportion and $\delta^{18}O$ of olivine was related to variations in the melt/rock ratio, which is expected to decrease with ongoing magmatic evolution. Antonicelli et al. (2020) also indicated that the gabbronorite dykes crosscutting the peridotites developed soon after the process of "contaminating melt flow".

The REE compositions of the gabbronorite dykes cannot be related to the melt compositions. The chondrite-normalized REE patterns of these gabbronorites are characterized by Eu positive anomaly, which may be attributed to a process of plagioclase accumulation. The gabbronorite dykes display significant Nd, Sr and Hf isotopic variations (Fig. 10). In particular, gabbronorite dyke BI10/3 shows lower $\varepsilon_{Nd(286\ Ma)}$ and $\varepsilon_{Hf(286\ Ma)}$ and higher $^{87}Sr/^{86}Sr_{(286\ Ma)}$ than gabbronorite dykes BI8/1 and BI50/3. The gabbronorite dyke BI10/3 also has anomalously high Mg# (82), which was attributed to local dissolution and assimilation of peridotite material by the migrating melt and/or diffusive Fe-Mg exchange between peridotite minerals and melt (Antonicelli et al., 2020). We exclude, however, that the enriched Nd-Hf-Sr isotopic signature of gabbronorite dyke BI10/3 is related to the interaction of the gabbronorite-forming melt with host dunite, because the dunites have relatively high $\varepsilon_{Nd(286\ Ma)}$ and $\varepsilon_{Hf(286\ Ma)}$ and low $^{87}Sr/^{86}Sr_{(286\ Ma)}$. The Nd and Sr isotopic compositions of the gabbronorite dykes notably follow the rough correlations defined by the gabbroic rocks of the Ivrea Mafic Complex (Figs. 18 and 19). These correlations are probably related to formation of the gabbroic rocks by mantle-derived melts variably contaminated by crustal material (Voshage et al., 1990; Sinigoi et al., 1991, 2016). In particular, the gabbronorite dyke BI10/3 most likely crystallized from a melt having higher crustal component than the melts forming the gabbronorite dykes BI8/1 and BI50/3.

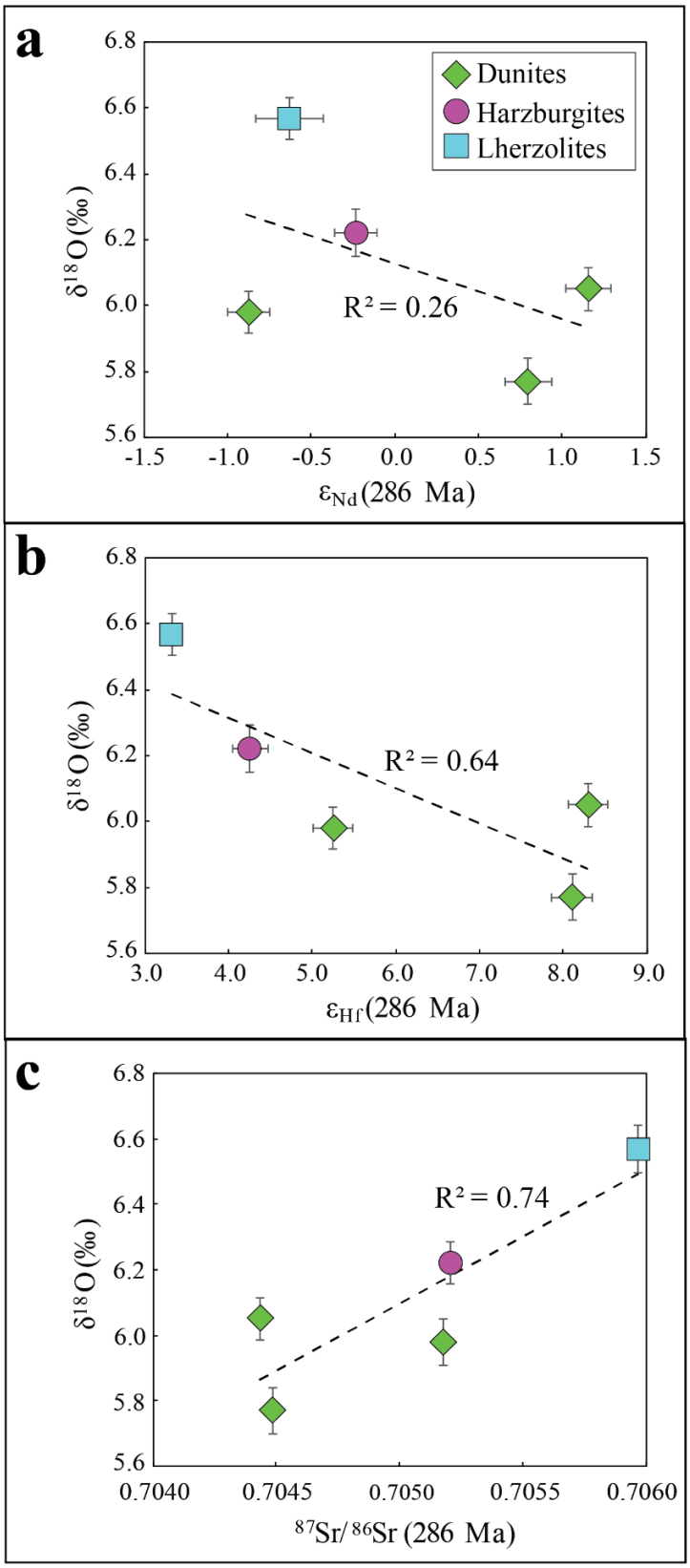

Fig. 22. Plot of $\delta^{18}O$ (weighted average ± 2σ) of peridotite olivine versus: (a) initial ε_{Nd} of associated clinopyroxene, (b) initial ε_{Hf} of associated clinopyroxene, and (c) initial $^{87}Sr/^{86}Sr$ of associated clinopyroxene. Because the $^{87}Sr/^{86}Sr$ ratio of lherzolite BI30/5 clinopyroxene is not available, we used the whole-rock analysis for this sample. The dashed lines represent the correlation trends.

Contrary to olivine $\delta^{18}O$, the Nd isotopic ratio of the Rocca d'Argimonia peridotites do not depict a clear correlation with forsterite proportion of olivine or with whole-rock Mg# (Fig. 23). Note, however, that the $\varepsilon_{Nd(286\ Ma)}$ of the six analysed peridotites displays limited variability, from +0.4 to -0.9. This variability is comparable to that observed between whole-rock and mineral separates for the most primitive dunites. For instance, whole-rock and clinopyroxene from dunite sample BI4/1 have $\varepsilon_{Nd(286\ Ma)}$ of -0.5 and +0.8, respectively. Similarly to what is observed for the whole-rocks, the Nd isotopic compositions of the peridotite clinopyroxenes show limited variability and do not produce a statistically significant correlation with olivine $\delta^{18}O$ (Fig. 22).

The Hf-Sr isotopic ratios of the peridotites show relatively wide variations. In particular, $\varepsilon_{Hf(286\ Ma)}$ and $^{87}Sr/^{86}Sr_{(286\ Ma)}$ of the peridotites range from +3.4 to +8.8 and from 0.7048 to 0.7060 (Fig. 10) and depict rough positive and negative correlations with Mg#, respectively (Fig. 23). Similar relationships are observed if the $\varepsilon_{Hf(286\ Ma)}$ and $^{87}Sr/^{86}Sr_{(286\ Ma)}$ of clinopyroxene separates are plotted against olivine $\delta^{18}O$ (Fig. 23). Hence, the Hf and Sr isotopic variability of the peridotites is consistent with the origin of peridotites after a formation process associated with crustal contamination. Note that these correlations argue against the process of "contaminating melt flow" proposed by Antonicelli et al. (2020), which implies nearly constant radiogenic isotope ratios for the peridotites. Following the "contaminating melt flow" scenario, the radiogenic isotopic signature of the peridotites should actually be dominated by the isotopic compositions of the melt reactively migrating through the olivine-rich matrix. The Hf-Sr isotopic correlations against whole-rock Mg# and olivine $\delta^{18}O$ instead suggest that the crustal contamination was driven by fractional crystallization and concomitant assimilation of isotopically enriched crustal material (i.e., the AFC of DePaolo, 1981). Following the AFC hypothesis, the narrow Nd isotopic variability of the peridotites could imply that the mantle parental melt and the crustal component had similar Nd isotopic signature.

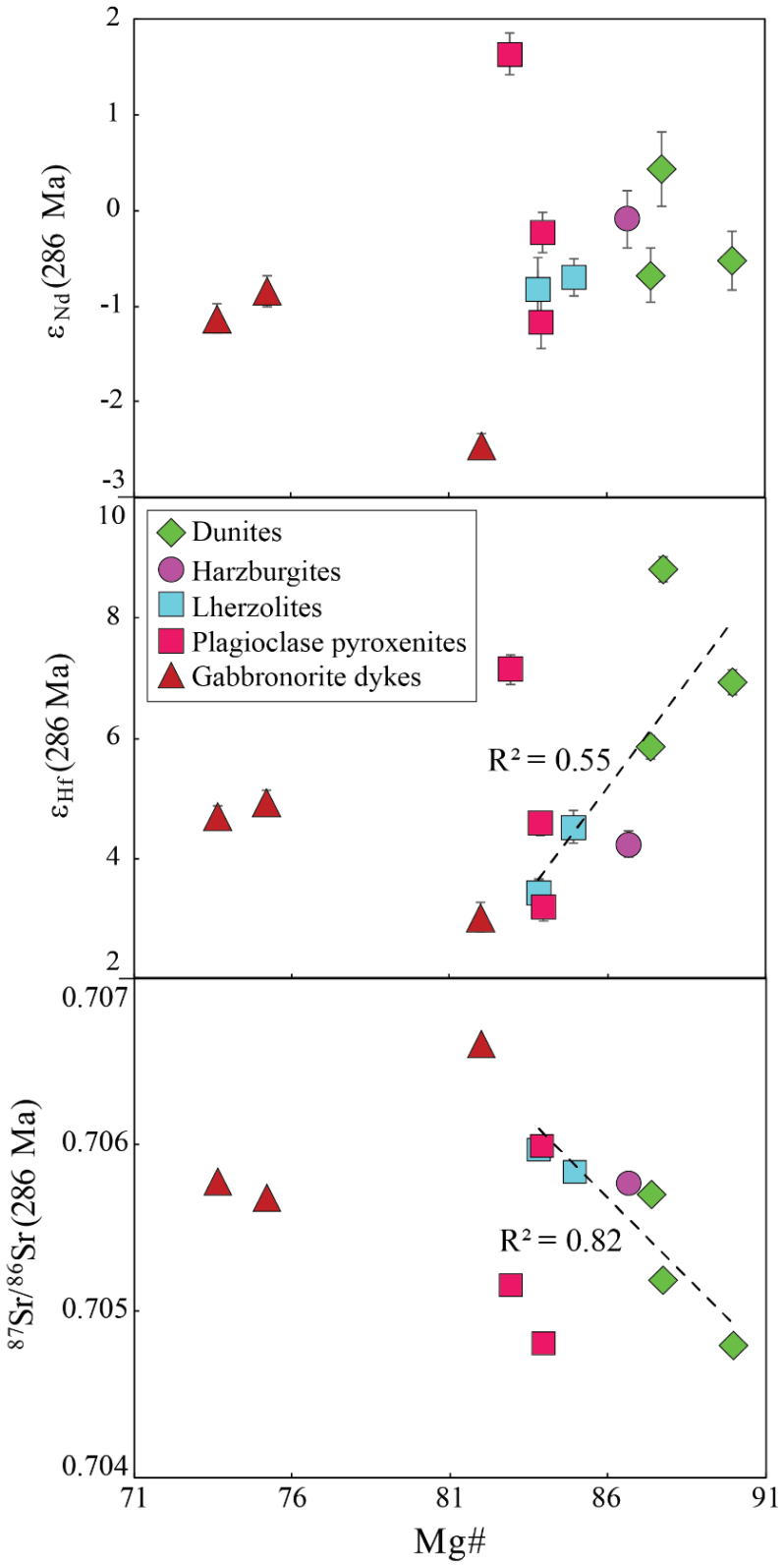

Fig. 23. Plot of initial ε_{Nd}, initial ε_{Hf} and initial $^{87}Sr/^{86}Sr$ versus whole-rock Mg# [molar $Mg/(Mg+Fe^{2+}_{tot})\times100$] of Rocca d'Argimonia peridotites, pyroxenites and gabbronorite dykes. The error bars represent the calculated error per each analysis (1σ) and are in most cases within the symbol area. The dashed line represents the correlation trend calculated for the peridotites. For dunite BI4/1 and lherzolite BI30/5, the mean isotopic values of the duplicates are reported.

The Rocca d'Argimonia pyroxenites lack of olivine and have high orthopyroxene/clinopyroxene modal ratio (Fig. 3a). The Nd-Sr-Hf isotopic signature of three analysed pyroxenites ($\varepsilon_{Nd(286\ Ma)}$ = +1.6 to -1.2, $^{87}Sr/^{86}Sr_{(286\ Ma)}$ = 0.7048 to 0.7060, and $\varepsilon_{Hf(286\ Ma)}$ = +7.1 to +3.2) is similar to that of associated peridotites (Figs. 10 and 23). Following the petrogenetic scenario of "contaminating melt flow" proposed by Antonicelli et al. (2020) for the Rocca d'Argimonia peridotites, the formation of the associated pyroxenites could be related to a process of reactive melt flow characterized by a high melt/olivine ratio, which led to the complete dissolution of the pre-existing olivine. This process is consistent with the lack of isotopic distinction between the pyroxenites and the peridotites. Alternatively, the pyroxenites could represent the crystallization products of melts residual after the crystallization of the peridotites. If the peridotite-pyroxenite association formed in response to an AFC-type process, however, the pyroxenites are expected to be isotopically enriched, at least for the Sr and Hf isotopic ratios, compared to the peridotites.

In summary, the data produced indicate that the Rocca d'Argimonia peridotite-pyroxenite association formed in response to a complex magmatic evolution. A possible scenario is represented by a two-stage magmatic evolution with an intrusion of a primitive mantle-derived magma initially evolving through an AFC-type process, thereby forming a melt-poor olivine-rich mush having slightly heterogeneous radiogenic isotopic signature. Subsequently, the pervasive reactive migration of crustally contaminated melts through the crystal mush produced the crystallization of orthopyroxene, clinopyroxene and amphibole at the expenses of olivine. This second stage process resulted in the differentiation of pyroxenites, lherzolites, harzburgites and dunites with decreasing melt/rock ratio. Further investigations are however needed to refine the petrogentic conceptual model here proposed for the formation of Rocca d'Argimonia ultramafic sequence. Valuable information could be provided by the definition of the pyroxene oxygen isotopic signature, which should track the crustal contamination evolution during the peridotite-pyroxenite forming process.

7.3.2 Relationships between the peridotite-pyroxenite association and the enclosing gabbronorites

The gabbronorites enclosing the ultramafic sequence show a marked compositional variability, both in modal proportions (Fig. 3b) and whole-rock compositions. In particular, the selected samples have Mg# ranging from 56 to 37 (Fig. 8) and variable chondrite-normalized REE patterns, typically characterized by evident LREE enrichment over MREE and HREE. The gabbronorites enclosing the ultramafic sequence are therefore chemically distinct from the gabbronorite dykes crosscutting the ultramafic sequence. For instance, the gabbronorite dykes display high Mg# (≥74) and nearly flat REE patterns. In addition, there is no overlap between the Nd-Sr-Hf isotopic compositions of the enclosing gabbronorites and those of the gabbronorite dykes (Fig. 10). In particular, the enclosing gabbronorites show enriched Nd-Sr-Hf isotopic compositions compared to the peridotite-pyroxenite sequence and included gabbronorite dykes. The chemical and isotopic compositions of the enclosing gabbronorites follow the rough correlations defined by all gabbroic-dioritic rocks of the Ivrea Mafic Complex (Figs. 18 and 19), and document that these rocks formed by highly evolved melts possessing a substantial crustal component (see Voshage et al., 1990; Sinigoi et al., 2011, 2016).

The fieldwork observations did not reveal relative chronology relationships between the Rocca d'Argimonia peridotite-pyroxenite sequence and the enclosing gabbronorites (Fig. 2). Where contacts between the peridotite-pyroxenite sequence and the enclosing gabbronorites are preserved, I found pyroxenites and gabbronorites displaying a concordant foliation. Hence, two main scenarios may be formulated for the relationships between the peridotite-pyroxenite sequence and the enclosing gabbronorites. In the first, the peridotite-pyroxenite association formed in response to an intrusion of a primitive mantle-derived magma into the gabbronorites, or into a magma-poor crystal mush rich in plagioclase and pyroxene-amphibole. Following this hypothesis, the mantle-derived magma underwent a substantial crustal contamination operated by hybrid melts with an enriched Nd-Sr-Hf isotopic signature (i.e., the gabbronorite-forming melts) near the host material, thereby giving rise to the pyroxenites. Far from the contact with the host material, the mantle-derived magma could experience a magmatic evolution associated with minor crustal contamination, thereby forming the peridotites. A high temperature deformation event could have subsequently erased the original intrusion relationships between the peridotite-pyroxenite sequence and the enclosing gabbronorites. In the second scenario, the primitive mantle-derived magma intruded the deep continental crust and formed a melt-poor olivine-rich crystal mush upon cooling. Following this hypothesis, the subsequent accretion of the Mafic Complex (Sinigoi et al., 2016) enclosed this mantle-derived partially molten material. This process could enable the interaction of the olivine-rich crystal mush with highly evolved hybrid melts, thereby forming the pyroxenites in response to a high melt/olivine-rich matrix ratio.

8 Concluding remarks

The present study deals with the origin of the Rocca d'Argimonia mafic-ultramafic sequence, which is enclosed within the gabbronoritic rocks of the lower sector of the Ivrea Mafic Complex (Sinigoi et al., 1991; Quick et al., 2003). Mostly based on whole-rock chemistry, Nd-Sr-Hf isotopic compositions of whole-rocks and clinopyroxene separates, and U-Pb zircon geochronology, the following concluding remarks are drawn.

The Nd-Sr isotopic signature of the Rocca d'Argimonia peridotites is enriched with respect to that of the Balmuccia mantle lherzolites, which are also enclosed within the Ivrea Mafic Complex (e.g. Quick et al., 1995). In particular, the only isotopic analysis reported in the literature for the Balmuccia replacive dunites ($\varepsilon_{Nd(286\ Ma)}$ = +2.9, $^{87}Sr/^{86}Sr_{(286\ Ma)}$ = 0.7041; Voshage et al., 1988) shows a distinct Nd-Sr fingerprint compared to the Rocca d'Argimonia dunites, which in turn have $\varepsilon_{Nd(286\ Ma)}$ of -0.7 to +0.4 and $^{87}Sr/^{86}Sr_{(286\ Ma)}$ of 0.7048 to 0.7057. No isotopic inheritance from the Balmuccia mantle sequence is therefore retained by the Rocca d'Argimonia peridotite-pyroxenite sequence. Similarly, the lack of any chemical correspondence between the Balmuccia and the Rocca d'Argimonia dunites was reported by Antonicelli et al. (2020) based on major element mineral compositions.

The petrographic, chemical and isotopic characteristics of the Rocca d'Argimonia peridotite-pyroxenite sequence are distinct compared to those of the other peridotite-pyroxenite sequences of magmatic origin associated with the Ivrea Mafic Complex, the so-called Ultramafic Pipes (e.g., Locmelis et al., 2016) and the Monte Capio sill (Berno et al., 2020). Taken as a whole, these data suggest the involvement of compositionally heterogeneous sources for the mantle melts that gave rise to the Ivrea Mafic Complex. This mantle heterogeneity could be related to sources variably metasomatized by the Varisican subduction.

An age of 286.0 ± 3.0 Ma may be proposed for the formation of the Rocca d'Argimonia sequence, based on U-Pb zircon investigations of gabbronorites enclosing the peridotite-pyroxenite sequence. This age is consistent with a two-point Lu-Hf isochron of 285 ± 22 Ma, obtained from clinopyroxene and amphibole separated from a dunite. The Rocca d'Argimonia sequence therefore could develop in conjunction with the main phase of the Mafic Complex formation, which occurred within a time window of 4 M.y. (285.5-281.6 Ma), as recently documented by U-Pb zircon investigations by isotope dilution TIMS (Karakas et al., 2019). It cannot be excluded, however, that the ~286 Ma age represents a cooling rather than an intrusion age, in response to prolonged stay of the Lower Mafic Complex at the solidus transition zone.

The Rocca d'Argimonia dunites show evidence for Nd-Sr-Hf isotopic disequilibrium. The observed Nd-Sr-Hf isotopic discrepancy between the whole-rock and the clinopyroxene (+ amphibole) in the dunites is interpreted to reflect the presence of a fine-grained accessory phase that

is isotopically enriched with respect to clinopyroxene and amphibole. This "hidden" phase could be related to melt trapping during olivine growth, in agreement with a process of reactive melt flow. The clinopyroxene-amphibole pairs could crystallize from melts that were isotopically more depleted than the olivine-forming melts. Alternatively, the "hidden" phase developed in response to migration of late-stage melts or high-temperature fluids released from enclosing gabbronorites into the dunites.

The Rocca d'Argimonia peridotites and included clinopyroxenes show minor variations in Nd isotopic compositions, whereas the Sr-Hf isotopic signature displays a relatively wide range. Notably, the $^{87}Sr/^{86}Sr_{(286\ Ma)}$ and the $\varepsilon_{Hf(286\ Ma)}$ of the peridotites roughly increase and decrease, respectively, with decreasing Mg#. In addition, the $^{87}Sr/^{86}Sr_{(286\ Ma)}$ and the $\varepsilon_{Hf(286\ Ma)}$ of the peridotite clinopyroxenes define rough positive and negative correlations with $\delta^{18}O$ of coexisting olivine (data after Antonicelli et al., 2020). The Sr-Hf isotopic signature of the peridotites therefore suggests the occurrence of a crustal contamination process driven by fractional crystallization and concomitant assimilation of isotopically enriched crustal material (i.e., the AFC of DePaolo, 1981).

The Nd-Sr-Hf isotopic signature of the Rocca d'Argimonia pyroxenites is similar to that of associated peridotites. The lack of a clear isotopic distinction between the two rock-types contrasts with building of the peridotite-pyroxenite sequence through an AFC-type process. Conversely, formation of the pyroxenites may be reconciled with the process of reacting melt flow envisaged by Antonicelli et al. (2020), in response to a high melt/olivine ratio that completely dissolved the pre-existing olivine and led to crystallization of orthopyroxene, clinopyroxene and amphibole. The melt pervasively migrating through the olivine-rich matrix could be crustally contaminated, similar to the melts forming the crosscutting gabbronorite dykes.

The somewhat contrasting information for the mechanism leading to crustal contamination of the mantle-derived magma most likely reflects the complexity of the process forming the Rocca d'Argimonia peridotite-pyroxenite sequence. It should be noted that this process could also involve contaminating crustal materials with different isotopic signature. We speculate that the reactive melt migration operated through a melt-poor olivine-rich crystal mush formed by an AFC-type process. The crystal mush olivine and its melt inclusions could therefore have a slightly heterogeneous Nd-Sr-Hf isotopic signature, which could be modified by the subsequent process of reactive melt migration.

The petrographic, chemical and isotopic characteristics of the gabbronorite dykes that crosscut the Rocca d'Argimonia peridotites are clearly distinct compared to the gabbronorites enclosing the peridotite-pyroxenite sequence. In particular, the gabbronorite dykes have Nd-Sr-Hf isotopic compositions that are similar to those of the peridotites and the pyroxenites, whereas the enclosing gabbronorites show a markedly enriched isotopic signature, similar to what is observed for most

gabbroic-dioritic rocks of the Ivrea Mafic Complex (see Voshage et al., 1990, and Sinigoi et al., 1991, 2016). The chemical-isotopic fingerprint of the gabbronorites enclosing the peridotite-pyroxenite sequence suggests formation by highly evolved melts possessing a substantial crustal component, genetically unrelated to the peridotite-pyroxenite sequence.

In summary, the following sequence of events is formulated for the formation of the Rocca d'Argimonia peridotite-pyroxenite sequence:

1. intrusion of chemically primitive mantle-derived magmas into the lower continental crust;
2. formation of a melt-poor olivine-rich crystal mush by slow cooling, presumably associated with minor assimilation of crustal material;
3. building of the peridotite-pyroxenite sequence in response to reactive migration of hybrid melts derived from the enclosing gabbronorites.

References

Antonicelli, M., Tribuzio, R., Liu, T., and Wu, F. Y.: Contaminating melt flow in magmatic peridotites from the lower continental crust (Rocca d'Argimonia sequence, Ivrea–Verbano Zone), European Journal of Mineralogy, 32, 587–612, 2020.

Baker, A. J.: Stable isotopic evidence for fluid-rock interactions in the Ivrea Zone, Italy, Journal of Petrology, 31(1), 243-260, 1990.

Barnes, S. J., Mole, D. R., Le Vaillant, M., Campbell, M. J., Verrall, M. R., Roberts, M. P., and Evans, N. J.: Poikilitic textures, heteradcumulates and zoned orthopyroxenes in the Ntaka Ultramafic Complex, Tanzania: implications for crystallization mechanisms of oikocrysts, Journal of Petrology, 57(6), 1171-1198, 2016.

Berno, D., Tribuzio, R., Zanetti, A., and Hémond, C.: Evolution of mantle melts intruding the lowermost continental crust: constraints from the Monte Capio-Alpe Cevia mafic-ultramafic sequences (Ivrea-Verbano Zone, northern Italy), Contributions to Mineralogy and Petrology, 175(1), 2, 2020.

Bertolani, M., and Loschi-Ghittoni, A. G.: La zona a ultrabasiti della Rocca D'Argimonia nelle Prealpi Biellesi. La petrografia, Rendiconti Società Italiana di Mineralogia e Petrologia, 35(2), 791-813, 1979.

Bindeman, I. N., Ponomareva, V. V., Bailey, J. C., and Valley, J. W.: Volcanic arc of Kamchatka: a province with high-$\delta^{18}O$ magma sources and large-scale $^{18}O/^{16}O$ depletion of the upper crust, Geochimica et Cosmochimica Acta, 68(4), 841-865, 2004.

Boriani, A., and Giobbi, E.: Does the basement of western southern Alps display a tilted section through the continental crust? A review and discussion, Periodico di Mineralogia, 73(2), 5-22, 2004.

Brey, G. P., and Köhler, T.: Geothermobarometry in four-phase lherzolites II. New thermobarometers, and practical assessment of existing thermobarometers, Journal of Petrology, 31(6), 1353-1378, 1990.

Bucholz, C. E., Jagoutz, O., VanTongeren, J. A., Setera, J., and Wang, Z.: Oxygen isotope trajectories of crystallizing melts: Insights from modeling and the plutonic record, Geochimica et Cosmochimica Acta, 207, 154-184, 2017.

Bussolesi, M., Grieco, G., and Tzamos, E.: Olivine–Spinel Diffusivity Patterns in Chromitites and Dunites from the Finero Phlogopite-Peridotite (Ivrea-Verbano Zone, Southern Alps): Implications for the Thermal History of the Massif, Minerals, 9(2), 75, 2019.

Chiba, H., Chacko, T., Clayton, R. N., and Goldsmith, J. R.: Oxygen isotope fractionations involving diopside, forsterite, magnetite, and calcite: Application to geothermometry, Geochimica et Cosmochimica Acta, 53(11), 2985-2995, 1989.

Corvò, S., Langone, A., Padrón-Navarta, J. A., Tommasi, A., and Zanetti, A.: Porphyroclasts: source and sink of major and trace elements during deformation-induced metasomatism (Finero, Ivrea Verbano Zone, Italy), Geosciences, 10(5), 196, 2020.

Demarchi, G., Quick, J. E., Sinigoi, S., and Mayer, A.: Pressure gradient and original orientation of a lower-crustal intrusion in the Ivrea-Verbano Zone, Northern Italy, Journal of Geology, 106, 609-622, 1998.

Denyszyn, S. W., Fiorentini, M. L., Maas, R., and Dering, G.: A bigger tent for CAMP, Geology, 46(9), 823-826, 2018.

DePaolo, D. J.: A neodymium and strontium isotopic study of the Mesozoic calc-alkaline granitic batholiths of the Sierra Nevada and Peninsula Ranges, California, Journal of Geophysical Research, 86, 10470-10488, 1981.

Dohmen, R., Chakraborty, S., and Becker, H. W.: Si and O diffusion in olivine and implications for characterizing plastic flow in the mantle, Geophysical Research Letters, 29(21), 26-1, 2002.

Eiler, J. M.: Oxygen isotope variations of basaltic lavas and upper mantle rocks, Reviews in Mineralogy and Geochemistry, 43(1), 319-364, 2001.

Eiler, J. M., Baumgartner, L. P., and Valley, J. W.: Intercrystalline stable isotope diffusion: a fast grain boundary model, Contributions to Mineralogy and Petrology, 112(4), 543-557, 1992.

Eiler, J. M., Valley, J. W., and Baumgartner, L. P.: A new look at stable isotope thermometry, Geochimica et Cosmochimica Acta, 57, 2571-2571, 1993.

Eiler, J. M., Farley, K. A., Valley, J. W., Stolper, E. M., Hauri, E. H., and Craig, H.: Oxygen isotope evidence against bulk recycled sediment in the mantle sources of Pitcairn Island lavas, Nature, 377(6545), 138-141, 1995.

Ewing, T. A., Hermann, J., and Rubatto, D.: The robustness of the Zr-in-rutile and Ti-in zircon thermometers during high-temperature metamorphism (Ivrea–Verbano Zone, northern Italy), Contributions to Mineralogy and Petrology, 4, 757–779, 2013.

Ferrario, A., Garuti, G., Rossi, A., and Sighinolfi, G. P. (Eds.): Petrographic and metallogenic outlines of the “La Balma-M. Capio” ultramafic-mafic body (Ivrea-Verbano basic complex, NW

Italian Alps), In Mineral Deposits of the Alps and of the Alpine Epoch in Europe, Springer, Berlin, Heidelberg, Germany, 28-40, 1983.

Fiorentini, M. L., LaFlamme, C., Denyszyn, S., Mole, D., Maas, R., Locmelis, M., Caruso, S., and Bui, T. H.: Post-collisional alkaline magmatism as gateway for metal and sulfur enrichment of the continental lower crust, Geochimica et Cosmochimica Acta, 223, 175-197, 2018.

Garuti, G., Fiandri, P., and Rossi, A.: Sulfide composition and phase relations in the Fe-Ni-Cu ore deposits of the Ivrea-Verbano basic complex (western Alps, Italy), Mineralium Deposita, 21(1), 22-34, 1986.

Garuti, G., Bea, F., Zaccarini, F., and Montero, P.: Age, geochemistry and petrogenesis of the ultramafic pipes in the Ivrea Zone, NW Italy, Journal of Petrology, 42(2), 433-457, 2001.

Giletti, B. J.: Diffusion effects on oxygen isotope temperatures of slowly cooled igneous and metamorphic rocks, Earth and Planetary Science Letters, 77(2), 218-228, 1986.

Guergouz, C., Martin, L., Vanderhaeghe, O., Thébaud, N., and Fiorentini, M.: Zircon and monazite petrochronologic record of prolonged amphibolite to granulite facies metamorphism in the Ivrea-Verbano and Strona-Ceneri Zones, NW Italy, Lithos, 308-309, 1-18, 2018.

Günther, T., Haase, K. M., Junge, M., Oberthür, T., Woelki, D., and Krumm, S.: Oxygen isotope and trace element compositions of platiniferous dunite pipes of the Bushveld Complex, South Africa–Signals from a recycled mantle component?, Lithos, 310, 332-341, 2018.

Handy, M. R., Franz, L., Heller, F., Janott, B., and Zurbriggen, R.: Multistage accretion and exhumation of the continental crust (Ivrea crustal section, Italy and Switzerland), Tectonics, 18(6), 1154-1177, 1999.

Hart, S. R., and Davis, K. E.: Nickel partitioning between olivine and silicate melt, Earth and Planetary Science Letters, 40(2), 203-219, 1978.

Hartmann, G., and Wedepohl, K. H.: The composition of peridotite tectonites from the Ivrea Complex, northern Italy: residues from melt extraction, Geochimica et Cosmochimica Acta, 57(8), 1761-1782, 1993.

Holland, T., and Blundy, J.: Non-ideal interactions in calcic amphiboles and their bearing on amphibole-plagioclase thermometry, Contributions to Mineralogy and Petrology, 116(4), 433-447, 1994.

Jackson, J. M., Sinogeikin, S. V., Carpenter, M. A., and Bass, J. D.: Novel phase transition in orthoenstatite, American Mineralogist, 89(1), 239-244, 2004.

Jackson, M. D., Blundy, J., and Sparks, R. S. J.: Chemical differentiation, cold storage and remobilization of magma in the Earth's crust, Nature, 564(7736), 405-409, 2018.

Karakas, O., Wotzlaw, J.-F., Guillong, M., Ulmer, P., Brack, P, Economos, R., Bergantz, G. W., Sinigoi, S., and Bachmann, O.: The pace of crustal-scale magma accretion and differentiation beneath silicic caldera volcanoes, Geology, 47, 719-723, 2019.

Kaufmann, F. E., Vukmanovic, Z., Holness, M. B., and Hecht, L.: Orthopyroxene oikocrysts in the MG1 chromitite layer of the Bushveld Complex: implications for cumulate formation and recrystallisation, Contributions to Mineralogy and Petrology, 173(2), 17, 2018.

Kempton, P. D., and Harmon, R. S.: Oxygen isotope evidence for large-scale hybridization of the lower crust during magmatic underplating, Geochimica et Cosmochimica Acta, 56(3), 971-986, 1992.

Klötzli, U. S., Sinigoi, S., Quick, J. E., Demarchi, G., Tassinari, C. C., Sato, K., and Günes, Z.: Duration of igneous activity in the Sesia Magmatic System and implications for high-temperature metamorphism in the Ivrea-Verbano deep crust, Lithos, 206, 19-33, 2014.

Korenaga, J., and Kelemen, P. B.: Major element heterogeneity in the mantle source of the North Atlantic igneous province, Earth and Planetary Science Letters, 184(1), 251-268, 2000.

Kruger, W., and Latypov, R.: Fossilized solidifications fronts in the Bushveld Complex argues for liquid-dominated magmatic systems, Nature Communications, 11(1), 1-11, 2020.

Kunz, B. E., and White, R. W.: Phase equilibrium modelling of the amphibolite to granulite facies transition in metabasic rocks (Ivrea Zone, NW Italy), Journal of Metamorphic Geology, 37(7), 935-950, 2019.

Langone, A., Padrón-Navarta, J. A., Ji, W.-Q., Zanetti, A., Mazzucchelli, M., Tiepolo, M., Giovanardi, T., and Bonazzi, M.: Ductile-brittle deformation effects on crystal-chemistry and U-Pb ages of magmatic and metasomatic zircons from a dyke of the Finero Mafic Complex (Ivrea-Verbano Zone, Italian Alps), Lithos, 284-285, 493-511, 2017.

Leake, B. E., Woolley, A. R., Arps, C. E., Birch, W. D., Gilbert, M. C., Grice, J. D., Hawthorne, F. C., Kato, A., Kisch, H. J., Krivovichev, V. G., Linthout, K., Laird, J., Mandarino, J., Maresch, W. V., Nickel, E. H., Tock, N. M. S., Schumacher, J. C., Smith, D. C., Stephenson, N. C. N., Ungaretti, L., Whittaker, E. J. W., and Youzhi, G.: Nomenclature of amphiboles; report of the Subcommittee on

Amphiboles of the International Mineralogical Association Commission on new minerals and mineral names, Mineralogical Magazine, 61(405), 295-310, 1997.

Lensch, G.: Die Ultramafitite der Zone von Ivrea und ihre geologische Interpretation, Schweiz. Mineral. Petrogr. Mitt., 48, 91·102, 1968.

Li, C. F., Chu, Z. Y., Guo, J. H., Li, Y. L., Yang, Y. H., and Li, X. H.: A rapid single column separation scheme for high-precision Sr–Nd–Pb isotopic analysis in geological samples using thermal ionization mass spectrometry, Analytical Methods, 7(11), 4793-4802, 2015.

Lissenberg, C. J., and MacLeod, C. J.: A reactive porous flow control on the Mid-ocean ridge magmatic evolution, Journal of Petrology, 57, 2195–2220, 2016.

Locmelis, M., Fiorentini, M. L., Rushmer, T., Arevalo Jr, R., Adam, J., and Denyszyn, S. W.: Sulfur and metal fertilization of the lower continental crust, Lithos, 244, 74-93, 2016.

Ludwig, K. R.: Isoplot 3.00: A Geochronological Toolkit for Microsoft Excel, Berkeley Geochronology Center Special Publication: Berkeley, CA, USA, 4, 70, 2003.

Ma, Q., Yang, M., Zhao, H., Evans, N. J., Chu, Z. Y., Xie, L. W., ... and Yang, Y. H.: Accurate and precise determination of Lu and Hf contents and Hf isotopic composition at the sub-nanogram level in geological samples using MC-ICP-MS, Journal of Analytical Atomic Spectrometry, 34(6), 1256-1262, 2019.

Mao, Y. J., Barnes, S. J., Qin, K. Z., Tang, D., Martin, L., Su, B., and Evans, N. J.: Rapid orthopyroxene growth induced by silica assimilation: constraints from sector-zoned orthopyroxene, olivine oxygen isotopes and trace element variations in the Huangshanxi Ni–Cu deposit, Northwest China, Contributions to Mineralogy and Petrology, 174(4), 33, 2019.

Mattey, D., Lowry, D., and Macpherson, C.: Oxygen isotope composition of mantle peridotite, Earth and Planetary Science Letters, 128(3-4), 231-241, 1994.

Mayer, A., Mezger, K., and Sinigoi, S.: New Sm-Nd ages for the Ivrea-Verbano Zone, Sesia and Sessera Valleys (Northern Italy), Journal of Geodynamics, 30, 147-166, 2000.

Mazzucchelli, M., Rivalenti, G., Brunelli, D., Zanetti, A., and Boari, E.: Formation of highly refractory dunite by focused percolation of pyroxenite-derived melt in the Balmuccia peridotite massif (Italy), Journal of Petrology, 50(7), 1205-1233, 2009.

Mukasa, S. B., and Shervais, J. W.: Growth of subcontinental lithosphere: evidence from repeated dike injections in the Balmuccia lherzolite massif, Italian Alps, Lithos, 48, 287-316, 1999.

Nandedkar, R. H., Ulmer, P., and Müntener, O.: Fractional crystallization of primitive, hydrous arc magmas: an experimental study at 0.7 GPa, Contributions to Mineralogy and Petrology, 167(6), 1015, 2014.

Nandedkar, R. H., Hürlimann, N., Ulmer, P., and Müntener, O.: Amphibole–melt trace element partitioning of fractionating calc-alkaline magmas in the lower crust: an experimental study, Contributions to Mineralogy and Petrology, 171(8-9), 71, 2016.

Nekvasil, H., Dondolini, A., Horn, J., Filiberto, J., Long, H., and Lindsley, D. H.: The origin and evolution of silica-saturated alkalic suites: an experimental study, Journal of Petrology, 45(4), 693-721, 2004.

Peressini, G., Quick, J. E., Sinigoi, S., Hofmann, A. W., and Fanning, M.: Duration of a large mafic intrusion and heat transfer in the lower crust: a SHRIMP U–Pb zircon study in the Ivrea–Verbano Zone (Western Alps, Italy), Journal of Petrology, 48(6), 1185-1218, 2007.

Pistone, M., Müntener, O., Ziberna, L., Hetényi, G., and Zanetti, A.: Report on the ICDP workshop DIVE (Drilling the Ivrea-Verbano zonE), Scientific Drilling, 23, 47-56, 2017.

Putirka, K.: Amphibole thermometers and barometers for igneous systems and some implications for eruption mechanisms of felsic magmas at arc volcanoes, American Mineralogist, 101(4), 841-858, 2016.

Quick, J. E., Sinigoi, S., Negrini, L., Demarchi, G., and Mayer, A.: Synmagmatic deformation in the underplated igneous complex of the Ivrea-Verbano zone, Geology, 20(7), 613-616, 1992.

Quick, J. E., Sinigoi, S., and Mayer, A.: Emplacement of mantle peridotite in the lower continental crust, Ivrea-Verbano zone, northwest Italy, Geology, 23(8), 739-742, 1995.

Quick, J. E., Sinigoi, S., Snoke, A. W., Kalakay, T. J., Mayer, A., and Peressini, G.: Geologic map of the southern Ivrea-Verbano Zone northwestern Italy. U.S. Geological Survey, Geologic Investigations Series Map I-2776, scale 1:25,000, 2003.

Redler, C., White, R. W., and Johnson, T. E.: Migmatites in the Ivrea Zone (NW Italy): constraints on partial melting and melt loss in metasedimentary rocks from Val Strona di Omegna, Lithos, 175, 40-53, 2013.

Rivalenti, G., Garuti, G., and Rossi, A.: The origin of the Ivrea-Verbano Basic Formation (Western Italian Alps) - whole rock geochemistry, Bollettino della Società Geologica Italiana, 94, 1149-1186, 1975.

Rivalenti, G., Rossi, A., Siena, F., & Sinigoi, S.: The layered series of the Ivrea-Verbano igneous complex, we tern Alps, Italy, Tschermaks Mineralogische und Petrographische Mitteilungen, 33(2), 77-99, 1984.

Rivalenti, G., Mazzucchelli, M., Vannucci, R., Hofmann, A. W., Ottolini, L., and Obermiller, W.: The relationship between websterite and peridotite in the Balmuccia peridotite massif (NW Italy) as revealed by trace element variations in clinopyroxene, Contributions to Mineralogy and Petrology, 121, 275-288, 1995.

Rosenbaum, J. M., Kyser, T. K., and Walker, D.: High temperature oxygen isotope fractionation in the enstatite-olivine-$BaCO_3$ system, Geochimica et Cosmochimica Acta, 58(12), 2653-2660, 1994.

Russell, W. A., Papanastassiou, D. A., and Tombrello, T. A.: Ca isotope fractionation on the Earth and other solar system materials, Geochimica et Cosmochimica Acta, 42(8), 1075-1090, 1978.

Schmid, S. M., Kissling, E., Diehl, T., van Hinsbergen, D. J., and Molli, G.: Ivrea mantle wedge, arc of the Western Alps, and kinematic evolution of the Alps–Apennines orogenic system, Swiss Journal of Geosciences, 110(2), 581-612. 2017.

Schnetger, B.: Partial melting during the evolution of the amphibolite-to granulite-facies gneisses of the Ivrea Zone, northern Italy, Chemical Geology, 113(1-2), 71-101, 1994.

Selverstone, J., and Sharp, Z. D.: Chlorine isotope evidence for multicomponent mantle metasomatism in the Ivrea Zone, Earth and Planetary Science Letters, 310(3-4), 429-440, 2011.

Sessa, G., Moroni, M., Tumiati, S., Caruso, S., and Fiorentini, M. L.: Ni-Fe-Cu-PGE ore deposition driven by metasomatic fluids and melt-rock reactions in the deep crust: the ultramafic pipe of Valmaggia, Ivrea-Verbano, Italy, Ore Geology Reviews, 90, 485-509, 2017.

Shervais, J. W., and Mukasa, S. B.: The Balmuccia orogenic lherzolite massif, Italy, Journal of Petrology, Special Lherzolite Issue, 155-174, 1991.

Sinigoi, S., Antonini, P., Demarchi, G., Longinelli, A., Mazzucchelli, M., Negrini, L., and Rivalenti, G.: Intractions of mantle and crustal magmas in the southern part of the Ivrea Zone (Italy), Contributions to Mineralogy and Petrology, 108(4), 385-395, 1991.

Sinigoi, S., Quick, J. E., Clemens-Knott, D., Mayer, A., Demarchi, G., Mazzucchelli, M., Negrini, L., and Rivalenti, G.: Chemical evolution of a large mafic intrusion in the lower crust, Ivrea-Verbano Zone, northern Italy, Journal of Geophysical Research: Solid Earth, 99(B11), 21575-21590, 1994.

Sinigoi, S., Quick, J. E., Mayer, A., and Demarchi, G.: Density-controlled assimilation of underplated crust, Ivrea-Verbano Zone, Italy, Earth and Planetary Science Letters, 129(1-4), 183-191, 1995.

Sinigoi, S., Quick, J. E., Mayer, A., and Budahn, J. R.: Influence of stretching and density contrasts on the chemical evolution of continental magmas: an example from the Ivrea-Verbano Zone, Contributions to Mineralogy and Petrology, 123, 238-250, 1996.

Sinigoi, S., Quick, J. E., Demarchi, G., and Klötzli, U. S: The role of crustal fertility in the generation of large silicic magmatic systems triggered by intrusion of mantle magma in the deep crust, Contributions to Mineralogy and Petrology, 162, 691-707, 2011.

Sinigoi, S., Quick, J. E., Demarchi, G., and Klötzli, U. S.: Production of hybrid granitic magma at the advancing front of basaltic underplating: Inferences from the Sesia Magmatic System (south-western Alps, Italy), Lithos, 252, 109-122, 2016.

Sláma, J., Košler, J., Condon, D. J., Crowley, J. L., Gerdes, A., Hanchar, J. M., ... and Schaltegger, U.: Plešovice zircon—a new natural reference material for U–Pb and Hf isotopic microanalysis, Chemical Geology, 249(1-2), 1-35, 2008.

Solano, J. M. S., Jackson, M. D., Sparks, R. S. J., Blundy, J. D., and Annen, C.: Melt segregation in deep crustal hot zones: a mechanism for chemical differentiation, crustal assimilation and the formation of evolved magmas, Journal of Petrology, 53(10), 1999-2026, 2012.

Solano, J. M. S., Jackson, M. D., Sparks, R. S. J., and Blundy, J.: Evolution of major and trace element composition during melt migration through crystalline mush: implications for chemical differentiation in the crust, American Journal of Science, 314(5), 895-939, 2014.

Su, B., Chen, Y., Guo, S., and Liu, J.: Origins of orogenic dunites: petrology, geochemistry, and implications, Gondwana Research, 29(1), 41-59, 2016.

Sun, S. S., and McDonough, W. F.: Chemical and isotopic systematics of oceanic basalts: implications for mantle composition and processes, Geological Society, London, Special Publications, 42(1), 313-345, 1989.

Tilhac, R., Ceuleneer, G., Griffin, W. L., O'Reilly, S. Y., Pearson, N. J., Benoit, M., ... and Grégoire, M.: Primitive arc magmatism and delamination: petrology and geochemistry of Pyroxenites from the Cabo Ortegal Complex, Spain, Journal of Petrology, 57(10), 1921-1954, 2016.

Tribuzio, R., Thirlwall, M. F., and Messiga, B.: Petrology, mineral and isotope geochemistry of the Sondalo gabbroic complex (Central Alps, Northern Italy): implications for the origin of post-Variscan magmatism, Contributions to Mineralogy and Petrology, 136(1-2), 48-62, 1999.

Valley, J. W.: Stable isotope thermometry at high temperatures, Reviews in Mineralogy and Geochemistry, 43(1), 365-413, 2001.

Van Achterbergh, E., Ryan, C. G., and Griffin, W. L.: GLITTER on-line interactive data reduction for the LA-ICPMS microprobe, Macquarie Research Ltd., Sydney, 2001.

Vavra, G., Schmid, R., and Gebauer, D.: Internal morphology, habit and U-Th-Pb microanalysis of amphibolite-to-granulite facies zircons: geochronology of the Ivrea Zone (Southern Alps), Contributions to Mineralogy and Petrology, 134(4), 380-404, 1999.

Vermeesch, P.: IsoplotR: A free and open toolbox for geochronology, Geoscience Frontiers, 9(5), 1479-1493, 2018.

Vervoort, J. D., Patchett, P. J., Söderlund, U., and Baker, M.: Isotopic composition of Yb and the determination of Lu concentrations and Lu/Hf ratios by isotope dilution using MC-ICPMS, Geochemistry, Geophysics, Geosystems, 5(11), 2004.

Villiger, S., Ulmer, P., Müntener, O., and Thompson, A. B.: The liquid line of descent of anhydrous, mantle-derived, tholeiitic liquids by fractional and equilibrium crystallization - an experimental study at 1.0 GPa, Journal of Petrology, 45(12), 2369-2388, 2004.

Villiger, S., Müntener, O., and Ulmer, P.: Crystallization pressures of mid-ocean ridge basalts derived from major element variations of glasses from equilibrium and fractional crystallization experiments, Journal of Geophysical Research: Solid Earth, 112(B1). 2007.

Voshage, H., Hunziker, J. C., Hofmann, A. W., and Zingg, A.: A Nd and Sr isotopic study of the Ivrea zone, Southern Alps, N-Italy, Contributions to Mineralogy and Petrology, 97(1), 31-42, 1987.

Voshage, H., Sinigoi, S., Mazzucchelli, M., Demarchi, G., Rivalenti, G., and Hofmann, A. W.: Isotopic constraints on the origin of ultramafic and mafic dikes in the Balmuccia peridotite (Ivrea Zone), Contributions to Mineralogy and Petrology, 100(3), 261-267, 1988.

Voshage, H., Hofmann, A. W., Mazzucchelli, M., Rivalenti, G., Sinigoi, S., Raczek, I., and Demarchi, G.: Isotopic evidence from the Ivrea Zone for a hybrid lower crust formed by magmatic underplating, Nature, 347(6295), 731-736, 1990.

Wells, P. R.: Pyroxene thermometry in simple and complex systems, Contributions to Mineralogy and Petrology, 62(2), 129-139, 1977.

Weyer, S., and Schwieters, J. B.: High precision Fe isotope measurements with high mass resolution MC-ICPMS, International Journal of Mass Spectrometry, 226(3), 355-368, 2003.

Whitney, D. L., and Evans, B. W.: Abbreviations for names of rock-forming minerals, American Mineralogist, 95(1), 185-187, 2010.

Wiedenbeck, M. A. P. C., Alle, P., Corfu, F., Griffin, W. L., Meier, M., Oberli, F. V., ... and Spiegel, W.: Three natural zircon standards for U-Th-Pb, Lu-Hf, trace element and REE analyses, Geostandards Newsletter, 19(1), 1-23, 1995.

Wilson, M., Neumann, E. R., Davies, G. R., Timmerman, M. J., Heeremans, M., and Larsen, B. T.: Permo-Carboniferous magmatism and rifting in Europe: introduction, Geological Society, London, Special Publications, 223(1), 1-10, 2004.

Wu, F. Y., Yang, Y. H., Xie, L. W., Yang, J. H., and Xu, P.: Hf isotopic compositions of the standard zircons and baddeleyites used in U–Pb geochronology, Chemical Geology, 234(1-2), 105-126, 2006.

Yang, Y. H., Zhang, H. F., Chu, Z. Y., Xie, L. W., and Wu, F. Y.: Combined chemical separation of Lu, Hf, Rb, Sr, Sm and Nd from a single rock digest and precise and accurate isotope determinations of Lu–Hf, Rb–Sr and Sm–Nd isotope systems using Multi-Collector ICP-MS and TIMS, International Journal of Mass Spectrometry, 290(2-3), 120-126, 2010.

Yang, A. Y., Wang, C., Liang, Y., and Lissenberg, C. J.: Reaction between mid-ocean ridge basalt and lower oceanic crust: An experimental study, Geochemistry, Geophysics, Geosystems, 20(9), 4390-4407, 2019.

Yao, J. H., Zhu, W. G., Li, C., Zhong, H., Yu, S., Ripley, E. M., and Bai, Z. J.: Olivine O isotope and trace element constraints on source variation of picrites in the Emeishan flood basalt province, SW China, Lithos, 338, 87-98, 2019.

Zaccarini, F., Garuti, G., Fiorentini, M. L., Locmelis, M., Kollegger, P., and Thalhammer, O. A.: Mineralogical hosts of platinum group elements (PGE) and rhenium in the magmatic Ni-Fe-Cu sulfide deposits of the Ivrea Verbano Zone (Italy): an electron microprobe study, Neues Jahrbuch für Mineralogie-Abhandlungen: Journal of Mineralogy and Geochemistry, 191(2), 169-187, 2014.

Zanetti, A., Giovanardi, T., Langone, A., Tiepolo, M., Wu, F. Y., Dallai, L., and Mazzucchelli, M.: Origin and age of zircon-bearing chromitite layers from the Finero phlogopite peridotite (Ivrea-Verbano Zone, Western Alps) and geodynamic consequences, Lithos, 262, 58-74, 2016.